Characteristics of Three-dimensional Vortex Formation and Propulsive Performance in Flapping Locomotion

Thesis by

Daegyoum Kim

In Partial Fulfillment of the Requirements

for the Degree of

Doctor of Philosophy

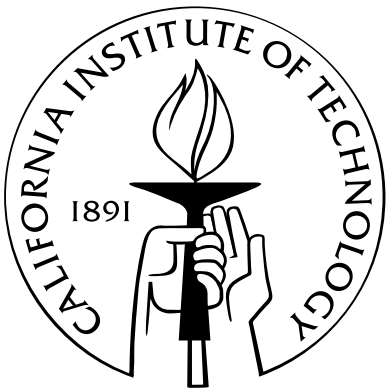

California Institute of Technology

Pasadena, California

2010

(Defended May 25, 2010)

Acknowledgements

First, I would like to thank Prof. Morteza Gharib, my advisor, for his generous support, which was essential in the completion of this work. His passion and broad interest in research have always motivated me. I was fortunate to do research under his insightful guidance and the great experimental environment he had created.

I extend my thanks to Prof. John Dabiri, Prof. Beverley McKeon and Prof. Dale Pullin for serving on my defense committee and reviewing my dissertation, and Prof. Tim Colonius for serving on my candidacy committee. Their comments were helpful in improving the quality of my work. The discussion with Prof. Fazle Hussain during his visit to Caltech was invaluable in building up my philosophy about academic research. I am also grateful to Prof. Jeff Eldredge whose computational code was a great tool in understanding some of the problems I encountered during my work.

Dr. William Dickson helped me to set up the initial experiment. Without his help, I would have had much more difficulty starting my experiment. I was happy to be with Gharib group members for three years. I gleaned useful information in a variety of fields from them. With the assistance of Martha Salcedo, devoted supporter of our group, I was able to conduct my research without any trouble.

I am grateful to the Samsung Scholarship Foundation for financial aid. Their decision to support me before my application for admission gave me the invaluable opportunity to study at GALCIT.

I appreciate my family's heartfelt support. They consistently encouraged my educational endeavors. Above all, I would like to express my deepest gratitude to my wife, Hae Jin. With her unconditional love, I could devote my best to graduate study. She was also my best mentor, friend and colleague. My thesis is dedicated to her.

Abstract

Three-dimensional vortex formation and propulsive performance were studied experimentally to identify some of the main characteristic mechanisms of flapping locomotion. Mechanical models with thin plates were used to simulate flapping and translating motions of animal propulsors. Three-dimensional flow fields were mapped quantitatively using defocusing digital particle image velocimetry.

First, vortex structures made by impulsively translating low aspect-ratio plates were studied. The investigation of translating plates with a 90° angle of attack is important since it is a fundamental model for a better understanding of drag-based propulsion systems. Rectangular flat-rigid, flexible, and curved-rigid thin plastic plates with the same aspect ratio were used to compare their vortex structures and hydrodynamic forces. The interaction of the tip flow and the nearby vortex is a critical flow phenomenon to distinguish vortex patterns among these three cases. In the flexible plate case, slow development of the vortex structure causes a small initial peak in hydrodynamic force during the acceleration phase. However, after the initial peak, the flexible plate generates large force magnitude comparable to that of the flat-rigid plate case.

Drag-based paddling propulsion was also studied to explain some of the fundamental differences in vortex formation of lift-based and drag-based propulsions. While the temporal change of the inner area enclosed by the vortex loop is an important factor in thrust generation of lift-based propulsion, the temporal change of the vortex strength becomes more important in drag-based propulsion. Spanwise flow behind the paddling plate plays an important role in tip vortex motion and thrust generation. The distribution of spanwise flow depends on the propulsor shape and the Reynolds number. A delta-shaped propulsor generates strong spanwise flow compared to a rectangular propulsor. For the low Reynolds number case, the spanwise flow is not as strong as that of the high Reynolds number case. The flexible propulsor can smooth out force peaks during impulsive motions without sac-

rificing total impulse, which is advantageous in avoiding structural failures and stabilizing body motion. The role of the stopping vortex was addressed in optimizing a stroke angle of paddling animals.

In addition, vortex formation of clapping propulsion was investigated by varying aspect ratio and stroke angle. A low aspect-ratio propulsor produces larger total impulse than a high aspect-ratio propulsor. As the aspect ratio increases, circulation of the vortex is strengthened, and the inner area enclosed by the vortex structure tends to enlarge. Moreover, in terms of thrust, the advantage of a single plate over double clapping plates is larger for the lower aspect-ratio case. These results offer information to better understand the benefit of low aspect-ratio wings in force generation under specific locomotion modes. When a pair of plates claps, a vortex loop forms from two counter-rotating tip vortices by a reconnection process. The dynamics of wake structures are dependent on the aspect ratio and the stroke angle.

Vortex formation and vorticity transport processes of translating and rotating plates with a 45° angle of attack were investigated as well. In both translating and rotating cases, the spanwise flow over the plate and the vorticity tilting process inside the leading-edge vortex were observed. The distribution of spanwise flow is a prominent distinction between the vortex structures of these two cases. While spanwise flow is confined inside the leading-edge vortex for the translating case, it is widely present over the plate and the wake region of the rotating case. As the Reynolds number decreases, due to the increase in viscosity, leading-edge and tip vortices tend to spread inside the area swept by the rotating plate, which results in lower lift force generation.

Lastly, for translating motion, the dynamics of the vortex in corner regions was compared among three different corner shapes. For a large corner angle, the forward movement of the vortex tends to be uniform along the plate edges. However, for a small corner angle, the vortex close to the corner moves forward following the plate while the vortex away from the corner retards its forward movement.

Contents

List of Figures

List of Tables

Chapter 1

Introduction

1.1 Motivation

The study on fluid dynamics of flapping animals has gained attention in recent years because of potential for bio-inspired applications such as micro air vehicles and underwater autonomous vehicles. In addition to the bio-inspired engineering of new propulsion systems, fluid dynamics of animal locomotion has been involved in other multi-disciplinary studies. The unsteady motion of the animal is an attractive model in developing the physics of unsteady flow. Vortex formation by an animal and its relation to propulsive performance is one emerging field of vortex dynamics. In terms of biology, the effects of surrounding fluid on propulsors are also important to understand how the form and function of propulsors have evolved and been optimized. Moreover, the dynamical interaction of surrounding fluid with sensory and muscular systems is an essential part of understanding locomotive neuronal feedback systems. Furthermore, the structural design of propulsors and its effect on propulsive performance are interesting problems in view of structural mechanics and material science.

Among various locomotion modes, we focus on the flapping motion of a thin propulsor, which is arguably the most common locomotion mode in flying and swimming animals. Birds and insects rely on flapping for their locomotion. Aquatic mammals and many fish also utilize this motion. The traditional aerodynamic theory of fixed wings has been applied to the aerodynamics or hydrodynamics of flapping animals. Unfortunately, it does not sufficiently explain the mechanisms of flapping propulsion. One of the most well-known problems is that, according to the traditional aerodynamic theory, insects should not hover in the air because they cannot obtain enough lift to support their weight. To tackle this

problem, researchers have suggested the unsteady lift generation strategies for hovering insects (Ellington *et al.*, 1996; Dickinson *et al.*, 1999). This approach teaches us that a new approach, totally different from the traditional aerodynamic theory, is required in order to understand the principles of flapping locomotion.

In order to better understand the aerodynamics of flying animals, it is also important to find the difference between fixed wings of airplanes and flapping wings of flying animals. First of all, flow around the airplane wing is steady or quasi-steady while flow near the flapping wing is unsteady due to repeated power and recovery strokes. Second, for the fixed wing case, there are specific components responsible for lift, thrust, and control respectively. However, in flying animals, the whole wing is responsible for force production and control without any functional distinction. Third, while airplane wings are rigid and have a high aspect ratio, animal wings are flexible and generally have a low aspect ratio. The effect of flexibility on aerodynamic performance has been studied. The flexible wings of insects are found to be more efficient in lift generation than the stiff wings (Mountcastle & Daniel, 2009; Young *et al.*, 2009). Fourth, for better aerodynamic performance, airplanes and flapping animals use different strategies. flow control (e.g., suppression of flow separation for drag reduction) is important in the fixed-wing aerodynamics to improve the performance. Meanwhile, in flapping animals, the flow is separated from the edge because the angle of attack is relatively high, and optimal vortex formation is the most relevant aerodynamic phenomena in improving their propulsive performance (Dabiri, 2009). The fluid dynamical features of flapping animals mentioned here are also applicable to swimming animals.

Through this thesis work, the primary focus was to study how three-dimensional vortex structures are generated by flapping propulsors under various conditions of kinematics, flexiblity, aspect ratio, and shape of propulsors, as well as the Reynolds number. The Reynolds number studied in this work is in the range of $O(10)$ to $O(10^4)$. Moreover, the relation between the vortex formation process and propulsive performance of flappers was analyzed under various conditions. For these purposes, we used simple mechanical models instead of studying live animals. Thin plastic or glass plates were used as propulsors. Forces acting on moving models were measured with a load cell. Details of the model conditions under study are explained in §1.4.

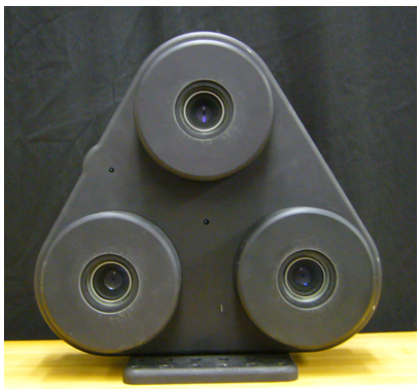

Figure 1.1: Front view of the DDPIV camera.

1.2 Defocusing digital particle image velocimetry

In order to map three-dimensional flow fields and identify three-dimensional vortex structures, defocusing digital particle image velocimetry (DDPIV) (Willert & Gharib, 1992; Pereira & Gharib, 2002; Pereira *et al.*, 2006; Graff, 2007; Lai *et al.*, 2008) was used. DDPIV is a novel technique to measure 3D position and velocity components of particles within a camera probe volume. In the standard imaging system with one aperture, for a particle in the imaging volume, only one particle image is shown in the image. For the camera with multiple apertures, one particle image is shown if a particle is on the focal plane of the camera. However, if a particle is out of the focal plane, multiple particle images appear in the image (for details, see figure 1 of (Pereira *et al.*, 2000)). From the distance information between multiple particle images, it is possible to construct 3D coordinates of the particle in the camera probe volume. The original design of the system was one camera with three apertures in a triangle configuration. This design has two problems. Each particle is shown as triple particles in the image. Therefore, heavily seeded particles in the fluid volume result in heavily overlapped particle images. In addition, the distance between apertures should be large to map the larger fluid volume. In order to solve these issues, the DDPIV concept was extended to the system with three cameras in a triangular configuration (figure 2 of (Pereira *et al.*, 2000)). Each camera has one aperture. The camera used in this study was built by Graff (2007)(figure 1.1). Once the coordinates of the particles in the flow are found, the velocity of the particles can be calculated by tracking particles between two successive frames.

Here, we briefly explain the DDPIV procedure used in our study. The camera was placed in front of the tank. The tank was filled with water or mineral oil. The tank was seeded with silver-coated glass spheres of mean diameter 100 μm (Conduct-o-fil, Potters Industries Inc.). The particles illuminated by an Nd:YAG laser (200 mJ/pulse, Gemini PIV, New Wave Research Inc.) were captured by the DDPIV camera. The images taken from the DDPIV camera were processed with the DDPIV software based on Pereira & Gharib (2002); Pereira *et al.* (2006). First, three-dimensional coordinates of the particles inside the tank were found by matching particles in three images captured by the DDPIV camera. Then, from the position information of the particles, the velocity vectors of the particles were calculated from a relaxation method of 3D particle tracking (Pereira *et al.*, 2006). The velocity vectors obtained by this step are randomly spaced in the camera probe volume. The number of cubic grids with size $3 \times 3 \times 3$ mm^3 in the mapped domain (about $160 \times 160 \times 160$ mm^3) was quite large compared to the number of randomly-spaced velocity vectors obtained from one case (≈ 5000). To obtain the number of velocity vectors as many as the number of grids, the experiment was repeated 25 (or 20) times under the same conditions with an interval of 90 sec. The interval between the cases was enough to calm the flow generated by the previous case. Then, for each time frame, the randomly-spaced velocity vectors from the 25 (or 20) cases were collected. The collected velocity vectors were interpolated into cubic grids to produce a velocity field. If the number of cases is much more than 25, the accuracy is expected to improve. However, due to a processing time issue, we chose to limit to 25 cases. After removing outlier velocity vectors and applying a smoothing operator to velocity fields, the vorticity field was obtained by a central difference scheme from the velocity data. For smooth rendering of three-dimensional iso-surfaces of vorticity, vorticity vectors were smoothed. The new vorticity at a node was computed by $\boldsymbol{\omega}_{new} = (\boldsymbol{\omega}_{old} + \bar{\boldsymbol{\omega}}_{nb})/2$ where $\bar{\boldsymbol{\omega}}_{nb}$ is the mean of six neighbor vorticity values. This smoothing process was iterated three times.

The performance of particle position reconstruction in the DDPIV system with three cameras has been characterized (Pereira *et al.*, 2000; Kajitani & Dabiri, 2005; Grothe & Dabiri, 2008; Graff & Gharib, 2008). For a particle in the air, the uncertainty of particle coordinates on the plane parallel to a camera front (in-plane uncertainty) is proportional to the distance of the particle from the camera, while the uncertainty in the direction perpendicular to the camera front (out-of-plane uncertainty) is proportional to its square.

For this reason, if the particle is far from the camera, out-of-plane uncertainty of particle coordinates is generally larger than in-plane uncertainty. For the DDPIV system used in this study, the error of the particle position constructed from the images was measured experimentally with the method of Pereira *et al.* (2000). Inside the camera probe volume, the out-of-plane mean error of the particle position was 40 μm for water and 49 μm for oil, and the in-plane mean error was 6 μm for both fluids. This error analysis was conducted for the experiment in Ch. 5.

For the validation of the DDPIV, the flow field data obtained by the DDPIV was compared to that of the planar DPIV (Willert & Gharib, 1991). The model for Ch. 3 experiment was used for the validation test. The triangular plate was rotated counter-clockwise from the camera view. The Reynolds number based on the mean tip velocity and the span length was 140. The trapezoidal velocity program was used for rotation. For the details of the model conditions and DDPIV procedures, refer to Ch. 3. For image process of the planar DPIV, PIVview2C Ver 3.0 (PIVTEC GmbH) was used. The flow of the symmetrical $z = 0$ plane was mapped for the planar DPIV. A multi-grid interrogation scheme was used. The first interrogation window size was 96 $\times$ 96 pixels with a 50 % overlap, and the final interrogation window size was 48 $\times$ 48 pixels with a 50 % overlap. The correlation process was repeated twice. The total vectors for each velocity field were 65 $\times$ 49 vectors. Outlier vectors were removed and replaced by the interpolation from their surrounding neighbor vectors. The grid size of the velocity fields was 4.4 $\times$ 4.4 mm^2.

Figure 1.2 shows vorticity (ω_z) fields from both DDPIV and planar DPIV. In general, the velocity and vorticity fields obtained from the DDPIV tend to be smoothed because the flow is phase-averaged to get enough randomly-spaced velocity vectors. Figure 1.3 shows the circulation of the tip vortex from two PIV techniques. The maximum relative difference of the tip vortex circulation, $(\Gamma_{3D}\text{-}\Gamma_{2D})/\Gamma_{2D}$, is 0.09 for the case of figure 1.3. In other cases conducted for the purpose of DDPIV and planar DPIV comparison, the maximum relative difference was below 0.10.

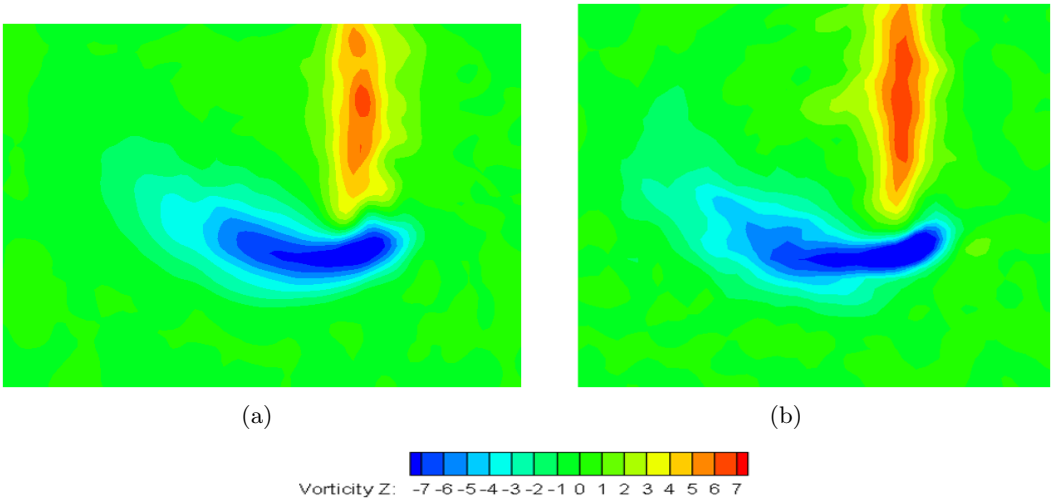

Figure 1.2: Vorticity fields obtained from (a) the DDPIV and (b) the planar DPIV.

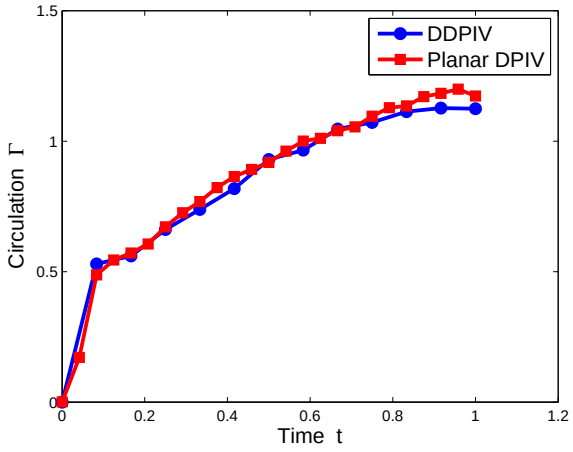

Figure 1.3: Circulation Γ of the tip vortex (the blue contour in figure 1.2) obtained from the DDPIV and the planar DPIV.

1.3 Vortex formation in lift-based and drag-based propulsions

The locomotion mechanism of flapping animals can be categorized into two modes: lift-based and drag-based propulsions (Vogel, 2003; Alexander, 2003). In lift-based propulsion, most propulsive force acts perpendicularly to the moving direction of the flapper with a small angle of attack. Meanwhile, in drag-based propulsion with a large angle of attack such as paddling and rowing modes, the propulsive force acts on the flapper mainly in the direction opposite the moving direction of the flapper. Vogel (2003) conjectured that the lift-based propulsion mode was more efficient in high speed locomotion establishing why fast-moving flapping animals employed this mode. He also argued that the drag-based mode was effective in low speed locomotion in that it could generate large thrust over a short time. Therefore, the drag-based propulsion mode is preferred in maneuvering behaviors such as acceleration, turning, and braking (Walker & Westneat, 2000).

The fundamental difference in vortex formation mechanism between lift-based propulsion and drag-based propulsion can be understood by examining the relationship between force generation and flow field. The hydrodynamic (aerodynamic) force acting on a moving object inside an infinite flow field can be derived from vorticity distribution of the flow field and velocity of the object (Wu, 1981).

$$\boldsymbol{F} = -\frac{\rho_f}{2}\frac{\mathrm{d}}{\mathrm{d}t}\int_{V_\infty} \boldsymbol{x} \times \boldsymbol{\omega} \mathrm{d}V + \rho_f \frac{\mathrm{d}}{\mathrm{d}t}\int_{V_b} \boldsymbol{u} \mathrm{d}V, \tag{1.1}$$

where ρ_f is fluid density, V_∞ is an infinite flow field, and V_b is body volume. If vorticity is confined in a closed vortex loop of circulation (Γ) and the object is thin, Eq. 1.1 can simply be approximated as follows (Wu *et al.*, 2006),

$$\boldsymbol{F}(t) \approx -\rho_f \frac{\mathrm{d}}{\mathrm{d}_t}(\Gamma \boldsymbol{S}) = -\rho_f(\dot{\Gamma}\boldsymbol{S} + \Gamma\dot{\boldsymbol{S}}). \tag{1.2}$$

$\boldsymbol{S}$ is the vector of the minimum surface spanned by the vortex loop and $|\boldsymbol{S}|$ is the area of the surface. If propulsive force (F_p) is applied on the object in the negative x-direction,

$$F_p(t) = -F_x(t) \approx \rho_f(\dot{\Gamma} S_x + \Gamma \dot{S_x}), \tag{1.3}$$

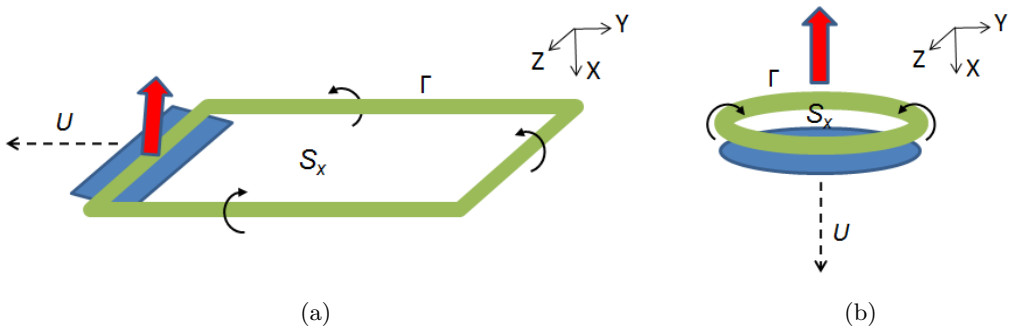

(a) (b)

Figure 1.4: Vortex structures in (a) lift-based propulsion and (b) drag-based propulsion. The thick green line is the vortex generated by a moving object. The curved arrows around the vortex show the rotating direction of the vortex. The dashed black arrow indicates the moving direction of the object. The thick red arrow indicates the direction of force acting on the object.

where S_x is the area of S projected on the yz-plane. Eqs. 1.2 and 1.3 show that the increase in the area enclosed by the vortex loop ($\dot{\boldsymbol{S}}$ and $\dot{S}_x$) and the growth of circulation ($\dot{\Gamma}$) are correlated with force generation. Figure 1.4 illustrates two simple examples of force generation modes: lift-based propulsion and drag-based propulsion. When a flying animal glides with a constant speed and a small angle of attack (figure 1.4(a)), the circulation of the vortex structure is assumed to be constant in time; the first term ($\dot{\Gamma} S_x$) in the right-hand side of Eq. 1.3 is neglected in lift generation. To apply Eq. 1.3 to drag-based propulsion, we first consider the example of a falling circular disk whose face is perpendicular to the falling direction (figure 1.4(b)). Vorticity is assumed to be created at the edge of the disk and the vortex is rolled up around the edge of the disk. In this case, while the inner area of the vortex loop can be assumed to be approximately constant, the circulation growth of the vortex loop cannot be neglected, and the first term ($\dot{\Gamma} S_x$) of Eq. 1.3 contributes significantly to the lift generation of the falling disk. For drag-based propulsion modes such as paddling and rowing in which the propulsor rotates with a joint, the temporal change of a vortex inner area projected in the thrust direction should also be taken into consideration. In the following chapters, the above equations will be referred to frequently in order to discuss results.

1.4 Outline

In the following chapters, translating, padding, clapping, and hovering motions of the plates are examined. The common point of these motions is that the angle of attack is high; either 45° for Ch. 5 or 90° for the other chapters. Each chapter was written as an independent report. Therefore, some content is duplicated among the chapters. Especially, the procedure explained in the *Experimental setup* section is quite similar to one another. Here, research topics are outlined.

- Ch. 2 Translating motion of rigid and flexible normal plates
  - Effect of flexibility on tip flow and vortex development near the tip.
  - Drag force and its correlation with vortex circulation.
- Ch. 3 Paddling propulsion
  - Interaction of spanwise flow and a tip vortex and its effect on tip vortex morphology.
  - Dependence of spanwise flow on plate shape and the Reynolds number.
  - Change of thrust trend by flexibility.
  - Optimal stroke angle for efficient thrust generation.
- Ch. 4 Clapping propulsion
  - Vortex formation and wake dynamics under some stroke angles and aspect ratios.
  - Relation between aspect ratios and total impulse.
  - Propulsive advantage of double clapping plates over a single plate.
  - Formation time for optimal vortex formation.
- Ch. 5 Translating and rotating motions with 45° angle of attack
  - Comparison of vortex structure and spanwise flow distribution between translating and rotating motions.
  - Vorticity transport by convection, tilting and diffusion.
  - Viscous effect on vorticity distribution and lift production.

- Ch. 6 Dynamics of corner vortices
  - Influence of corner angles on the dynamics of corner vortices in translating plates.

Chapter 2

Translating motion of rigid and flexible normal plates

2.1 Background

The interest in unsteady flow at low to intermediate Reynolds numbers has increased in recent years because of potential bio-inspired applications to micro air vehicles and underwater autonomous vehicles. Previous experimental studies have sought to find the physics of unsteady flow using simple body shapes and simple motions (Dickinson & Götz, 1993; Ringuette *et al.*, 2007). Others have used live animals or robotic models to study animal locomotion (Ellington *et al.*, 1996; Drucker & Lauder, 1999; Birch & Dickinson, 2001). However, most of these experimental studies were based on two-dimensional flow field measurements, which limited their ability to present a complete physical picture of these inherently three-dimensional unsteady flows.

Flapping is a widely used locomotion mode of flying and swimming animals. Propulsion by flapping is used in both air and water in a broad range of Reynolds number regimes (Vogel, 2003). The flow induced by the flapping motion of animals has some distinct features. The first feature is the small aspect ratio (AR) of animal wings and fins. Thus, the influence of tip flow is significant. Second, the flow induced by the motion of a flapper is unsteady. Third, the angle of attack of the propulsor can be quite high. Finally, the propulsor is not rigid and has some flexibility in general. In this sense, impulsively starting flexible plates at a high angle of attack in low Reynolds number ranges will be an important model for an in-depth study relevant to animal locomotion.

Vortices created by flapping motion have been the central subject in studying animal

locomotion since hydrodynamic forces and efficiency are closely related to the generation and transport of vortices. Researchers who have tried to identify vortices in animal locomotion using flow visualization techniques have pointed to the possible correlation between hydrodynamic force acting on animals and observed vortices (Ellington *et al.*, 1996; Drucker & Lauder, 1999; Birch & Dickinson, 2001; Srygley & Thomas, 2002; Spedding *et al.*, 2003). These studies addressed cases where the flapper undergoes complex three-dimensional motion. The lack of a proper three-dimensional flow mapping system as well as the inherent complexity of flow due to three-dimensional motion has posed major difficulties in providing comprehensive principles of flapping motions. Even though it is desirable to study the three-dimensional vortex created by complex flapping motion, we have focused on the vortex structure created in a relatively simple translating motion.

The mechanical properties of the flexible wings of insects and the relation between wing deformation and aerodynamic performance have been studied. Combes & Daniel (2003*a*) and Combes & Daniel (2003*b*) measured the bending stiffness of insect wings and found the anisotropy of the bending stiffness in the spanwise and chordwise directions. Combes & Daniel (2003*c*) insisted that passive wing deformation of their models was mainly caused by inertial-elastic force by rapid acceleration and deceleration, rather than aerodynamic force. From flow visualization, Mountcastle & Daniel (2009); Young *et al.* (2009) showed that the flexible wings of insects are more efficient in lift generation than the stiff wings. Here, we study the effect of the flexibility on the vortex formation and the trend of force generation. Only the spanwise bending of the plate is considered. By focusing on the translating motion of a rectangular plate, we can isolate the effect of wing flexibility from other effects such as rotation and specific wing geometry.

While many studies have been performed for two-dimensional flow around a translating plate with a high angle of attack as a fundamental study for insect flight (Dickinson & Götz, 1993; Pullin & Wang, 2004; Wang, 2004), few have been done for a model with a small AR, either experimentally or computationally, (Ringuette *et al.*, 2007; Taira & Colonius, 2009). Ringuette *et al.* (2007) reported that the unsteady drag coefficient of a plate with a small AR is bigger than the plate with a larger AR because the tip edge contributes to drag. Ringuette *et al.* (2007) obtained vorticity fields and calculated the circulation at three sections using planar digital particle image velocimetry (DPIV). Because of the inherent limitation of planar DPIV, they couldn't obtain three-dimensional velocity and vorticity fields. Instead,

they focused more on the role of the tip vortex in the generation of hydrodynamic force.

In order to supplement Ringuette *et al.* (2007) experiment and find more on the three-dimensional vortex formation process, defocusing digital particle image velocimetry (DDPIV) (Willert & Gharib, 1992; Pereira & Gharib, 2002; Pereira *et al.*, 2006) was used for the purpose of mapping three-dimensional flow fields present in this study. A flat normal plate of AR = 3.75 is translated impulsively in a water tank. In addition, a flexible plate is also used to investigate the effect of plate flexibility on vortex formation and hydrodynamic force generation. A curved-rigid plate, which has a similar shape to the flexible plate at its maximum deformation, is also considered for comparison with the other cases.

2.2 Experimental setup

Figure 2.1 shows the experimental setup. A water tank with $870 \times 430 \times 360$ mm^3 dimensions was used for the experiment. Three polycarbonate plates ($\rho_m = 1.2$ g/cm^3) were used to represent *flat-rigid*, *flexible*, and *curved-rigid* plates. The thickness and Young's modulus of the rigid plates are 1.52 mm and 2.3 GPa, and those of the flexible plate are 0.25 mm and 2.4 GPa. Even though the plates with 1.52 mm thickness are not completely rigid, the deformation during translation is negligible and, thus, the *rigid* term is used as a counterpart to the *flexible* term. The width of the plate was 40 mm. In the middle of the tank, 150 mm of the plate was immersed vertically (figure 2.2). Part of the plate above a free surface was attached firmly to a load cell (miniature beam type, Interface Inc.). A traverse with a lead-screw (Velmex Inc.) to translate the plate was driven by a stepper motor. The traverse accelerated for 0.25 seconds at the start and moved with a constant velocity (U_c) of 50 mm/sec. The Reynolds number based on the constant traverse velocity and plate width ($\mathrm{Re} = U_c w/\nu$) was 2000. To make the curved shape for the curved-rigid plate, a hole near a tip edge was penetrated, and the thread was used to connect the hole and the load cell while keeping the plate curved (figure 2.2(b)). We tried to make the curved-rigid plate bend at the same degree as the flexible plate at its maximum deformation. For this purpose, we compared camera images of the curved-rigid and deformed flexible plates. However, there were some deviations in curvatures because it was difficult to match the shapes exactly.

For the DDPIV setup (figure 2.1), the distance between the water tank and the camera, which was placed in front of the water tank, was adjusted to position the camera probe

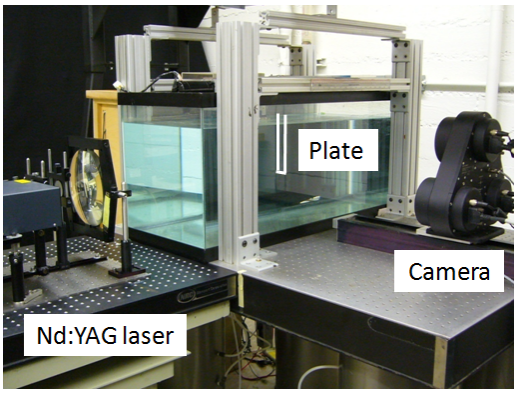

Figure 2.1: Experimental setup. White lines are the edges of the plate model.

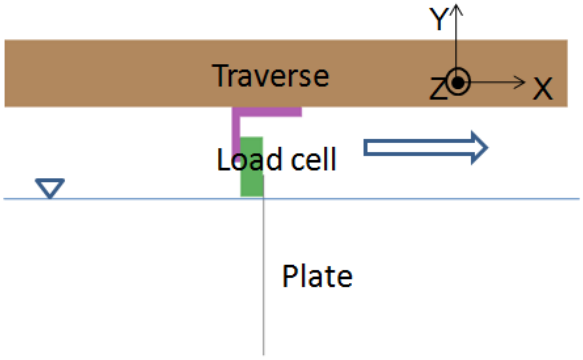

(a)

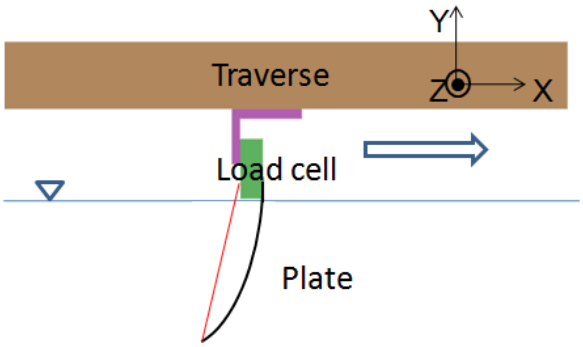

(b)

Figure 2.2: Details of the mechanical model from the camera view. In (a), the initial shape of the flat-rigid and flexible plates is shown. In (b), the initial shape of the curved-rigid plate is shown. The red line in (b) is the thread connecting the plate tip and the load cell to make the plate curved. The arrow indicates the moving direction of a traverse.

volume in the middle of the tank. The tank was seeded with silver-coated glass spheres of mean diameter 100 μm (Conduct-o-fil, Potters Industries Inc.). An Nd:YAG laser (200 mJ/pulse, Gemini PIV, New Wave Research Inc.) was placed to the left side of the camera and optical lenses were used to make a laser cone, which covered the camera probe volume. The traverse system, including the plate model and the load cell, was placed over the tank so that it could be seen from the camera. A stepper motor control computer sent trigger pulses to synchronize the DDPIV camera, the laser, and the motor start. Image pairs were captured at a rate of 5 pairs/sec. The time gap between two laser pulses to take a pair of images was 0.05 sec.

The images taken from the camera were processed with the DDPIV software based on Pereira & Gharib (2002) and Pereira *et al.* (2006). First, three-dimensional coordinates of the particles inside the tank were found. Then, from this information, velocity vectors of particles were calculated using a relaxation method of three-dimensional particle tracking (Pereira *et al.*, 2006). The flow field with $160 \times 160 \times 140$ mm^3 volume was cropped during these processes. The number of cubic grids with size $3 \times 3 \times 3$ mm^3 in the mapped domain was quite large compared to the number of randomly-spaced velocity vectors obtained from one case. To increase the density of randomly-spaced velocity vectors in a fluid domain, the experiment was repeated 20 times under the same conditions with an interval of 90 sec. For each time step, the randomly-spaced velocity vectors obtained from 20 cases were collected into one and interpolated into cubic grids to produce a velocity field. After removing outlier vectors and applying a smoothing operator to velocity vectors, the vorticity field was obtained by a central difference scheme. For smooth rendering of three-dimensional iso-surfaces of vorticity magnitude, vorticity data were also smoothed. When the plate moved outside of the camera probe volume, the initial position of the plate was moved back 80 mm so that the plate showed up in the camera volume later. Then, another set of the experiment was conducted for the later stage of the plate motion.

We also measured hydrodynamic drag forces acting on the plates moving in water. Force transducer outputs were amplified and low-pass filtered through a signal conditioner (SGA, Interface Inc.) and Matlab (The Mathworks Inc.) with 3 Hz cutoff frequency. Forces were also measured for the models in air in order to make sure that inertial forces were negligible. The flexible plate did not deform in the air in our model, which means that the plate was deformed mainly by the hydrodynamic force acting on the plate, rather than inertial-elastic

force. The same immersed area of the plate S (40 mm $\times$ 150 mm) and constant velocity of the traverse U_c were used in calculating drag coefficients ($C_D = D/\frac{1}{2}\rho_f U_c^2 S$) for all three conditions considered in this study. The drag is the force acting on the plate in the negative x-direction.

Following Gharib *et al.* (1998), a non-dimensional time T known as *formation time* was defined as $\int_0^{t_d} U(\tau)\mathrm{d}\tau/c$ where U is the traverse velocity, c is the plate width, and t_d is the dimensional time. In figures of §2.3, velocity, vorticity, circulation, and circulation rate are non-dimensionalized;

$$\boldsymbol{u} = \frac{\boldsymbol{u}_d}{U_c}, \quad \boldsymbol{\omega} = \frac{\boldsymbol{\omega}_d c}{U_c}, \quad \Gamma = \frac{\Gamma_d}{U_c c}, \quad \dot{\Gamma} = \frac{\dot{\Gamma}_d}{U_c^2}, \tag{2.1}$$

where the subscript d means the dimensional variable.

Two non-dimensional parameters are necessary to characterize the problem for the dynamical interaction of the deformable plate model and the surrounding fluid. Namely,

$$\frac{\rho_m}{\rho_f} = 1.2, \quad EI = \frac{(EI)_d}{\rho_f U_c^2 h^3} = 79.8(\text{rigid plate}) \text{ , } 0.4(\text{flexible plate}) \tag{2.2}$$

where $(EI)_d$ is the dimensional bending stiffness of plates per unit width, ρ_m and ρ_f are the density of plates and water, and h is the height of the plate inside the tank. Dynamically, the former is the ratio of the inertial force of the deforming plate to the inertial force of the surrounding fluid, and the latter shows the relative magnitude of the bending shear force of the plate over the inertial force of the surrounding fluid.

2.3 Results and Discussion

2.3.1 Vortex formation

Figure 2.3(a) depicts plate shapes for the three cases considered in this study. For the flexible plate case, the deformation is shown at several formation times (T). Throughout this study, the vortices generated along the vertical long edges of the plate are termed leading-edge vortices (LEV) and the vortex along the horizontal short edge is termed a tip vortex (TV) (figure 2.3(b)). From figures 2.4 to 2.9, iso-surfaces of vorticity plots represent vorticity magnitude of $|\boldsymbol{\omega}| = 2.4$. The white arrows in figures show the rotating direction of

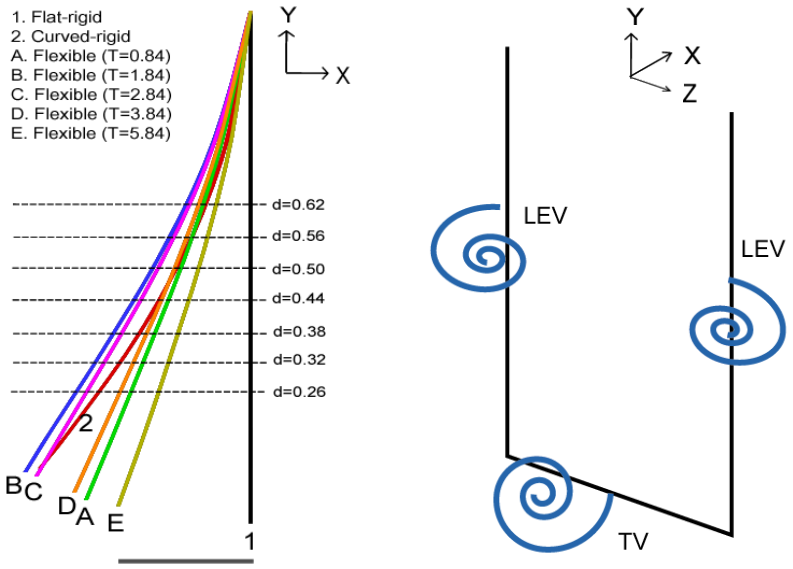

(a) (b)

Figure 2.3: (a) Shapes of the plates immersed in water during traverse movement. The plates are rearranged to have the same base position in order to compare x-directional deviation of the tip from a vertical line. Seven horizontal dashed lines are sections used in §2.3.3 for Γ_y calculation. A horizontal continuous line at the bottom is the distance which the traverse travels for $\Delta T = 1$ where T is the non-dimensional formation time. (b) Vortex term definition. A leading-edge vortex (LEV) is the vortex created along the span. A tip vortex (TV) is the vortex created at the tip.

the vortex with the right-hand rule. The regions of lower vorticity, such as the shear layer connecting the vortex core and the boundary layer, are not shown in figures 2.4 to 2.9. The plates shown in these figures are all immersed in water. The top area of the plate is beyond the camera probe volume and, thus, its flow field is absent. Figures 2.4 and 2.5 represent the flat-rigid plate case, figures 2.6 and 2.7 are for the flexible plate case, and figures 2.8 and 2.9 are for the curved-rigid plate case.

At the onset of the plate movement, a vortex sheet emanates from plate edges and begins to roll up the edges (figure 2.4). After $T = 1.84$, the LEV starts to get away from the plate in the mid-section of each side. During this process, the LEV forms a curved shape. Whereas the LEV near the tip remains attached to the plate, the LEV in the upper part detaches from the plate and slants into the xz-plane while moving outward in the z-direction. A high vorticity magnitude ($|\boldsymbol{\omega}| = 2.4$) is used in figure 2.4 for a better depiction of the vortex core structure. As a supplement, vorticity distribution with a lower threshold

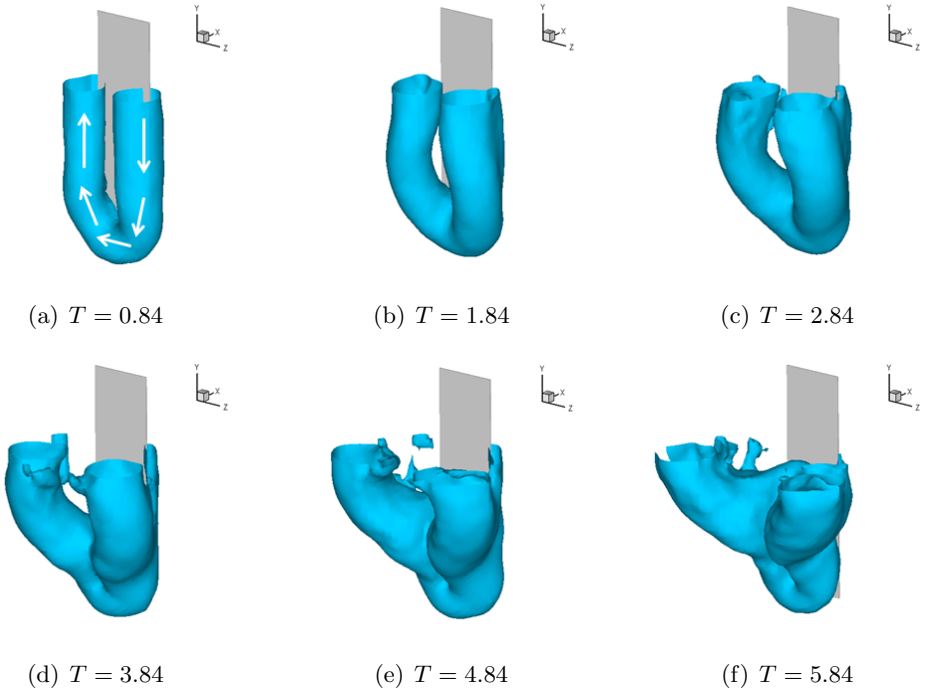

(a) $T = 0.84$ (b) $T = 1.84$ (c) $T = 2.84$

(d) $T = 3.84$ (e) $T = 4.84$ (f) $T = 5.84$

Figure 2.4: Isometric view of the vortex formation process in the flat-rigid plate case.

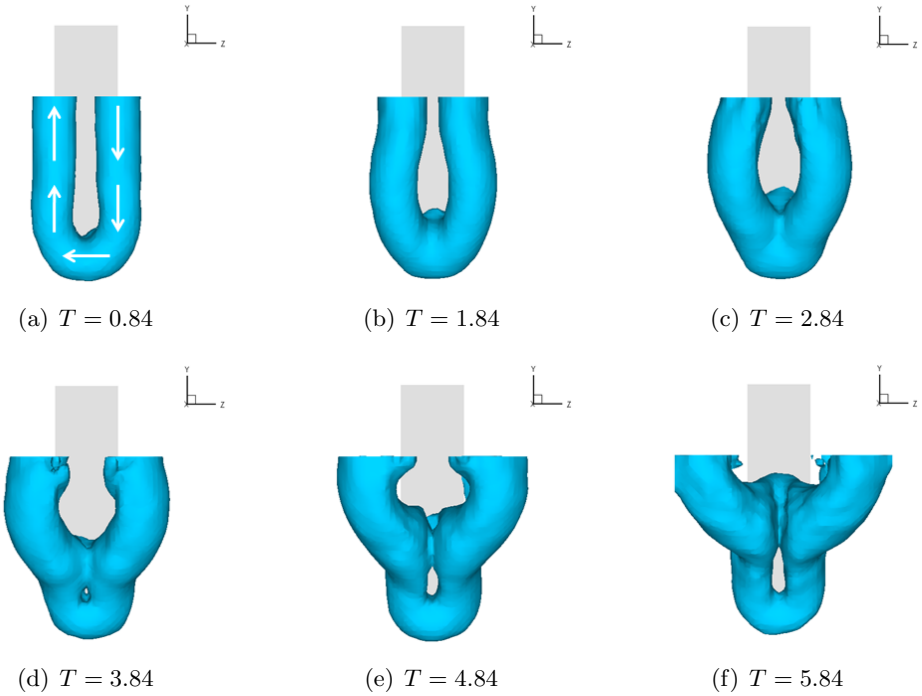

(a) $T = 0.84$ (b) $T = 1.84$ (c) $T = 2.84$

(d) $T = 3.84$ (e) $T = 4.84$ (f) $T = 5.84$

Figure 2.5: Back view of the vortex formation process in the flat-rigid plate case.

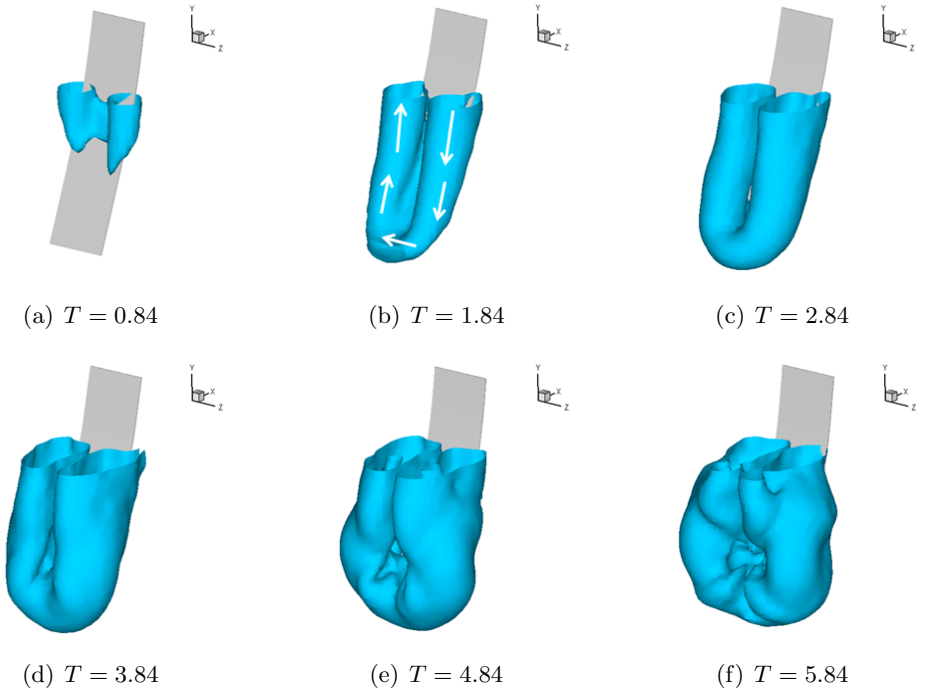

(a) $T = 0.84$ (b) $T = 1.84$ (c) $T = 2.84$

(d) $T = 3.84$ (e) $T = 4.84$ (f) $T = 5.84$

Figure 2.6: Isometric view of the vortex formation process in the flexible plate case.

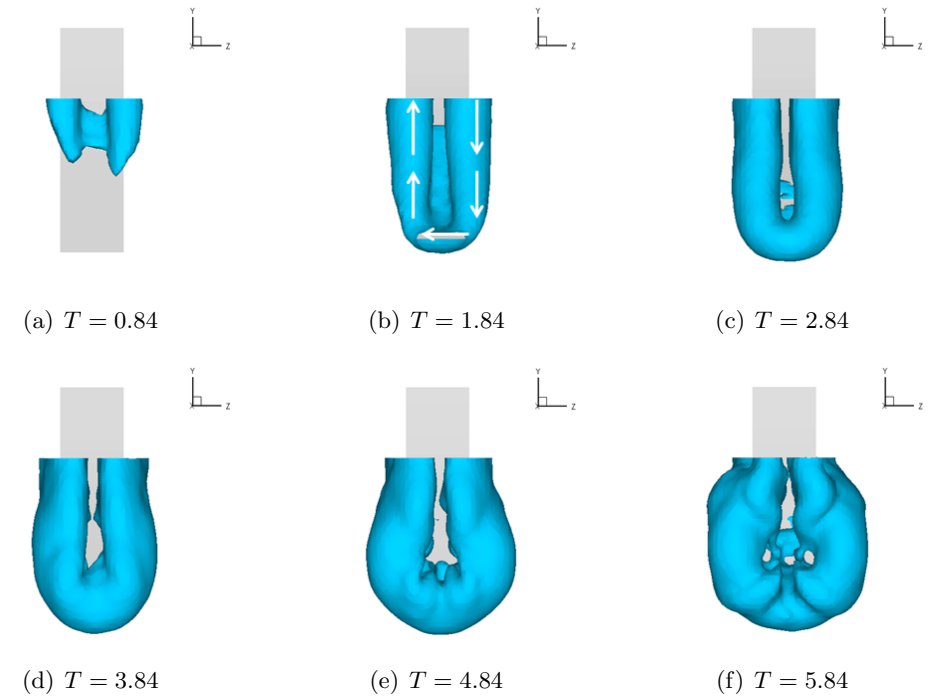

(a) $T = 0.84$ (b) $T = 1.84$ (c) $T = 2.84$

(d) $T = 3.84$ (e) $T = 4.84$ (f) $T = 5.84$

Figure 2.7: Back view of the vortex formation process in the flexible plate case.

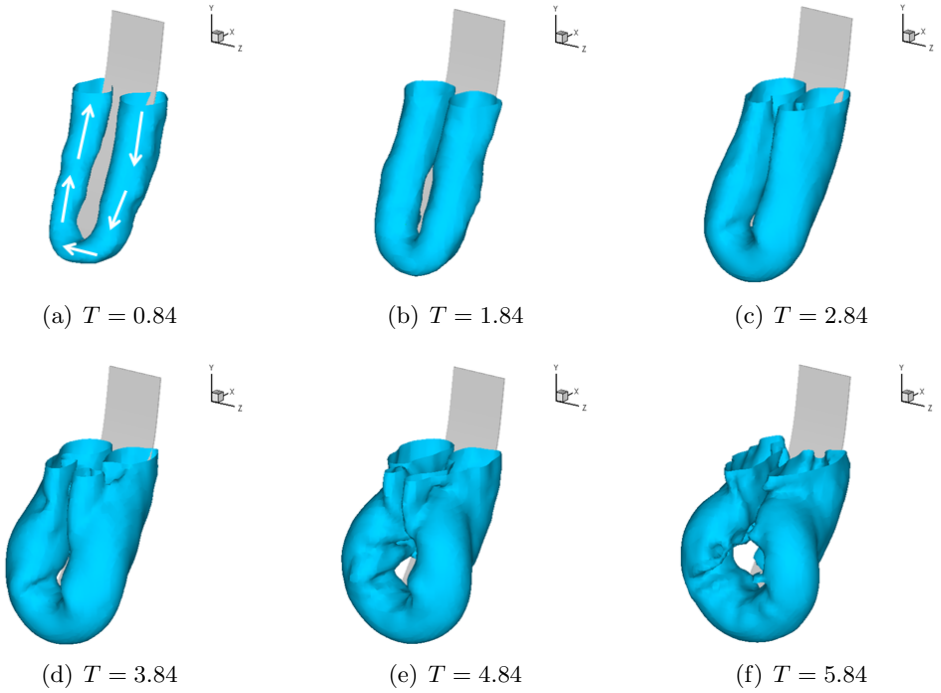

(a) $T = 0.84$ (b) $T = 1.84$ (c) $T = 2.84$

(d) $T = 3.84$ (e) $T = 4.84$ (f) $T = 5.84$

Figure 2.8: Isometric view of the vortex formation process in the curved-rigid plate case.

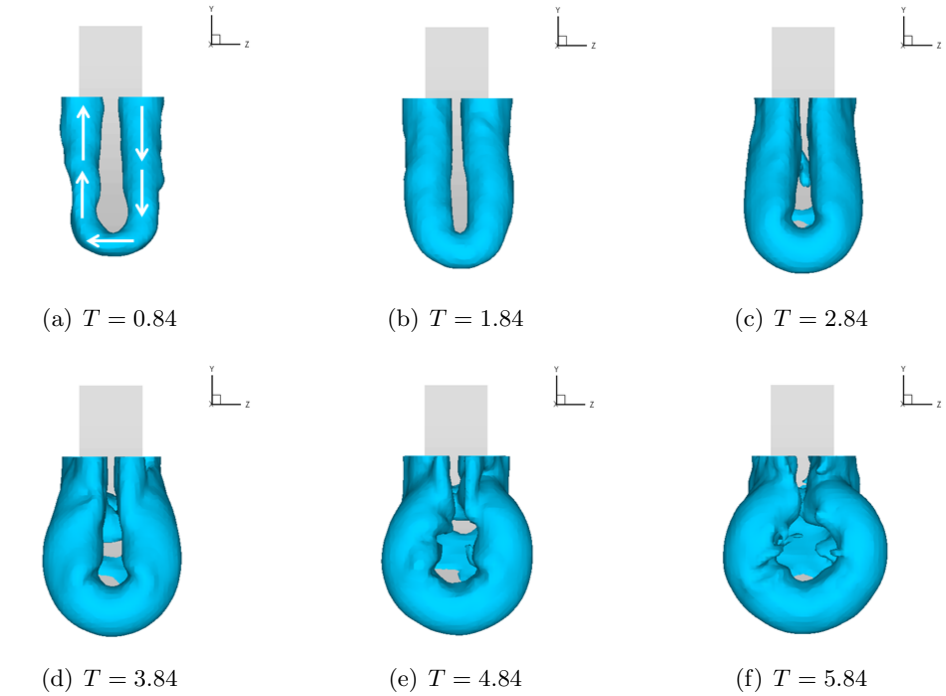

(a) $T = 0.84$ (b) $T = 1.84$ (c) $T = 2.84$

(d) $T = 3.84$ (e) $T = 4.84$ (f) $T = 5.84$

Figure 2.9: Back view of the vortex formation process in the curved-rigid plate case.

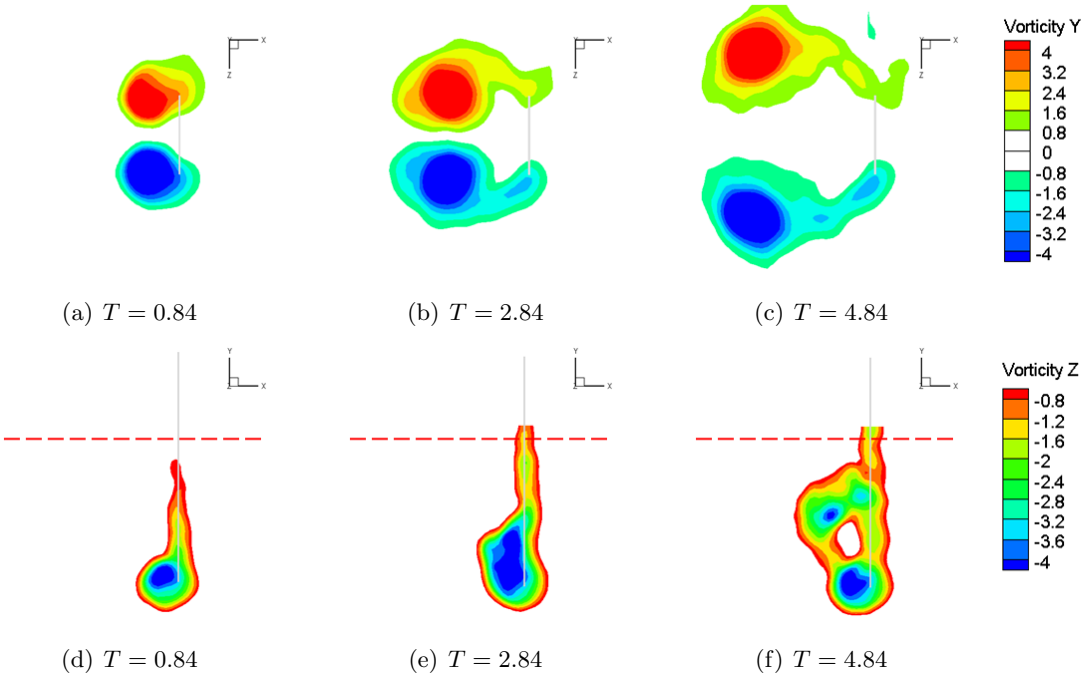

(a) $T = 0.84$ (b) $T = 2.84$ (c) $T = 4.84$

(d) $T = 0.84$ (e) $T = 2.84$ (f) $T = 4.84$

Figure 2.10: ω_y and ω_z distribution at sections in the flat-rigid plate case. (a)−(c) are ω_y at $T = 0.84$, $T = 2.84$, and $T = 4.84$. (d)−(f) are ω_z at $T = 0.84$, $T = 2.84$, and $T = 4.84$. The height of the y-section used for ω_y contour is shown as a long dashed line in (d)−(f). $z = 0$ section (middle section in z-direction) is used for ω_z contour.

value of vorticity magnitude is shown in figure 2.10. Near $T = 3.84$, the TV moves upward continuously due to the tip flow. A similar behavior has been reported by Ringuette *et al.* (2007). The upward motion of the TV is concurrent with the tilting of the LEV during the full observation time of the experiment. This continuous upward motion of the TV accentuates the upward propagation of the LEV tilting (figures 2.4(d)−2.4(f)).

In the flexible plate case, the forward motion of the lower part of the plate is delayed due to the flexibility of the plate, and the vortex system develops first in the upper part (figures 2.3(a) and 2.6(a)). As the lower part of the plate starts to move forward, the LEV and the TV begin to develop in the lower part as well. At the same time, the vortex sheet on the front surface of the plate, which connects two LEVs, moves toward the tip (figure 2.11). After $T = 2.84$, the curved shape of the plate is relaxed toward an equilibrium state. The vortex morphology follows the shape of the plate without exhibiting any distinct deformation until $T = 3.84$. However, after this time, the vortex deforms into a horseshoe shape in the lower region of the plate. During this deformation process of the lower LEV

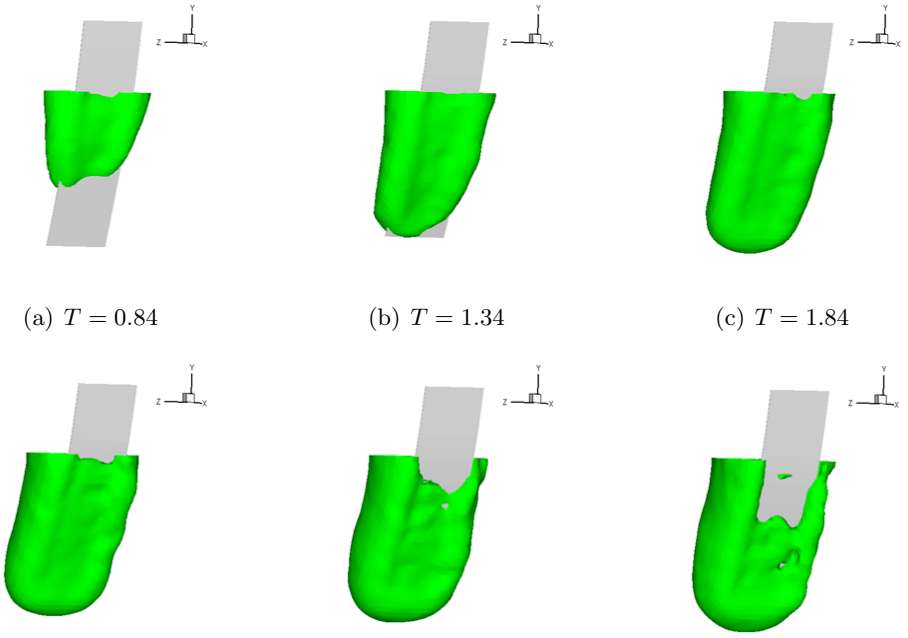

(a) $T = 0.84$ (b) $T = 1.34$ (c) $T = 1.84$

(d) $T = 2.34$ (e) $T = 2.84$ (f) $T = 3.34$

Figure 2.11: Vorticity distribution in front of the plate in the flexible plate case (iso-surface of vorticity magnitude, $|\boldsymbol{\omega}| = 1.6$). Vorticities in front of the upper part tend to move toward the tip.

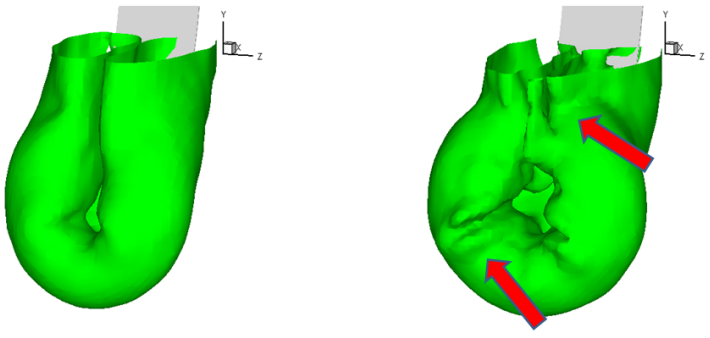

(a) (b)

Figure 2.12: Close-up to see the vortex deformation in the curved-rigid plate case in (a) $T = 3.84$ and (b) $T = 5.84$. Iso-surface of vorticity magnitude ($|\boldsymbol{\omega}| = 1.6$) is used. An upper arrow in (b) points out the lateral compression of the vortex core. A lower arrow shows corrugation of the vortex.

part, the vortex core in the upper part continues to elongate in the x-direction. Note that for the flat-rigid plate case, the LEV in the upper part of the plate moves away from the plate early. However, in the flexible plate case, the LEV in the upper part does not move outward from the plate edge and ends up having an elongated vortex core. When the LEV in the lower part tilts outward to make a horseshoe-shaped vortex, the LEVs in both edges of the upper region show a tendency to move inward. However, the LEV's inward movement would be limited due to the imposed symmetric condition at $z = 0$. Instead, the LEV core in the upper part folds and continues to elongate in the x-direction.

For the curved-rigid plate case, the vortex in the lower part of the plate grows faster than that of the flexible plate case. The formation of the vortex into a horseshoe shape in the lower region is more distinct than that of the flexible plate case, and the LEV is tilted vertically in the lower part as is the flexible plate case (figures 2.8(e) and 2.8(f)). The separation of the lower LEV from the plate edge is more distinct than that of the flexible plate case. The vortex system in the lower part of the plate becomes nearly a circular vortex and the vortex core becomes corrugated similar to the flexible plate case. This deformation is concurrent with the severe elongation of the LEV core in the upper part of the plate (figure 2.12).

2.3.2 Effect of tip flow on vortex formation

The outward motion of the LEV is not present in the flow field of impulsively moving two-dimensional flat plates (Koumoutsakos & Shiels, 1996). Thus, it is reasonable to conjecture that three-dimensional effects make the vortex formation process in our cases drastically different from that of their two-dimensional counterpart. The fundamental difference between these two cases is the presence of the tip flow and its influence on the nearby flow field. It will be shown that the main three-dimensional factor for the observed differences is the presence of an upward flow (tip flow in the positive y-direction) near the tip region.

First, let's consider the flat-rigid plate case. When the plate starts to move, upward flow is induced from the tip because forward motion of the plate creates a suction region behind the plate. Thus, the vortical flow near the tip penetrates into the inner region of the plate's backside. The upward flow near the tip interferes with the LEV formation process by being entrained to the upper part of the LEV. The entrainment of the tip flow forces the LEV to move away from the plate's edge (figures 2.13(a) and 2.13(b)). Once the LEV starts to

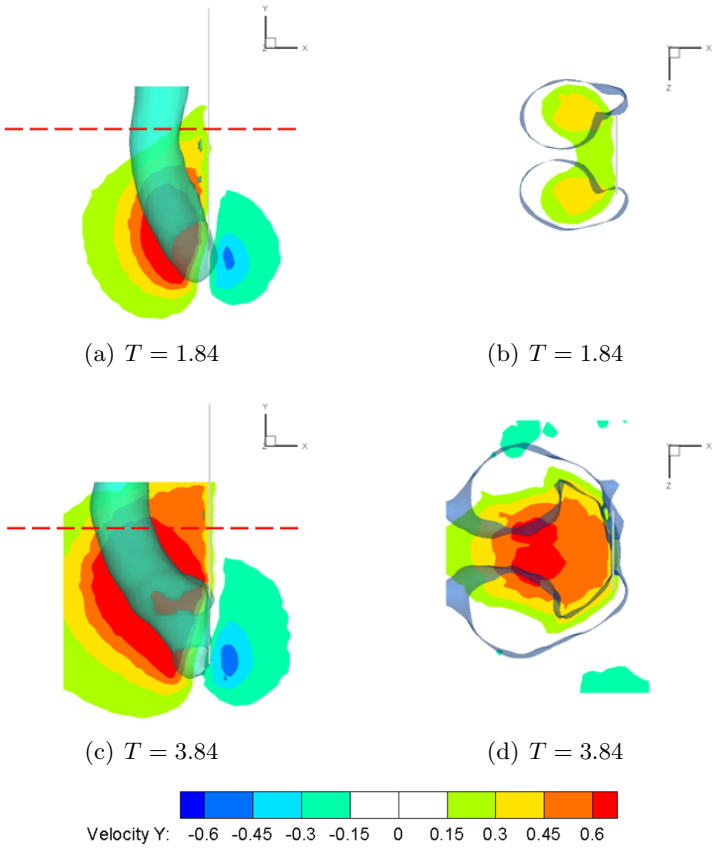

(a) $T = 1.84$ (b) $T = 1.84$

(c) $T = 3.84$ (d) $T = 3.84$

Figure 2.13: Y-directional flow distribution in the flat-rigid plate case. (a) and (c) are side views of $z = 0$ section at $T = 1.84$ and $T = 3.84$. (b) and (d) are top views of a section at $T = 1.84$ and $T = 3.84$, whose y-position is shown in (a) and (c) as a long red dashed line. The contour on the sections is the y-component of the velocity and the three-dimensional transparent surface is the iso-surface of the vorticity magnitude ($|\boldsymbol{\omega}| = 3.2$ for (a) and (c), $|\boldsymbol{\omega}| = 1.6$ for (b) and (d)). Different vorticity magnitudes are chosen to support the explanation in the text better.

move away from the plate, the tip flow gets less entrained by the LEV. Therefore, upward flow becomes more dominant behind the plate, and the TV shifts further up (figures 2.13(c) and 2.13(d)). This observation indicates that upward flow from the tip and its interaction with the LEV has a significant role in early deformation and outward motion of the LEV. In figure 2.13(d), the y-component of the velocity, u_y, inside the LEV core is negligible, and a high magnitude of u_y is observed near the middle section of z-direction. In other words, the region of high tip flow does not coincide with the region of vortex cores.

For the flexible and curved-rigid plate cases, the upward flow near the tip region is replaced by a downward flow behind the plate (figure 2.14). A potential source for this

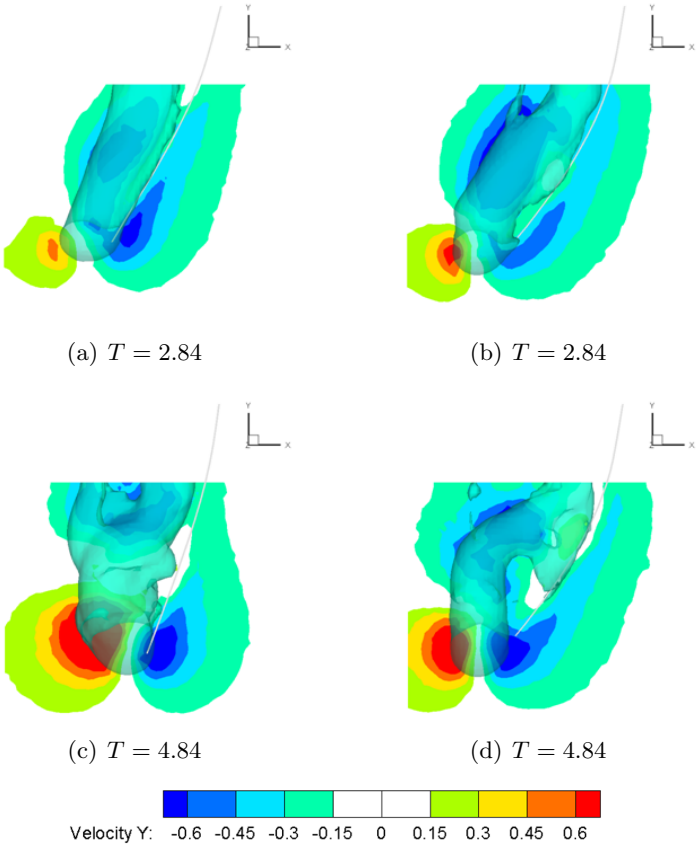

(a) $T = 2.84$ (b) $T = 2.84$

(c) $T = 4.84$ (d) $T = 4.84$

Figure 2.14: Y-directional flow distribution in the flexible plate and curved-rigid cases. (a) and (c) are for the flexible plate case at $T = 2.84$ and $T = 4.84$. (b) and (d) are for the curved-rigid plate case at $T = 2.84$ and $T = 4.84$. All are side views of the section in $z = 0$. Contour on the plane is the y-component of the velocity and the three-dimensional transparent surface is the iso-surface of the vorticity magnitude ($|\boldsymbol{\omega}| = 3.2$).

downward flow in the early stages is the induced flow of the curved vortex that forms along the curved edges of the plates. The direction of flow behind the plate is quite uniform along the curved geometry. It is evident that the entrainment of tip flow by the LEV is not dominant. Therefore, an early separation of the LEV from the plate does not occur in the upper region. Instead, the LEV moves away from the plate first near the lower part where upward tip flow and downward flow meet. This process results in the formation of a vertical horseshoe-shaped vortex near the lower part of the plate. As mentioned in §2.3.1, vortex deformation at the lower region is more apparent in the curved-rigid plate case than in the flexible plate case. Since the LEV of the curved-rigid plate case develops faster than that of the flexible plate after starting, the magnitude of downward flow velocity is larger, which induces more distinct vortex separation from the plate. However, in the flexible plate case, when the plate tip bounces back toward its original position, the tip flow penetrates the region behind the plate. This change of flow pattern may cause a less clear vortex pinch-off process in the lower part of the flexible plate when it is compared to the curved-rigid plate case (figure 2.14).

2.3.3 Vorticity transport

In order to study the vorticity transport of the LEV, first Γ_y was calculated at several y-sections (figure 2.15). Γ_y is defined as $\int_{A(t)} \omega_y \mathrm{d}A$ where $A(t)$ is the total area of a y cross section in the negative z side. Because of the symmetry condition, only one side (negative z) was considered. To avoid including noise in Γ_y calculation, ω_y smaller than 0.5/sec corresponding to non-dimensional value 0.4, was discarded. According to the boundary layer theory, the boundary layer thickness of our model is about 2 mm. This thickness is smaller than the grid size (3 mm). Therefore, during vorticity calculation from velocity vectors, the no-slip condition of the plate could not be imposed accurately. In other words, the size of grids in the experimental data was not fine enough to measure velocity and vorticity fields in the boundary layer region. Thus, some underestimation of Γ_y may be present in figure 2.15. We estimate the order of circulation for the vorticity in the boundary layer. The strength of the boundary layer is $O(U_c)$ (U_c = 50 mm/sec). The half width of the plate $w/2$ is 20 mm. Therefore, the circulation of the boundary layer is about $O(U_c w/2)$ ($=O(10^3$ mm^2/sec)). The corresponding non-dimensional circulation of the boundary layer, which might miss in figure 2.15, is $O(0.5)$.

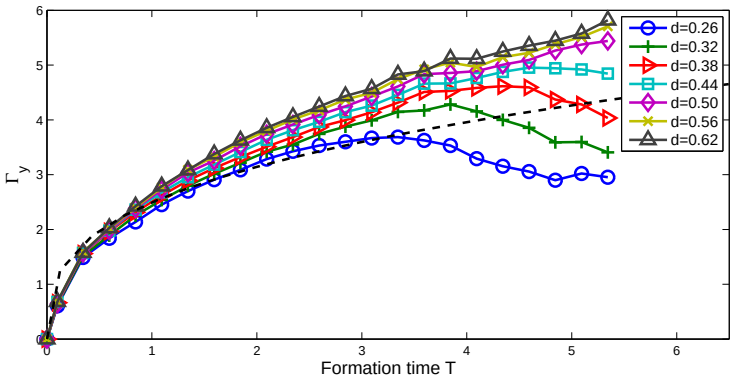

(a)

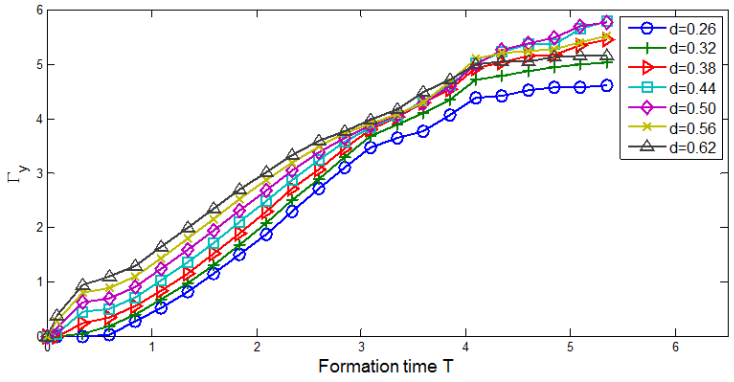

(b)

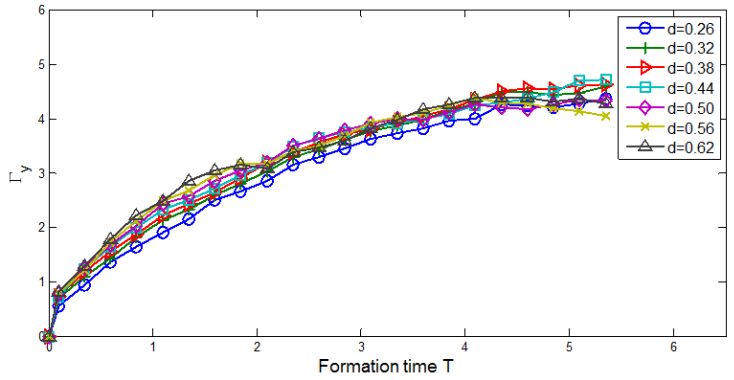

(c)

Figure 2.15: Γ_y at seven y cross sections in three cases; (a) flat-rigid plate, (b) flexible plate, and (c) curved-rigid plate. Values in a legend mean the normalized distance, d, of the section from the tip position (distance from the tip position/total height of the plate immersed in water). The tip position of the flat-rigid plate is also used in the flexible and curved-rigid plate cases. Thus, the same value in the legend means the same y-coordinate of the section (see figure 2.3(a) for the positions of the sections). The dashed line in (a) is from the two-dimensional theory.

For the flat-rigid plate case, Γ_y grows fast when the plate starts impulsively but is then followed by a gradual decrease in the growth rate. While Γ_y in the upper part ($d \geq 0.50$) continues to increase, the growth rate of Γ_y in the lower part ($d \leq 0.44$) becomes almost zero or even negative. Lack of Γ_y in the lower sections does not mean that the y-component of vorticity, ω_y, is not created in the lower part of the plate anymore. Instead, vorticity supplied from the boundary layer in the lower part is lost by convection and tilting processes, which reduce Γ_y in the lower part. A control volume integral can be used in order to estimate the magnitude of ω_y transport. By considering a y cross section in the negative z side as a control surface, we can get the following equation,

$$\frac{\mathrm{d}}{\mathrm{d}t}\int_{A(t)} \omega_y \mathrm{d}A = -\int_{A(t)} u_y \frac{\partial \omega_y}{\partial y}\mathrm{d}A + \int_{A(t)} \left(\omega_x \frac{\partial u_y}{\partial x} + \omega_z \frac{\partial u_y}{\partial z}\right)\mathrm{d}A + \int_{L(t)} \nu \frac{\partial \omega_y}{\partial n}\mathrm{d}L \quad (2.3)$$

where $A(t)$ is the whole fluid area of one side (negative z) at a y-section, $L(t)$ is the plate boundary on $A(t)$, and n is the normal vector into the plate. The term on the left-hand side is the growth rate of Γ_y at a y-section. The first term on the right-hand side, including the negative sign, means the growth rate of Γ_y by convection across that y-section. The second term is the growth rate of Γ_y by tilting into the xz-plane, and the last term is total ω_y flux from the plate surface at that y-section, the source of vorticity. It is assumed that net diffusion across the y-section is negligible. ω_y supplied from the boundary can be transported by convection across the y-section, or by tilting into the xz-plane. The circulation from the two-dimensional theory was also plotted in figure 2.15(a) (Pullin & Wang, 2004). Before $T < 0.5$, the circulation from the two-dimensional theory is larger. The gap is mainly because of the different kinematics of the plate. In the theory, the plate accelerates impulsively and reach the constant velocity at $T = 0^+$ while the plate accelerates for 0.25 sec. Also, as mentioned above, the underestimation of the circulation in the boundary layer may cause the gap between the experiment and the theory. As T increases, the circulation from the 2D theory underestimates the circulation of the flat-rigid plate, the Γ_y curve of $d = 0.62$ in figure 2.15(a). Γ_y at $d = 0.62$ is not affected by the dynamical change of vortex structure near the tip as much as Γ_y of the other sections. The theory is based on the assumption that the rolled-up vortex sheet is self-similar for small times, which is not valid as the vortex becomes large. Also the effect of the vortex in the other edge is neglected in the theory. As the strength of the vortex increases, the effect of

the counter-rotating vortex in the other edge should be considered.

Figure 2.16 shows the effect of vorticity transport in the flat-rigid plate case. Threshold values of ω_y and u_y were applied to obtain the growth rate of Γ_y by convection or tilting at y-sections; $\omega_y > 0.5$/sec and $|u_y| > 2$ mm/sec. Instead of detailed quantitative analysis, we focus on the characteristics of curves in figure 2.16. While the net vorticity transport is negligible up to $T = 1.5$, Γ_y loss by tilting rather than by convection increases considerably in the lower part of the plate after $T = 1.5$. The upper part does not have any noticeable net vorticity transport during the full observation time in this experiment. When tilting rates at $d = 0.26$ and 0.34 increase after the lowest peak, tilting rates at $d = 0.40$ and 0.48 have the lowest peaks in turn. This means a significant tilting motion of the LEV happens from the lower section to the upper section, which is accompanied by the upward motion of the TV. The loss and gain behavior of Γ_y in figure 2.16 supports the qualitative discussion on the vortex deformation presented in §2.3.1.

In the flexible plate case, the initial slope of Γ_y is not as large as that of the rigid plate case, especially in the lower part (figure 2.15(b)). When the plate starts to move, the upper part moves faster than the lower part; therefore, the LEV grows first in the upper part. Thus, Γ_y at y-sections are different at early time. In the curved-rigid plate case, the initial slope is comparable to that of the flat-rigid plate case (figure 2.15(c)). However, after $T = 2$, the growth rate of Γ_y becomes smaller than that of the flat-rigid plate case. Unlike the flat-rigid plate case, the flexible plate and curved-rigid plate cases do not show significant divergence of Γ_y curves. Therefore, it can be inferred that Γ_y gain or loss by vorticity transport is not a dominant process. In both rigid plate cases, vorticity supply from the boundary layer into the vortex diminishes and, thus, the circulation slope becomes less steep after the LEV grows considerably by an impulsively starting motion early on ($T < 0.5$). However, in the flexible plate case, Γ_y continues to grow without slowing down its growth rate at the early formation time. The slope of Γ_y is larger than that of the rectangular plate case from $T = 1.5$ to $T = 4$. Even though the development of the vortex is delayed initially, the vortex grows fast afterward, and its strength becomes comparable to that of the rigid plate case. In addition, when the flexible plate bounces back to its original shape, it may create more ω_y since the forward velocity of the tip is larger than when the plate is in maximum deformation and the downward velocity component in front of the plate by the downwash effect of the LEVs is reduced.

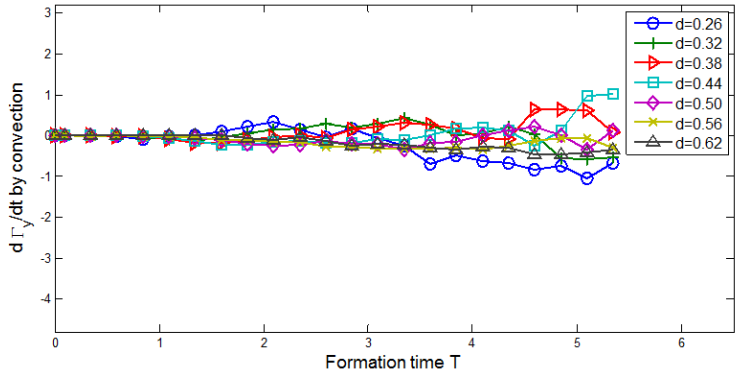

(a)

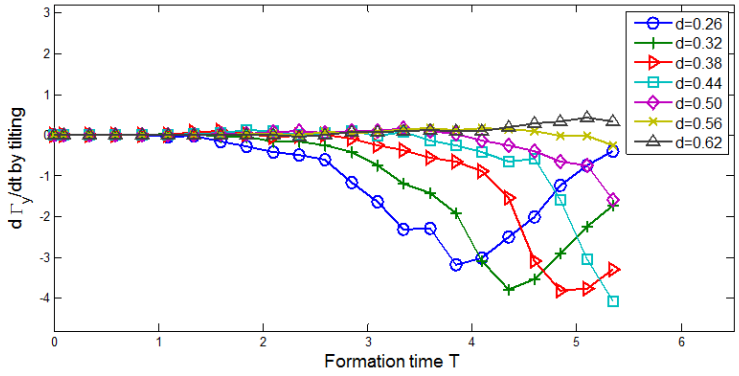

(b)

Figure 2.16: Vorticity transport rates in the flat-rigid plate case; (a) Γ_y convection and (b) Γ_y tilting. (a) and (b) correspond to the first two terms on the right-hand side in Eq. 2.3 including the negative sign in front of the term. The negative value in the graphs means Γ_y loss at the section.

2.3.4 Correlation between hydrodynamic force and vortex formation

The hydrodynamic force acting on a body can be obtained from vorticity field data without the need to know the pressure and shear stress on the body. For three-dimensional viscous flow, which rests at infinity, Wu (1981) derived

$$\boldsymbol{F} = -\frac{\rho}{2}\frac{\mathrm{d}}{\mathrm{d}t}\int_{V_\infty} \boldsymbol{x} \times \boldsymbol{\omega}\mathrm{d}V + \rho\frac{\mathrm{d}}{\mathrm{d}t}\int_{V_b} \boldsymbol{u}\mathrm{d}V \tag{2.4}$$

where V_b and V_∞ are body volume and total volume including the body, respectively.

In the Euler limit of viscous flow ($\mathrm{Re} \to \infty$), added-mass reaction force by linear acceleration can be calculated from Eq. 2.4 (Leonard & Roshko, 2001). A solid body can be replaced by the proper vorticity distribution inside the body volume and on the body surface to have the same velocity field in the fluid volume. Then, during acceleration, an incremental velocity ΔU_b of the object proportionally changes the instantaneous strength of the vorticity inside the body volume and on the body surface to satisfy the no-through boundary condition. Therefore, in Eq. 2.4, the first term integrated inside the body volume and on the body surface, as well as the second term, is proportional to $\mathrm{d}U_b/\mathrm{d}t$. The sum of these two terms is added-mass force. To calculate the total force acting on the body, the first term integrated outside the body volume should be included as well.

If the vorticity is confined in a closed loop of thin vortex filament of circulation Γ, the first term of Eq. 2.4 is reduced to

$$\boldsymbol{F} = -\rho(\dot{\Gamma}\boldsymbol{S} + \Gamma\dot{\boldsymbol{S}}) + \rho\frac{\mathrm{d}}{\mathrm{d}t}\int_{V_b} \boldsymbol{u}\mathrm{d}V \tag{2.5}$$

where $\boldsymbol{S}$ is the surface vector spanned by the closed loop (Wu *et al.*, 2006). $|\boldsymbol{S}|$ is the area of the minimum surface spanned by the loop. In order to apply Eq. 2.5 to our case, first it should be assumed that the effect of a free surface is negligible and a symmetric flow field can be mirrored across the free surface to have an infinite flow field. The last term of Eq. 2.5 is negligible because the thickness of the plates is small and the traverse driven by the motor moves with a constant velocity after initial acceleration. A three-dimensional vortex is composed of three-dimensional thin vortex filaments. This concept was used in the lifting line theory of traditional aerodynamics. It is also analogous to the concept of using point vortices composing a vortex sheet in the two-dimensional case. However, for

qualitative analysis, it is easier to consider one vortex (a collection of vortex filaments), instead of individual vortex filaments. For the vortex of the frontal area S_x and strength Γ, the drag D, the force acting on the plate in the negative x-direction, can be expressed approximately as

$$D(t) \approx \rho(\dot{\Gamma} S_x + \Gamma \dot{S_x}). \tag{2.6}$$

Growth of vortex strength and frontal area contributes to the drag force. Vortex filaments created on the plate are added to the vortex, which increases the strength of the vortex and contributes to the drag force. The second term of Eq. 2.5 is negligible in our *thin* plate model with 90° angle of attack. During acceleration, the force peak of the second term is much smaller than that of the first term in Eq. 2.4. For the validation of Eq. 2.6 and the effect of the neglected boundary layer on the accuracy of Eq. 2.6, refer to Appendix B.

Figure 2.17 is the graph of the drag measured by the load cell. In the flat-rigid plate and curved-rigid plate cases, drag decreases rapidly after the initial peak and has a plateau after about $T = 2.5$. The drag of the flat-rigid plate stays higher than that of the curved-rigid plate. For the flexible plate case, the magnitude of the initial peak is not as large as the other cases since only the upper part moves at first. Instead, drag increases again after the initial peak until $T = 1$ and stays constant during $T = 1 \sim 4$. It drops after $T = 4$ and lies between the drag curves of the other cases. It is interesting to note that the drag of the flexible plate case is comparable to that of the flat-rigid plate case during $T = 1 \sim 4$ even though the plate is curved. If the instantaneous frontal area of the plate is used in the definition of the drag coefficient instead of the immersed area, the drag coefficient of the flexible plate case is higher than that of the flat-rigid plate case during $T = 2 \sim 4$; however, the drag coefficient of the curved-rigid plate is not higher than that of the flat-rigid plate even if the instantaneous frontal area of the plate is used.

The circulation rate of the vortex system, $\dot{\Gamma}$ in Eq. 2.6, can be obtained from Γ_y curves in figure 2.15. In the uppermost section of the plate, Γ_y is relatively free from tilting or growth delay. Thus, the rate of circulation ($\dot{\Gamma}$) of the vortex can be approximated with the slope of Γ_y in the uppermost section. In the flat-rigid plate case, the slope of Γ_y in the uppermost section drops significantly after the acceleration time and decreases gradually. This trend is reflected in the drag curve in figure 2.17. Even though the circulation slope decreases gradually, the drag maintains almost constant value after $T = 2$. In fact, the increase of the

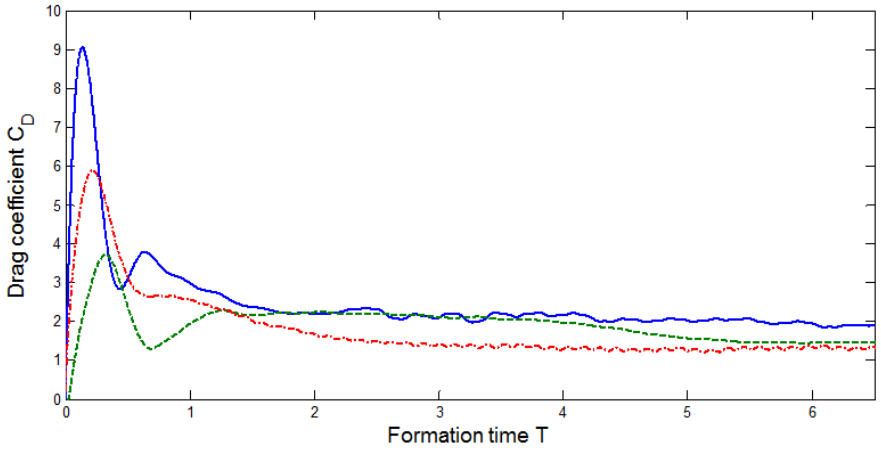

Figure 2.17: Drag coefficients of the flat-rigid, flexible and curved-rigid plate cases. A continuous line is for the flat-rigid plate; a dashed line is for the flexible plate; a dash-dotted line is for the curved-rigid plate.

vortex frontal surface ($\dot{S}_x > 0$) is responsible for the drag plateau (see Eq. 2.6 and figure 2.5). the LEV moves outward in z-direction, which results in positive $\dot{S}_x$. However, while the LEV moves outward, some portion of the TV also moves upward to reduce S_x (figure 2.5). Thus, the net effect of the frontal surface change on drag is decreased by the upward TV motion. In the curved-rigid plate case, the circulation slope drops rapidly after starting, and it remains smaller than that of the flat-rigid plate case. After $T = 3.84$, the increase of the vortex frontal surface (figure 2.9) compensates for the decrease of the circulation growth rate, which finally results in nearly constant drag.

The drag of the flexible plate shows the trend distinctly different from those of the other cases. The initial peak of the drag in the flexible plate case is not as high as the rigid plate cases. This can be correlated with the fact that the vortex structure, early on, has a small frontal area. However, this vortex expands its frontal surface S_x when vortex sheets connecting two LEVs on the front side of the plate expand toward the tip and finally form the TV near the tip. This expansion of the frontal surface contributes to the drag increase (figures 2.11 and 2.18). In other words, the flexible plate distributes its drag over a large time interval instead of having a large peak during acceleration, and the increase of the vortex frontal surface by moving the vortex toward the tip plays an important role in drag generation at an early formation time. Perhaps, this observation can be used to explain why it maintains a drag value as high as that of the flat-rigid plate during $T = 1 \sim 4$. During

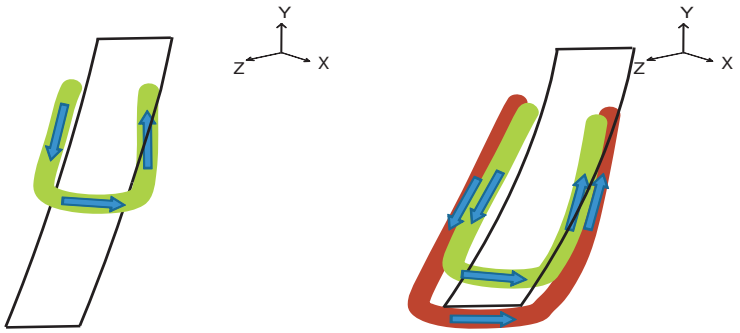

(a) $T = 0.84$ (b) $T = 3.34$

Figure 2.18: Simple vortex tube representation of figure 2.11 (flexible plate case) in the view toward the plate front. While a dark vortex tube is generated from the plate between (a) and (b), a light vortex tube of (a) expands its frontal surface area toward the tip. Arrows indicate the direction of vortices following a right-hand rule. Vortices on the top regions are not shown.

the early formation time, the already-created vortex filaments present for the rigid cases do not contribute to the drag as significantly as the flexible plate case due to their small $\dot{S}_x$. However, in the flexible plate case, they can increase the drag force by enlarging their frontal surface area toward the tip. The completion of vortex frontal surface expansion toward the tip may be one of the reasons that the drag value drops after $T = 4$. The force trend of the flexible plate case depends on bending stiffness of the plate. Thus, the trend shown in this study cannot be applied to plates with different rigidity without careful investigation.

2.4 Concluding remarks

Vortex formation processes of low aspect-ratio plates show distinct differences among three cases reported here. The main distinction between the flat-rigid plate case and the flexible or the curved-rigid plate cases is in the presence of a large upward flow that originates at the tip and moves up along the backside of the plate. The presence of this upward flow from the tip region causes early deformation and outward motion of the LEV in the upper region of the flat-rigid plate. In the flexible and curved-rigid plate cases, vortex pinch-off occurs first near the tip followed by the formation of a horseshoe-shaped vertical vortex. Previous researchers (Ellington *et al.*, 1996; Maxworthy, 1979) have reported that the presence of spanwise flow from the base to the tip on the suction side of the hovering insect's wing stabilizes LEV attachment to the wing. In the cases studied here, the flow from the tip

(upward flow) induces vortex separation and deformation rather than retaining the vortex near the edge of the plate. Unlike the wing of hovering insects, our models undergo only a translating motion and the surface of the model is perpendicular to the moving direction. In this respect, the interaction of the LEV and nearby axial flow depends on the kinematics of the model.

The amount of vortex core deformation is varied by the position of the vortex core and the dynamics of nearby vortex parts. When the vortex can move outward freely after separation from the plate, such as in the upper part of the LEV of the flat-rigid plate case, the vortex core would be able to maintain its original circular shape. In contrast, if the inward motion of the vortex is restricted because of the symmetry condition like the upper part of the LEV of the flexible plate and curved-rigid plate cases, the vortex core would go through severe elongation along the moving direction.

The drag coefficient value for the maximally deformed flexible plate is significantly different from that of the curved-rigid plate of similar curvature. This implies that the history of a flow field should be considered in order to understand the hydrodynamic force generation at any given time. For the flexible plate case, the initial peak of the drag is not as large as the other cases. But, it could maintain high drag values for a long time despite its curved shape. From this study, it was revealed that the slow development of the vortex system is related to this notable drag trend. An animal with a flexible flapper may be able to avoid the large initial peak of hydrodynamic force at sudden motion and at stroke reversal by slowing down growth of the vortex. This would be beneficial to maintain the constant propulsive force during power strokes, avoid the structural fatigue due to repeated strokes, and reduce the excessive demand of muscle work for abrupt stroke conditions. It would be interesting to study how the flexible flapper influences the three-dimensional vortex system around the flapper and the thrust performance when the animal starts to move impulsively.

Chapter 3

Paddling propulsion

3.1 Background

The locomotion mechanism of flapping animals can be categorized into two modes: lift-based and drag-based propulsions (Vogel, 2003; Alexander, 2003). In lift-based propulsion, most propulsive force acts perpendicularly to the moving direction of the flapper with a small angle of attack. Meanwhile, in drag-based propulsion with a large angle of attack such as paddling and rowing modes, the propulsive force acts on the flapper mainly in the direction opposite the moving direction of the flapper. Vogel (2003) conjectured that the lift-based propulsion mode was more efficient in high speed locomotion establishing why fast-moving flapping animals employed this mode. He also argued that the drag-based mode was effective in low speed locomotion in that it could generate large thrust over a short time. Therefore, the drag-based propulsion mode is preferred in maneuvering behaviors such as acceleration, turning, and braking (Walker & Westneat, 2000).

The traditional fixed-wing aerodynamic theory has been successfully used in the past to explain the principle of lift-based propulsion. However, this approach is not suitable for drag-based propulsion. In order to study thrust and mechanical efficiency of drag-based propulsion, the blade-element approach has been used in the pectoral fin motion of the angelfish (Blake, 1979, 1980) and the threespine stickleback (Walker, 2004). On the other hand, the vortex formation process has been investigated to find its relation to kinematics and propulsive performance of animals (Ellington *et al.*, 1996; Birch & Dickinson, 2001; Dabiri & Gharib, 2005b). Also in the drag-based propulsion mode of fish, vortex structures were identified experimentally and used to derive hydrodynamic force acting on the fish (Drucker & Lauder, 1999; Epps & Techet, 2007). However, the unsteady vortex formation

process of drag-based propulsion has not been addressed adequately.

Here, we analyze vortex formation and its relation with thrust generation by using a simple mechanical model mimicking the power stroke of drag-based propulsion. In order to map the three-dimensional flow field around our model and identify a vortex structure, defocusing digital particle image velocimetry (DDPIV) was used (Willert & Gharib, 1992; Pereira & Gharib, 2002; Pereira *et al.*, 2006; Lai *et al.*, 2008). First, we focused on the effect of model shape and flexibility on thrust performance. We also compared flow structures between two different Reynolds number regimes of $O(10^2)$ and $O(10^4)$. Furthermore, we explored whether there is an optimal stroke angle for efficient thrust generation and identified flow phenomena that affect the relation between the stroke angle and thrust generation process.

The fundamental difference in vortex formation mechanism between lift-based propulsion and drag-based propulsion can be better understood by examining the relationship between force generation and flow field. The hydrodynamic (aerodynamic) force acting on a moving object inside an infinite flow field can be derived from vorticity distribution of the flow field and velocity of the object (Wu, 1981).

$$\boldsymbol{F} = -\frac{\rho_f}{2}\frac{\mathrm{d}}{\mathrm{d}t}\int_{V_\infty} \boldsymbol{x}\times\boldsymbol{\omega}\mathrm{d}V + \rho_f\frac{\mathrm{d}}{\mathrm{d}t}\int_{V_b}\boldsymbol{u}\mathrm{d}V, \tag{3.1}$$

where ρ_f is fluid density, V_∞ is an infinite flow field, and V_b is body volume. If vorticity is confined in a closed vortex loop of circulation (Γ) and the object is thin, Eq. 3.1 can simply be approximated as follows (Wu *et al.*, 2006),

$$\boldsymbol{F}(t) \approx -\rho_f\frac{\mathrm{d}}{\mathrm{d}_t}(\Gamma\boldsymbol{S}) = -\rho_f(\dot{\Gamma}\boldsymbol{S} + \Gamma\dot{\boldsymbol{S}}). \tag{3.2}$$

$\boldsymbol{S}$ is the vector of the minimum surface spanned by the vortex loop and $|\boldsymbol{S}|$ is the area of the surface. If propulsive force (F_p) is applied on the object in the negative x-direction,

$$F_p(t) = -F_x(t) \approx \rho_f(\dot{\Gamma}S_x + \Gamma\dot{S}_x), \tag{3.3}$$

where S_x is the area of S projected on the yz-plane. Eqs. 3.2 and 3.3 show that the increase in the area enclosed by the vortex loop ($\dot{\boldsymbol{S}}$ and $\dot{S}_x$) and the growth of circulation ($\dot{\Gamma}$) are correlated with force generation. Figure 3.1 illustrates two simple examples of force

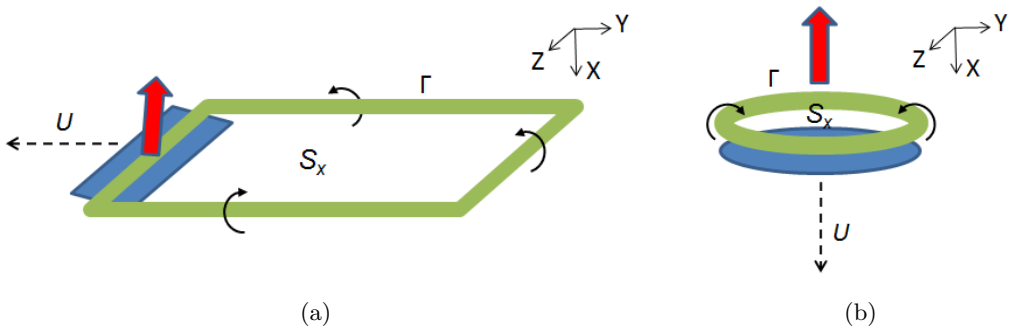

(a) (b)

Figure 3.1: Vortex structures in (a) lift-based propulsion and (b) drag-based propulsion. The thick green line is the vortex generated by a moving object. The curved arrows around the vortex show the rotating direction of the vortex. The dashed black arrow indicates the moving direction of the object. The thick red arrow indicates the direction of force acting on the object.

generation modes: lift-based propulsion and drag-based propulsion. When a flying animal glides with a constant speed and a small angle of attack (figure 3.1(a)), the circulation of the vortex structure is assumed to be constant in time; the first term ($\dot{\Gamma} S_x$) in the right-hand side of Eq. 3.3 is neglected in lift generation. To apply Eq. 3.3 to drag-based propulsion, we first consider the example of a falling circular disk whose face is perpendicular to the falling direction (figure 3.1(b)). Vorticity is assumed to be created at the edge of the disk and the vortex is rolled up around the edge of the disk. In this case, while the inner area of the vortex loop can be assumed to be approximately constant, the circulation growth of the vortex loop cannot be neglected, and the first term ($\dot{\Gamma} S_x$) of Eq. 3.3 contributes significantly to the lift generation of the falling disk. For drag-based propulsion modes such as paddling and rowing in which the propulsor rotates with a joint, the temporal change of a vortex inner area projected in the thrust direction should also be taken into consideration.

3.2 Experimental setup

3.2.1 Models and kinematic conditions

A plate used as a propulsor was attached to a micro-stepping stepper motor (NEMA 14 and IM483, Schneider Electric Motion). Transparent glass plates with thickness 1.15 mm and density ρ_m 2.56 g/cm^3 were used as rigid flappers. For the animals in the drag-based mode, the shapes of the propulsors are diverse. In this study, three simple shapes (rectangle,

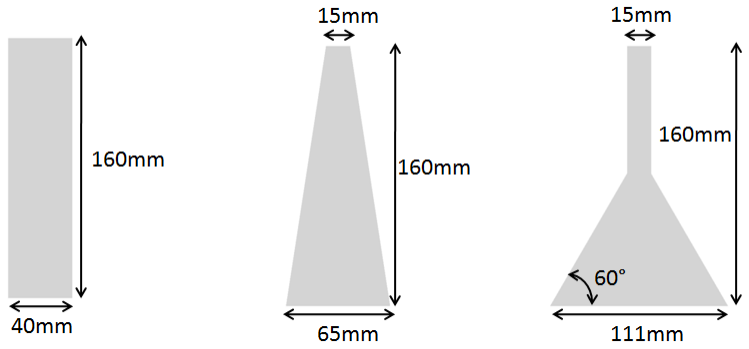

(a) (b) (c)

Figure 3.2: Shapes of three plates; (a) rectangular plate, (b) triangular plate, and (c) delta-shaped plate for a duck's feet.

triangle, and delta shape) were considered (figure 3.2). All plates had the same area of 6400 mm^2, but the ratio of the plate width in the base to the width in the tip is different. The delta-shaped plate was chosen to represent the propulsor such as a duck's foot, which has a much larger area near the tip than near the base. The span length s from the base to the tip was 160 mm for all plates. The width of the rectangular plate was 40 mm. The widths of the tip and the base in the triangular plate were 65 mm and 15 mm, respectively. The end part of the delta-shaped plate was the equilateral triangle 111 mm wide near the tip. The width of the region connecting the base and the equilateral triangle was 15 mm. The glass plates were assumed rigid. In addition, for flexible plates, transparent polycarbonate plates (Young's modulus $E = 2.3$ GPa, density $\rho_m = 1.2$ g/cm^3) with thickness 1.52 mm, 1.02 mm, and 0.76 mm were used.

The plate was immersed into a glass tank of $870 \times 430 \times 360$ mm^3, and it was rotated by the stepper motor (figure 3.3). Two angular velocity programs, trapezoidal and sinusoidal angular velocity programs, were used for rotation of the stepper motor (figure 3.4). A stroke time (T) was 2.4 sec and a stroke angle (ϕ) was 106° for both programs. After 2.4 sec, the plate stayed at the final position of the power stroke. For all simulations, only one power stroke was simulated. In the trapezoidal velocity program, the motor accelerates for 0.125 sec, maintains a constant angular velocity for 2.15 sec, and decelerates its rotation for the last 0.125 sec. To study flow fields of two different Reynolds numbers , water ($\nu =$ 1 mm^2/sec, $\rho_f = 1.00$ g/cm^3) for high Re and mineral oil (Chevron Superla white oil, $\nu =$

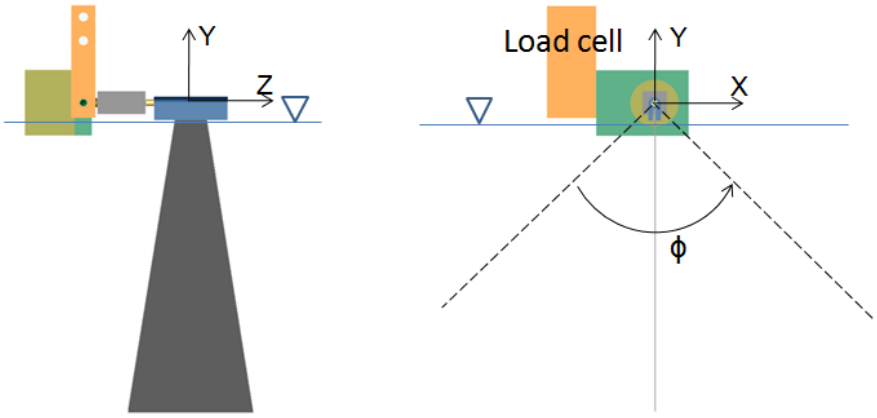

(a) Back view (b) Side view

Figure 3.3: Schematic of the model. The plate rotates for a stroke angle ϕ with respect to the z-axis. The rotating axis of the motor is 10 mm above the free surface.

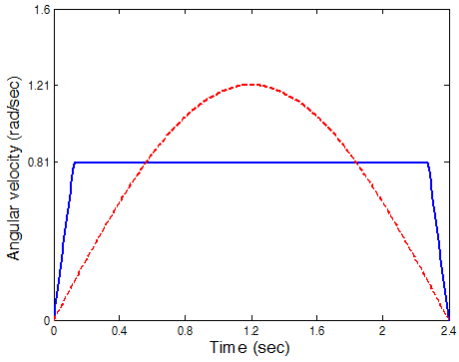

Figure 3.4: Trapezoidal (continuous line) and sinusoidal (dashed line) angular velocity programs.

Plate shape	Rectangle, triangle, and delta-shape
Plate material	Glass (thickness 1.15 mm) and polycarbonate (thickness 1.52 mm, 1.02 mm, and 0.76 mm)
Reynolds number Re	19720 and 140
Angular velocity program	Trapezoid and sinusoid
Stroke angle ϕ	106°
Stroke time T	2.4 sec

Table 3.1: Summary of the model conditions considered in this study.

140 mm^2/sec, $\rho_f = 0.84$ g/cm^3) for low Re were used as a working fluid inside the tank. The Reynolds number (Re $= Us/\nu$) was 19720 for high Re and 140 for low Re. The span length s was used as a characteristic length for Re since our main interest is the tip vortex structure at the tip edge of the plate. The characteristic velocity U for Re is where Ω is the mean angular velocity of the motor during a stroke. In the rigid plate case, U is the same as the mean tip velocity of the plate. In the following sections, the Reynolds number of the model is 19720 unless it is stated specially. The model conditions are summarized in table 3.1.

3.2.2 Defocusing DPIV and force measurement

DDPIV was conducted to map three-dimensional flow generated by a rotating plate. Here, important processing steps are briefly explained. The DDPIV camera was placed in front of the tank. The distance between the camera and the tank was adjusted to place the camera probe volume in the middle of the tank. The tank was seeded with silver-coated glass spheres of mean diameter 100 μm (Conduct-o-fil, Potters Industries Inc.). An Nd:YAG laser (200 mJ/pulse, Gemini PIV, New Wave Research Inc.) illuminated glass sphere particles. The time gap between two laser pulses to take a pair of images was 25 msec. The control computer sent trigger pulses to synchronize operation of the DDPIV camera and the laser, and controlled the stepper motor motion.

First, three-dimensional coordinates of the particles inside the tank were found by matching particle images in three images captured by the DDPIV camera. Then, from the position information of the particles, velocity vectors of the particles were calculated from a relaxation method of 3D particle tracking (Pereira *et al.*, 2006). The camera probe volume was not large enough to include the whole vortex structure. Thus, three sets of

the experiment were performed by translating the initial position of the model 80 cm and 160 cm parallel to the tank wall. Thus, the total fluid volume mapped by three sets of the experiment was $280 \times 160 \times 160$ mm^3. To increase the density of randomly-spaced velocity vectors in a fluid domain, the experiment was repeated 25 times under the same conditions with an interval of 90 sec. For each time frame, the velocity vectors from 25 cases were collected and fitted into grids of $3 \times 3 \times 3$ mm^3 to obtain a velocity field. The vorticity field was obtained by a central difference scheme from the velocity field data. The time step between frames was 0.2 sec.

For thrust force measurement, a load cell (miniature beam type, Interface Inc.) was attached to the top of the motor (figure 3.3). The load cell measured the force acting on the plate in the x-direction. The signal was amplified and low-pass filtered with 5 Hz cutoff frequency through a signal conditioner (SGA, Interface Inc.). Thrust coefficient C_T and non-dimensional impulse I_x were obtained from the filtered signal.

$$C_T(t) = -\frac{F_x(t)}{\frac{1}{2}\rho_f U^2 \hat{r}_2^2 A} \quad \text{and} \quad I_x(t) = \frac{\int_0^t C_T(\tau)\mathrm{d}\tau}{T}, \tag{3.4}$$

where U is $s\Omega$, A is the area of the plate, T is the total stroke time of the plate, and $\hat{r}_2^2$ is the non-dimensional second moment of plate area with respect to the rotating axis. Non-dimensional total impulse I_∞ is the impulse as t goes to ∞ in Eq. 3.4.

Variables such as time, velocity, vorticity, and circulation were non-dimensionalized with a proper choice of the rotation time T, the span length s, and the velocity U, which is the mean tip velocity in the rigid plate case; $t = t_d/T$, $\boldsymbol{u} = \boldsymbol{u}_d/U$, $\boldsymbol{\omega} = \boldsymbol{\omega}_d s/U$, and $\Gamma = \Gamma_d/Us$, where a subscript d means a dimensional variable. Matlab (The Mathworks Inc.) was used to obtain circulation ($\Gamma_d = |\int_\mathrm{A} \omega_z \mathrm{dA}|$) of the tip vortex at the $z = 0$ plane. A is the whole section of the $z = 0$ plane. The main vorticity component of the tip vortex at the $z = 0$ plane is negative ω_z. To avoid including noise in Γ_d calculation, a threshold value of ω_z was set; $\omega_z < -0.23$.

For the flexible plate cases, bending stiffness and density of the plate are important parameters in the interaction of a deformable plate and fluid. Two non-dimensional numbers can be induced with these parameters to characterize the fluid-deformable structure interaction problem. Here, non-dimensional bending stiffness is defined as $EI = (EI)_d/\rho_f U^2 s^3$ where $(EI)_d$ is the dimensional bending stiffness per unit width. EI is 10.9, 3.2 and 1.4

for flexible polycarbonate plates with thickness 1.52 mm, 1.02 mm, and 0.76 mm in water. This non-dimensional parameter indicates relative magnitude of plate bending shear force with respect to fluid inertial force. Another non-dimensional parameter ρ_m/ρ_f represents the ratio of inertial force of the deforming plate to fluid inertial force.

3.3 Results and Discussion

3.3.1 Role of spanwise flow on tip vortex formation

Vortices generated by the power stroke of rectangular, triangular, and delta-shaped glass plates are compared in figure 3.5 for the trapezoidal angular velocity program. One distinct difference among these three cases is the nature of the tip vortex motion. During the stroke, the position of the tip vortex is the lowest along the y-direction in the delta-shaped plate case and the highest in the rectangular plate case. For the delta-shaped plate case, soon after the propulsor starts the power stroke, the tip vortex near the tip edge of the plate separates from the tip edge and moves outward from the tip edge. Meanwhile, the tip vortex for the rectangular plate case relatively follows the trajectory of the tip edge without significant outward motion.

Spanwise flow distribution behind the rotating propulsor is shown in figure 3.6 at $t = 0.5$ when the propulsor surface is parallel to the y-axis. Spanwise flow is the flow that has the velocity component parallel to the plate span. Outward spanwise flow from the base to the tip is strong and widely distributed for the delta-shaped plate case, compared to the other cases. Spanwise flow occurs mainly in the center region between two side-edge vortex cores. The trends of tip vortex motion and spanwise flow distribution mentioned here were also observed for the sinusoidal angular velocity program cases.

The outward motion of the tip vortex is enhanced by spanwise flow behind the propulsor. Spanwise flow is mainly distributed in the central region between cores of side-edge vortices. The spanwise flow induced by the propulsor's motion interacts with the tip vortex and pushes it outward from the tip edge. Once the tip vortex starts to move away from the tip edge, the motion of the tip vortex is less influenced by the motion of the plate. After the separation of the tip vortex, spanwise flow also interacts with the thin vortex sheet shedding from the tip edge and pushes it outward as well. As the tip edge is wider, the tip vortex tends to move farther away from the tip edge during rotation. In the delta-shaped

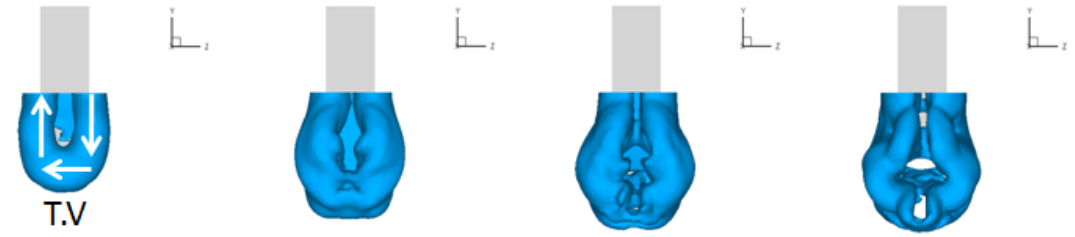

(a) Rectangular plate

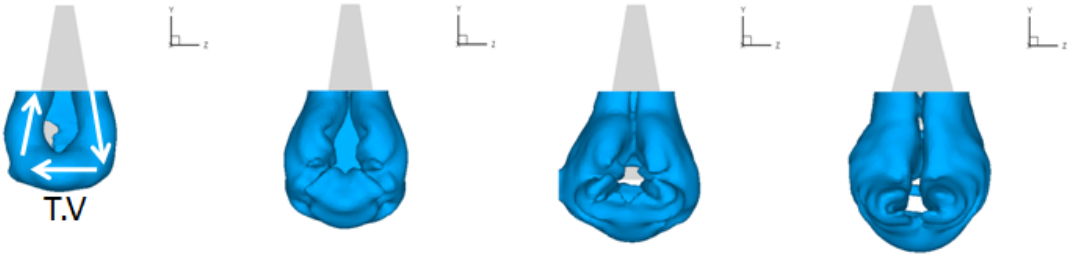

(b) Triangular plate

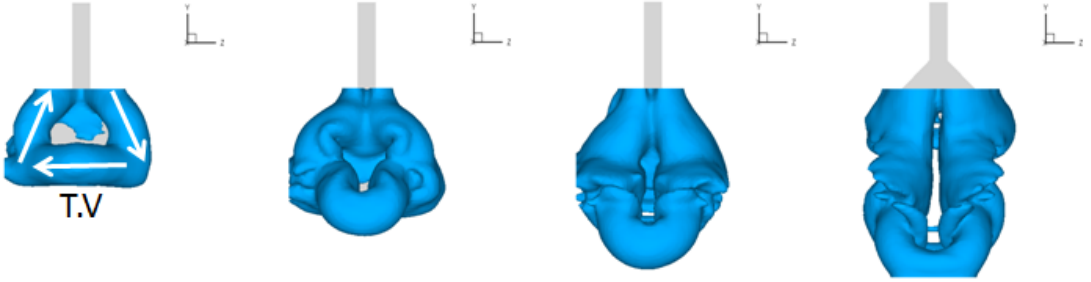

(c) Delta-shaped plate

Figure 3.5: Vortex structures for three propulsors with different shapes in back view. From left to right, the vortex formation process is shown at four time steps ($t = 0.25$, 0.50, 0.75, 1.00). Iso-surfaces of vorticity magnitude ($|\boldsymbol{\omega}| = 6$) are used. The white arrows show the rotating direction of the vortex with the right-hand rule. $T.V$ in the subfigures means the tip vortex generated near the tip.

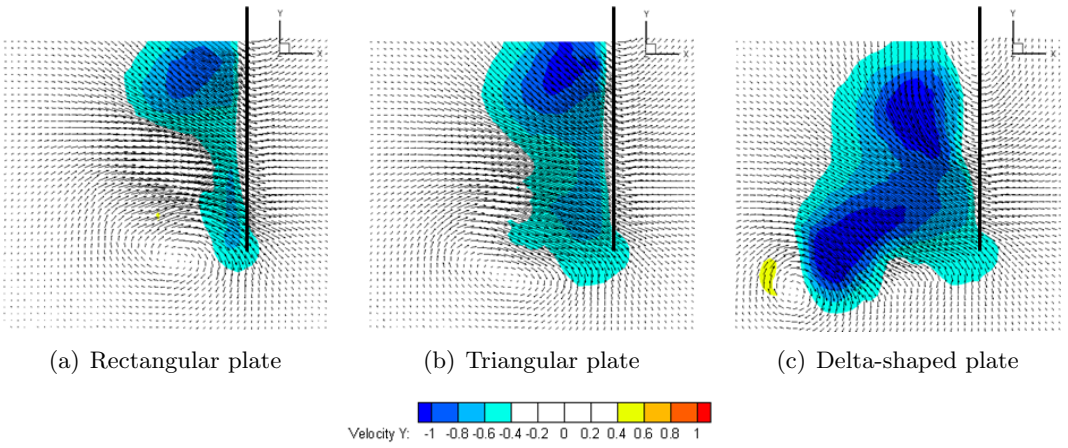

(a) Rectangular plate (b) Triangular plate (c) Delta-shaped plate

Figure 3.6: Spanwise flow distribution for three propulsors with different shapes at $t = 0.50$ (side view). Velocity vectors and velocity y contours are plotted on the symmetrical $z = 0$ plane.

propulsor, side edges are not perpendicular to the tip edge, and thus the side-edge vortices can contribute significantly to the development of spanwise flow.

Figure 3.7 shows thrust coefficients obtained from load cell measurement for rigid glass plates for the shapes studied here. The three cases do not show a significant difference in thrust coefficients, especially for the trapezoidal velocity program. In Eq. 3.4, the non-dimensional second moments of the plate area $\hat{r}_2^2$ are 0.33 (rectangle), 0.44 (triangle), and 0.56 (delta-shape). Therefore, the delta-shaped plate case generates the largest force during the power stroke. According to Eq. 3.1, the outward motion of the tip vortex in the delta-shaped plate case contributes to the increase of thrust ($-F_x$) by enlarging the inner area enclosed by the vortex structure projected on the yz-plane. However, one should also notice that, in the delta-shaped plate case, side-edge vortices near the tip tend to move inward, which reduces the inner area of the vortex. These arguments do not mean that the difference in thrust magnitude among the three cases is purely due to the difference in tip vortex motion. To relate thrust and vortex structure, vorticity distribution of the whole vortex structure instead of the tip vortex alone should be taken into consideration.

The role of spanwise flow mentioned in this paper is different from the role of spanwise flow for leading-edge vortex stabilization in hovering insects. In the hovering insect case, it is important to maintain the leading-edge vortex on the wing of hovering insects for high lift generation, and spanwise flow has a role in stabilizing the leading-edge vortex by transport-

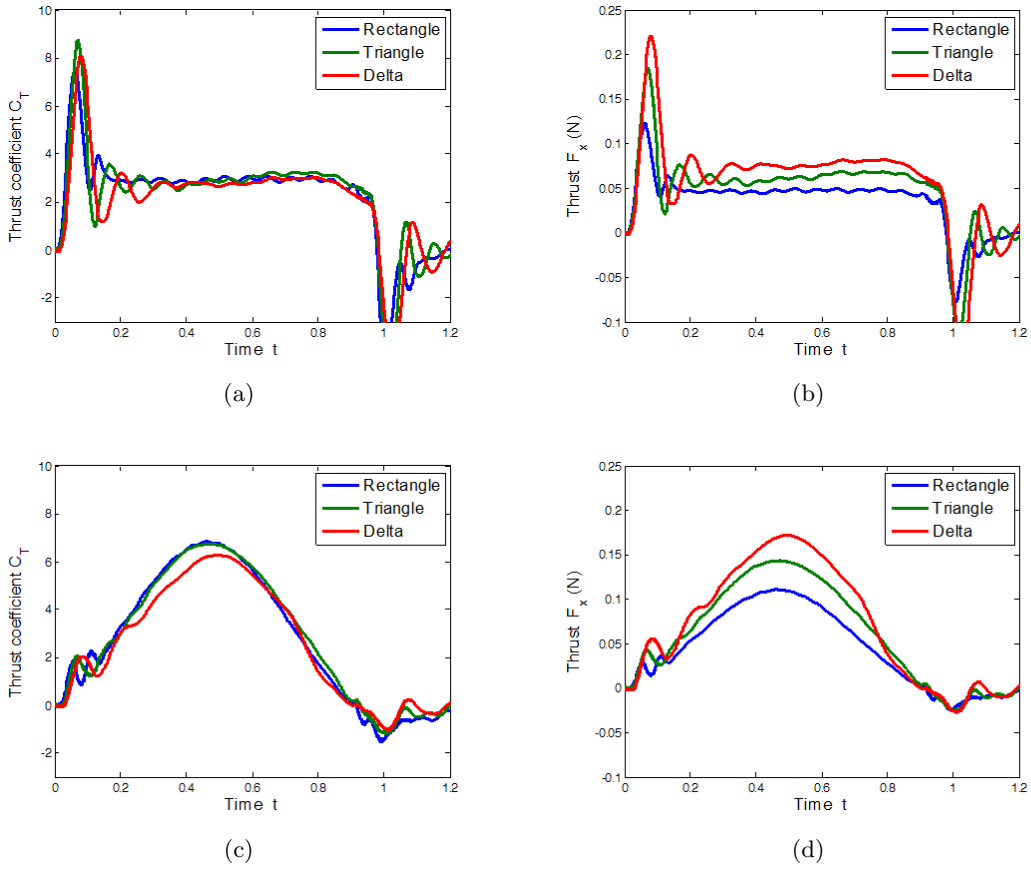

Figure 3.7: Shape effect on thrust generation for trapezoidal angular velocity ((a) and (b)) and sinusoidal angular velocity ((c) and (d)). The value of the y-axis is thrust coefficient for (a) and (c) and thrust for (b) and (d).

ing vorticity of the leading-edge vortex toward the tip (Ellington *et al.*, 1996). Meanwhile, in our model of drag-based propulsion, spanwise flow induces the outward motion of the tip vortex rather than maintaining the tip vortex near the tip edge, which is advantageous in thrust performance.

3.3.2 Reynolds number dependence of vortex structure and spanwise flow

In order to investigate whether or not the tip vortex motion and spanwise flow distribution is dependent on the Reynolds number, two Reynolds number cases (Re = 19720 and 140) are compared for the rigid delta-shaped plate case with the trapezoidal angular velocity program. In the low Re case, the tip vortex does not move outward during rotation as much as that of the high Re case (figure 3.8). Moreover, the core of the tip vortex does not show a clear separation from the tip edge. Instead, the core elongates following the tip edge. Spanwise flow is not formed as distinctly as in the high Re case. High shear stress due to high fluid viscosity keeps fluid behind the plate from moving toward the tip, the lower pressure region. Most of the flow behind the plate has the velocity component perpendicular to the span of the plate for the low Re case. All of these trends are also found for the sinusoidal velocity case.

It was examined how thrust and vortex structure are affected when some portion of spanwise flow near the propulsor is blocked. For this purpose, a thin plastic fence of width 4 cm and height 2 cm was attached perpendicularly to the back surface of the delta-shaped plate ($EI = 10.9$) at several positions (figure 3.9). In Re = 19720 (figure 3.9(a)), the effect of a fence on reducing thrust is significant during the second half of the stroke whereas it is not significant during the first half. In the case of $l = 2$ cm, thrust of the plate with a fence decreases about 30% near $t = 0.9$. The fence positioned nearer to the tip has a generally larger impact on thrust reduction, which implies that spanwise flow near the tip is critical in the interaction with the vortex structure near the tip and the reduction of thrust. The flow fields were compared for the plate ($EI = 10.9$) with and without a fence at $l = 2$ cm. Interestingly, in the second half of rotation, the circulation growth rate of the tip vortex structure is larger in the with-a-fence case (figure 3.10). However, in the with-a-fence case, some portion of the vortex sheet shed from the tip edge does not move outward, but rather accumulates near the tip, which results in the reduced inner area S_x of the vortex structure (figure 3.11). Thus, in spite of larger circulation, the with-a-fence case generates less force.

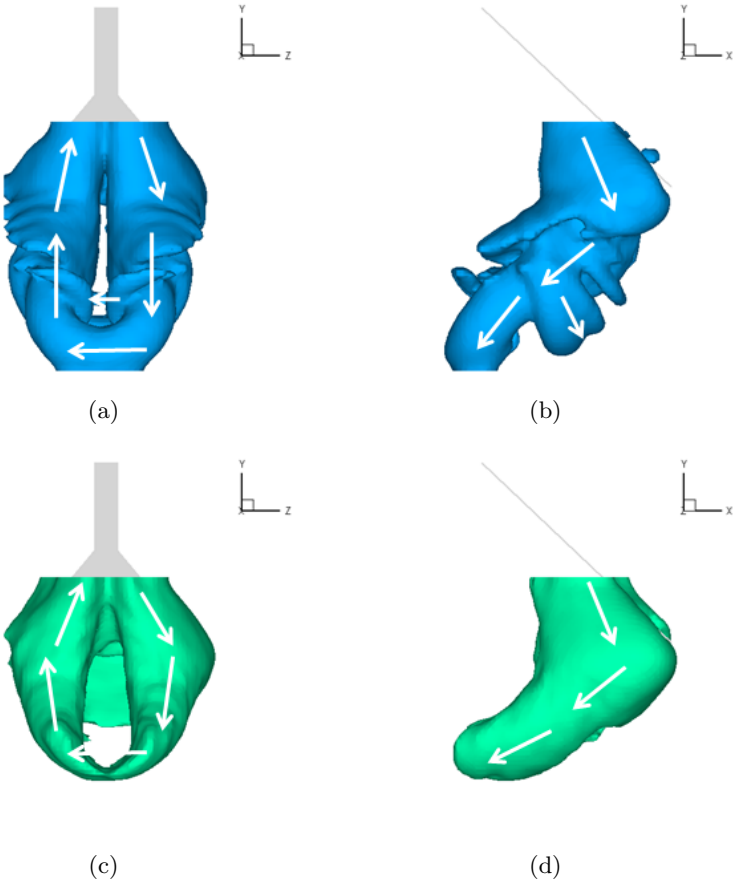

(a) (b)

(c) (d)

Figure 3.8: Comparison of vortex structures between high and low Reynolds numbers at t = 0.92 for the rigid delta-shaped plate and trapezoidal angular velocity case. (a) and (b): Re = 19720, (c) and (d): Re = 140. (a) and (c) are in back view, (b) and (d) are in side view. Iso-surfaces of vorticity magnitude ($|\boldsymbol{\omega}| = 6$ for high Re and $|\boldsymbol{\omega}| = 4$ for low Re) are used. The white arrows show the rotating direction of the vortex with the right-hand rule.

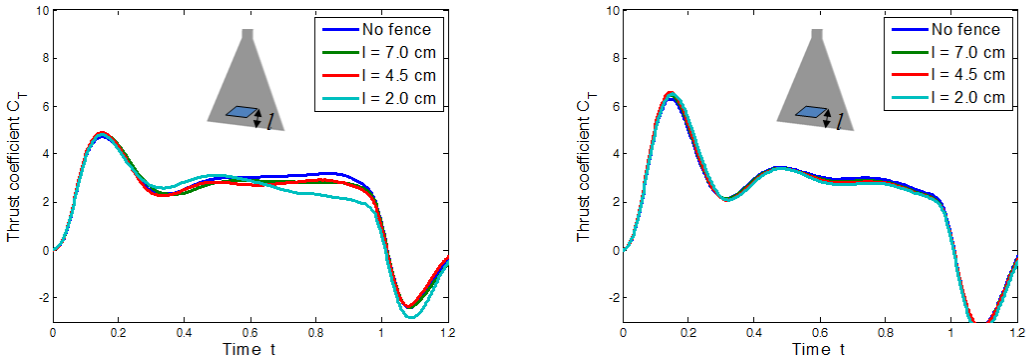

Figure 3.9: Fence effect of thrust in the delta-shaped plate ($EI = 10.9$) and trapezoidal velocity program case: (a) Re = 19720 and (b) Re = 140. l is the distance of the fence from the tip edge.

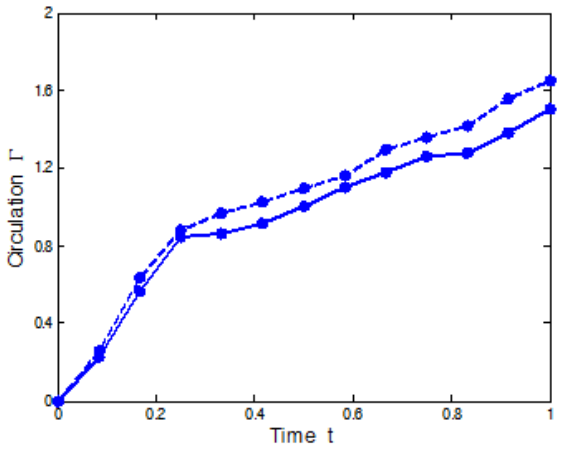

Figure 3.10: Comparison of tip vortex circulation between without-a-fence (continuous line) and with-a-fence (dashed line) cases.

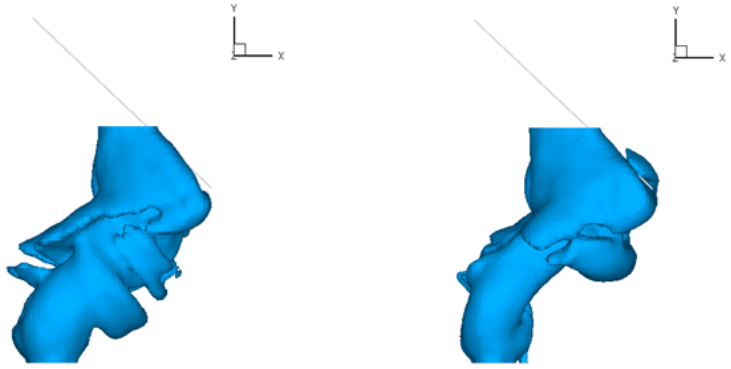

(a) (b)

Figure 3.11: Comparison of vortex structures between (a) without-a-fence and (b) with-a-fence cases at $t = 0.92$. The fence is positioned at $l = 2.0$ cm. The delta-shaped plate ($EI = 10.9$) and trapezoidal velocity program are used.

In the delta-shaped case of Re = 140, the tip vortex does not move outward as much as the Re = 19720 case and spanwise flow is not as strong. Therefore, the effect of spanwise flow blockage on thrust generation is negligible (figure 3.9(b)). A less distinct outward motion of the tip vortex does not mean that thrust is smaller in the low Re case than the high Re case. From our experiment, the low Re cases were found to generate more thrust. We conjecture that it is because side-edge vortices of the low Re case are distributed more outward in the y-direction, compared to those of the high Re case.

3.3.3 Change of thrust trend by flexible propulsors

In order to study the effect of plate flexibility on thrust generation, the force was measured with four triangular plates with different bending stiffness (rigid, $EI = 10.9$, 3.2, and 1.4) for the trapezoidal angular velocity (figure 3.12). If the plate is flexible, the plate is bent backward during impulsive angular acceleration of the plate. The peak of the hydrodynamic force during impulsive acceleration is smoothed out more distinctly as the bending stiffness is smaller. In spite of bending, the flexible plastic plates can generate more thrust than the rigid glass plate for some time after the angular acceleration phase. In addition to the acceleration phase, the peak in the deceleration phase also tends to be smoothed out for the low bending stiffness case. Even though the temporal trend of the force acting on the plate is affected by bending stiffness, total impulse I_∞ is not strongly dependent on it. All four cases have a similar magnitude of total impulse; I_∞ is between 2.10 and 2.15 for the four

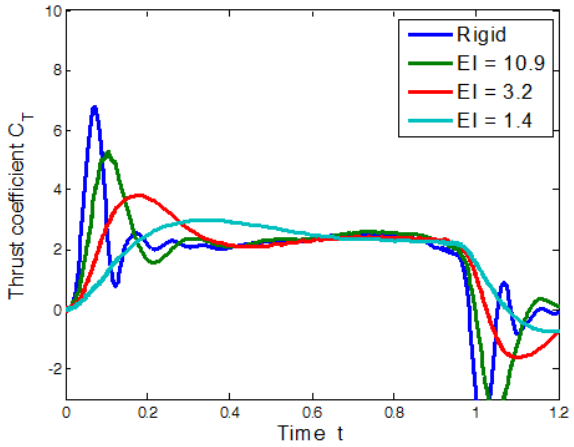

Figure 3.12: Flexibility effect on thrust generation for four triangular plates with different bending stiffness in the trapezoidal angular velocity program.

cases. This does not mean that the propulsor with smaller bending stiffness can generate the thrust comparable to the above four cases. In our experiment, the plate with $EI = 0.4$ generated a much smaller impulse than the above cases. The plate was bent backward so severely during rotation that the rotational speed of the plate was much smaller than the above cases. In the sinusoidal angular velocity program, the large initial peak of the force is absent even for the rigid plate case, and thus the temporal trend of the thrust is similar for the four bending stiffness cases.

The shapes of the rigid plate and flexible plate ($EI = 1.4$) during rotation are shown in figure 3.13(a). In figure 3.13(b), the rotating angles of the plates are plotted. For the flexible plate, the position of the tip edge relative to the initial position of the rigid plate was used to calculate the rotating angle. Because of the gravity, the initial positions of the rigid and flexible plates are not same. During initial acceleration, the rotating motion of the tip part of the flexible plate is delayed. The maximum angle difference between the rigid and flexible plates is 11° (at $t = 0.25$). Even after $t = 1$, the flexible plate continues to rotate and overshoots the final position of the rigid plate. After $t = 1.25$, the flexible plate returns toward the final position of the rigid plate. The flexible plate ($EI = 1.4$) can generate larger thrust than the rigid plate during the first half of the power stroke ($t = 0.2 \sim 0.5$ in figure 3.12). For the flexible plate, the bending caused by the hydrodynamic force acting on the plate delays the vortex formation process. However, after the acceleration phase, the vortex

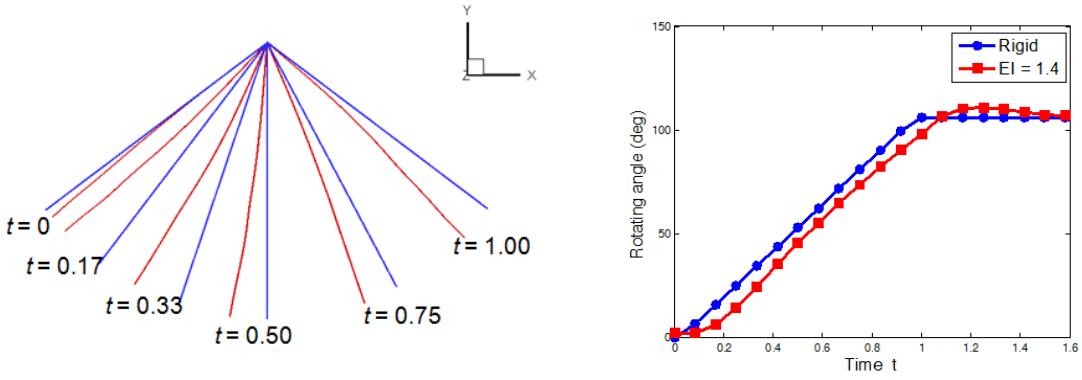

(a) (b)

Figure 3.13: (a) Plate shapes of the rigid plate (blue) and the flexible plate ($EI = 1.4$, red) during a power stroke in side view. (b) Rotating angle of the plates. The rotating angle was calculated from the initial position of the rigid plate. In both (a) and (b), the trapezoidal velocity program is used.

starts to develop at a fast pace. When the bending of the flexible plate is relaxed due to reduced hydrodynamic force, the tip of the plate moves faster than that of the rigid plate during the remaining first half of rotation (figure 3.13(a)). This action is closely related to the trend in the growth of the tip vortex circulation (figure 3.14). The tip vortex circulation of the flexible plate ($EI = 1.4$) delays its growth at an initial stage of rotation, but catches up circulation of the rigid glass plate in the middle of a stroke. For $t = 0.2 \sim 0.5$, the circulation slope of the flexible plate is larger than that of the rigid plate, which contributes larger thrust during that time according to Eq. 3.1.

Many studies about the mechanical effect of flexible flapping propulsors have focused on enhanced performance of propulsive force and efficiency by virtue of flexibility (Mountcastle & Daniel, 2009; Young *et al.*, 2009). In our cases of drag-based propulsion, flexible propulsors generate total impulse similar to that of the rigid propulsor. However, the trend of thrust generation is quite different between rigid and flexible propulsors in the trapezoidal angular velocity program. With smoothed peaks of thrust, the flexible propulsor could generate nearly constant thrust during a power stroke. Some advantages of flexibility can be inferred from this result. The unsteadiness of the thrust is reduced by flexibility in spite of sudden acceleration and deceleration without the sacrifice of total thrust performance, which is good at stabilizing the body during abrupt locomotion. Furthermore, by avoiding large peaks of the force acting on the propulsor, flapping animals will be able to reduce

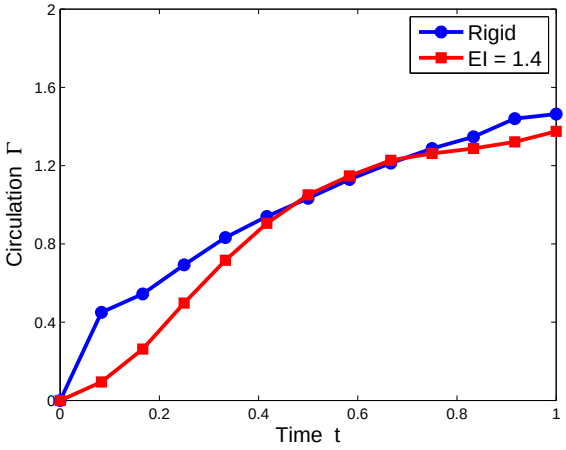

Figure 3.14: Circulation of the tip vortex for the rigid and flexible ($EI = 1.4$) cases. The trapezoidal velocity program is used.

the danger of fracture and fatigue in structures for propulsion. In the sinusoidal velocity program cases with flexible plates of the same bending stiffness, the effect of flexibility on changing a thrust trend was not noticeable because there was no impulsive rotational acceleration and deceleration.

3.3.4 Optimal stroke angle and vortex shedding

A simple experiment was conducted to find out if there was an optimal power stroke angle for efficient thrust generation. For rectangular, triangular, and delta-shaped rigid plates, the power stroke angle ϕ was varied from 60° to 180° with 10° increments. The sinusoidal angular velocity program is used in this experiment. The stroke time of the propulsor is proportional to the stroke angle; 2.4 sec for 180° and 1.2 sec for 90°. For all stroke angles, the mean angular velocity remains constant, which means the maximum angular velocity in the middle of a stroke also remains constant. Only one power stroke was considered, and, after the power stroke, the plate stayed at the final position of the power stroke without returning to its initial position. The starting and stopping positions of the plate are symmetric with respect to the yz-plane. In order to avoid the plate moving over the free surface for large stroke angle cases (e.g., 180°), in this experiment, the rotating axis of the stepper motor was parallel to the y-axis, and the shaft and the plate were immersed vertically into the tank.

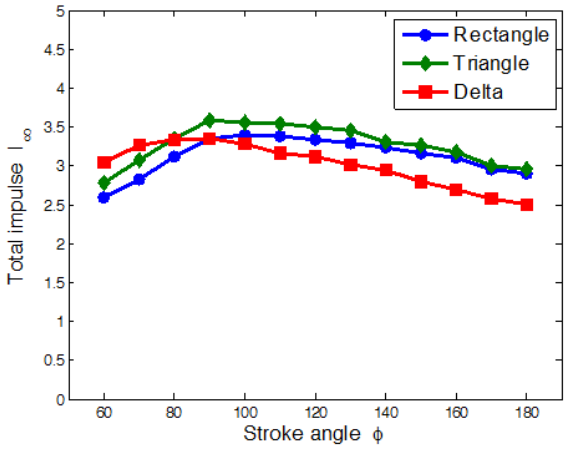

Figure 3.15: Stroke-angle dependence of total impulse for three cases with different shape.

For the stroke angles between 90° and 180°, non-dimensionalized total impulse has a tendency to increase slightly as the stroke angle decreased (figure 3.15). As the stroke angle decreases further from 90°, the total impulse tends to decline steeply except for the delta-shaped plate case. In all three cases, the stroke angle for the highest total impulse resides between $80 \sim 90°$. It is notable that the delta-shaped plate case has its highest total impulse below $\phi = 80°$ while it has the lowest total impulse above $\phi = 100°$. For the rectangular and delta-shaped propulsors, the time histories of the impulse I_x for five stroke angle cases are plotted in figure 3.16. In both cases, the lower stroke angle case has the higher peak just before the plate stops. However, for $\phi = 60°$, the impulse decreases significantly near $t = 1$, which results in reduced total impulse. The amount of impulse reduction near the stopping time is much larger for the rectangular plate than the delta-shaped plate.

If the blade element theory is applied to find the best stroke angle for thrust performance in our model, the lower stroke angle should produce the higher non-dimensional total impulse I_∞. According to the blade element theory, added-mass effect by acceleration is canceled by added-mass effect by deceleration in thrust generation because of the symmetry of the kinematics. As the stroke angle is small, the plate surface maintains a large angle relative to the thrust direction (x-direction) during most of the stroke time. Therefore, a smaller stroke angle is more efficient in generating quasi-steady force in the x-direction. For these reasons, if the blade element theory is applied, the stroke angle should be inversely related to non-dimensional total impulse. However, it contradicts our result shown in fig-

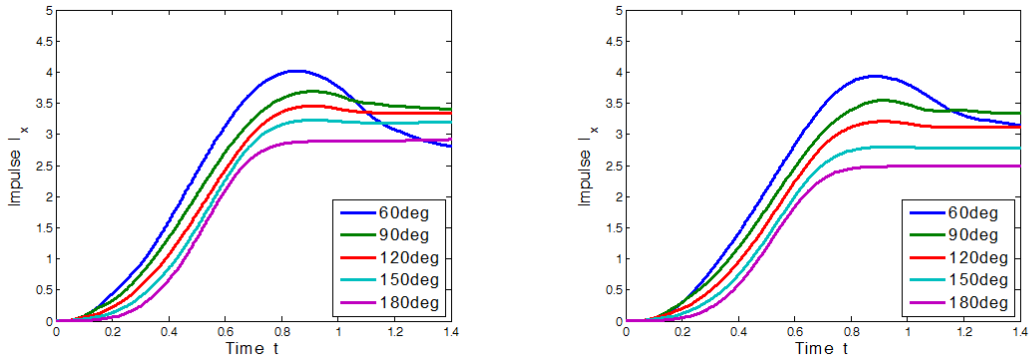

(a) (b)

Figure 3.16: Impulse for five stroke angles in (a) rectangular and (b) delta-shaped plate cases.

ures 3.15 and 3.16. In this sense, the application of the blade element theory to the study for drag-based propulsion is questionable.

Muskrats and ducklings employing a drag-based propulsion mode use a specific stroke angle for a given body speed (Fish, 1984; Algeldinger & Fish, 1995). Our experiment to find the optimal stroke angle was meant to find important factors that determine the preferred stroke angle. From repeated paddling motions of the propulsor, it has been indentified that the ring-like vortex structure is shed into the wake (Algeldinger & Fish, 1995; Drucker & Lauder, 1999). The closed vortex structure in the wake originates from a starting vortex (a tip vortex and side-edge vortices in our case) and a stopping vortex. When the propulsor decelerates its power strokes, the stopping vortex starts to shed from the plate. The shedding process continues even after the propulsor finishes its power stroke. How the stopping vortex is shed depends on the shape and flexibility of the plate and the angular velocity program. For example, the stopping vortex sheds smoothly for the sinusoidal velocity program while it sheds abruptly for the trapezoidal velocity program because of its short deceleration time.

The stopping vortex can be shed both from the tip edge and from the two side edges of the plate. In all edges, the stopping vortex has vorticity the sign of which is opposite that of the starting vortex. In our experiment, unless the stopping vortex sheds in the direction parallel to the x-axis, the shed stopping vortex has a negative effect on thrust ($-F_x$) according to Eq. 3.1. As the stroke angle becomes smaller, this negative effect of the stopping vortex on thrust is amplified since the stopping vortex tends to shed from the

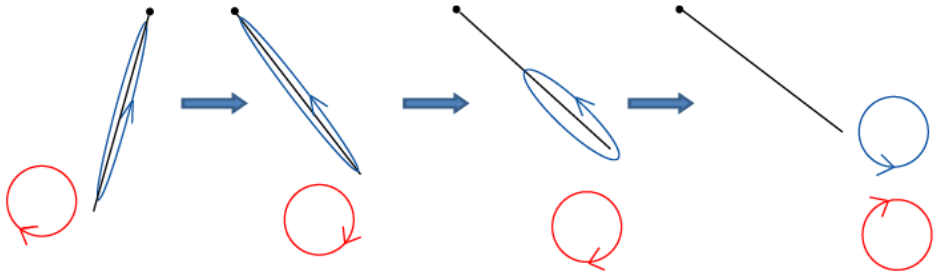

Figure 3.17: Formation and shedding of the tip vortex (red) and the corresponding bound vortex (blue) on the $z = 0$ plane. The shedding bound vortex forms the stopping vortex. Arrows indicate the rotating direction of vorticity (ω_z) on the $z = 0$ plane.

tip edge and side edges in the direction perpendicular to the x-axis. For this reason, total impulse decreases as the stroke angle reduces further from 90° in our experiment (figures 3.15 and 3.16). For clarity, the formation and shedding of the tip vortex and the corresponding bound vortex are illustrated in figure 3.17. During rotation, the bound vortex is created on the surface of the plate as the counterpart of the starting tip vortex. In deceleration, the bound vortex starts to move toward the tip edge and forms a stopping vortex. This shedding process has a negative effect on thrust generation since it reduces the inner area spanned by the vortex structure.

For the $\phi = 60°$ case of the delta-shaped plate, the decline of the impulse near $t = 1.0$ is small, compared to that of the rectangular plate (figure 3.16). One possible reason is the position of the bound vortex on the plate surface. In the delta-shaped plate case, the bound vortex is distributed mainly near the tip during the stroke. Meanwhile, the bound vortex is distributed uniformly from the base to the tip in the rectangular plate case. Thus, during the stopping vortex shedding process, the decrease of the inner area enclosed by the vortex structure ($\dot{S}_x < 0$) may be smaller than that of the rectangular plate case. Spanwise flow distribution can also be used to explain this trend. In the small stroke angle case, the flow behind the plate pushes the plate in the positive x-direction when the plate decelerates or stops and it causes the negative thrust. For the delta-shaped plate case, the flow behind the plate has a stronger spanwise component than the other cases with different shapes, which means less impact on the plate. Therefore, the undesirable effect of the flow behind the plate on thrust is smaller than the other cases.

3.4 Concluding remarks

Several characteristics of drag-based paddling propulsion are studied with a simple mechanical model and a measurement technique for mapping three-dimensional flow fields. In drag-based propulsion, the temporal change of the vortex strength is an important parameter in the relation between vortex formation and thrust generation. Our studies indicate that spanwise flow behind the paddling propulsor plays an important role in tip vortex development and thrust generation. The distribution of spanwise flow is dependent on the propulsor shape and the Reynolds number. A delta-shaped propulsor generates strong spanwise flow compared to a rectangular propulsor. For the low Reynolds number case, spanwise flow is not as strong as that of the high Reynolds number case. Without sacrificing total impulse, the flexible propulsor can smooth out thrust peaks during sudden stroke motions, which is favorable in avoiding structural failures. We also explored the role of stopping vortex shedding in efficient thrust generation by finding the relation between stroke angles and total impulses generated by paddling propulsors.

The motion of the mechanical model in our study is simple. A recovery stroke was not considered, and the body (the rotating axis of the model) was fixed. A more sophisticated model is required in order to investigate thrust performance under realistic kinematic conditions for paddling animals. Even though our model is simple, we expect that the main characteristics of vortex formation and thrust performance, which were studied here, should hold for more complex drag-based locomotion.

Chapter 4

Clapping propulsion

4.1 Background

Many animals use a pair of propulsors the motion of which is symmetrical along a sagittal plane. In some cases, the propulsors on both sides approach closely or come in contact with each other. The most well-known case is the Weis-Fogh clap and fling mechanism in the hovering of insects (Weis-Fogh, 1973; Ellington, 1984b). In this mechanism, a pair of wings clap and fling sequentially during pronation. Some insects such as locusts and butterflies were found to clap and fling their wings even during forward flight (Cooter & Baker, 1977; Brodsky, 1991). Several living creatures also make a pair of propulsors approach each other for locomotion in water. For example, frogs extend their legs toward the symmetrical plane when they move or jump quickly in water. A similar motion is also found when humans swim the breaststroke. The benefits of this locomotion mode have been suggested. The insect wings can generate large lift instantaneously when the wings fling after clapping, which has been regarded as an important unsteady lift enhancement mechanism for hovering in some species of insects (Weis-Fogh, 1973; Ellington, 1984c). Gal & Blake (1988) insisted that frogs might generate additional thrust by using a jetting mechanism. According to their study, when a pair of legs is close to each other during an extension phase, the momentum is imposed on the water by a jet between the two legs. Brodsky (1991) also suggested that the butterflies flying forward used the jetting mechanism for thrust generation during pronation phases. Furthermore, the drag acting on a pair of propulsors can be reduced if the frontal area of the propulsors normal to the moving direction is reduced by clapping or straightening up the propulsors backward.

In addition to the relation between kinematics and propulsive force production, vortex

formation has been studied for a pair of propulsors contacting or approaching each other. In the case of hovering insects, large leading-edge vortices were observed on the upper surfaces of the wings at the fling motion of the wings (Spedding & Maxworthy, 1986; Miller & Peskin, 2005). These vortices remain stably near the wings during a downstroke (Maxworthy, 1979). Using smoke visualization, Brodsky (1991) showed that a vortex ring was generated when butterfly wings clapped after an upstroke and was coupled with another vortex ring created during a downstroke. Using planar particle image velocimetry, Johansson & Lauder (2004) and Stamhuis & Nauwelaerts (2005) showed that vortices were shed at each leg of a frog when the frog kicked its legs; these vortices remained separated from each other. However, in this kind of study on vortex formation, it was difficult to investigate the complicated three-dimensional nature of the vortex formation process in detail because of the limitation of the velocity field mapping technique. If a pair of propulsors approaches each other closely, the vortices generated by them interact with each other and develop a complicated configuration of the vortex in the wake. This process is unsteady and three-dimensional. Therefore, its understanding requires the analysis of three-dimensional flow fields.

The interaction of multiple vortices has been one of the main topics addressed in the study of vortex dynamics. The collision of two vortex rings would be the topic relevant to the vortex formation by the locomotion modes mentioned above. When two thin circular vortex rings with a large radius collide obliquely, they suffer a drastic change in shape. They may merge into one vortex ring or split into another two-vortex system. The morphology of two vortex rings after collision depends on initial conditions such as the angle between approaching vortex rings and the Reynolds number. For details on the collision of two vortex rings, see Kida *et al.* (1991) and references therein. Even though these studies on the interaction of multiple vortices are closely related to this study, there are fundamental differences. In most previous studies, the interaction between vortex rings is free from the influence of a solid structure generating those vortices. However, in our study, the interaction of two vortex structures is severely affected by the plates; the bound vortex on the plate plays an important role in this interaction. Moreover, the shape of interacting vortices is not exactly a circular ring.

Here, we study how the vortex structure created by a pair of propulsors evolves in space and time. By changing geometrical and kinematic conditions of the model such as aspect ratio and stroke angle, it was investigated how such conditions affect thrust generation

and vortex evolution in the wake. Specifically, we focus on the circulation and shape of the vortex in order to find the relation between the impulse acting on the model and the vortex structure under various conditions. Single-plate cases were also considered by removing one of the plates from the two clapping plates. It was intended to find whether there is an advantage of double clapping plates over a single plate for thrust generation and, if any, how the aspect ratio of the plate is related to this advantage. Moreover, we study the non-dimensional time parameter, vortex formation time, to characterize the efficiency of force generation. Vortex formation time has been studied in order to find out the relation between efficient thrust generation, vortex formation, and kinematic and geometric conditions of vortex generating models (Gharib *et al.*, 1998; Krueger & Gharib, 2003; Dabiri & Gharib, 2005a; Milano & Gharib, 2005; Ringuette *et al.*, 2007, e.g,). It was suggested as an important principle for the performance of biological propulsion systems. For review, see Dabiri (2009). Here, the concept of the vortex formation time is applied to determine whether the vortex structures, which are generated by the single-plate and double-plates models, are optimized for efficient thrust generation.

We implemented defocusing digital particle image velocimetry (DDPIV) (Willert & Gharib, 1992; Pereira & Gharib, 2002) to map the three-dimensional flow fields generated by the mechanical clapping model. Force measurement was conducted as well to obtain thrust and impulse. To simulate a clapping motion, two thin plastic plates were rotated symmetrically. From now on, the term *clap* will be used broadly to describe the motion of double plates rotating toward each other, even though there is a gap between the two plates.

This chapter is organized as follows. The experimental setup and the data analysis method are explained in §4.2. In §4.3.1, the wake structure formed by the clapping motion of two plates is compared with the wake structure by the rotation of only a single plate for the purpose of showing the fundamental difference in a vortex shedding process. In §4.3.2, the vortex reconnection mechanism found in clapping cases is explained in more detail. The effect of aspect ratios of the plates on thrust performance and vortex formation is presented in §4.3.3. It is shown in §4.3.4 how the fate of shedding bound vortices depends on the angle between a pair of plates when rotation stops. The vortex formation time and its relation with impulse generation were explored in §4.3.5. Lastly, results are summarized in §4.4.

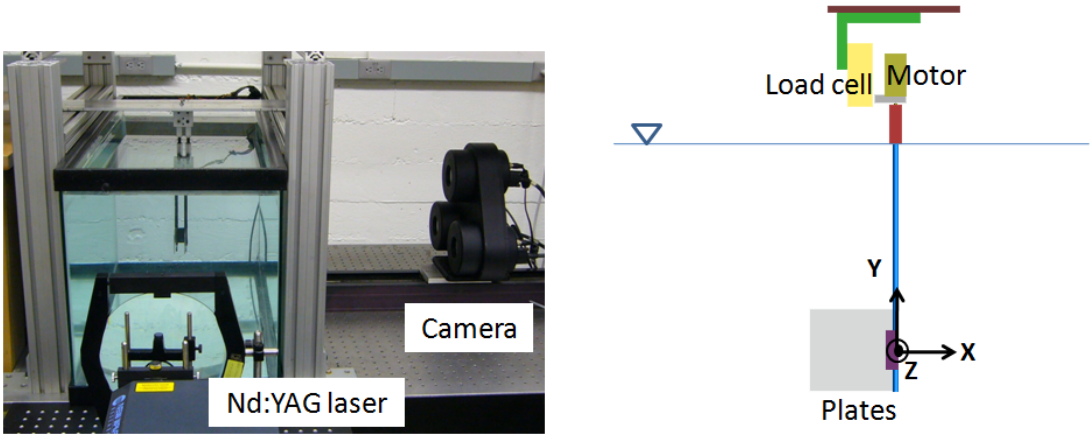

(a) (b)

Figure 4.1: (a) Experimental setup and (b) details of the model from the camera view.

4.2 Experimental setup

Figure 4.1 shows the experimental setup and the mechanical model. A glass tank of 870 $\times$ 430 $\times$ 360 mm^3 was filled with water. A pair of stepper motors (NEMA 8, Anaheim Automation Inc.) was linked to a fixed aluminum plate via a load cell. Micro-stepping drivers (IM483, Schneider Electric Motion) were used for precise and smooth rotation of the motors. Two stepper motors were put together, and each motor was connected to a vertical aluminum shaft. The gap distance between the two aluminum shafts was 2 cm. Plastic tape was used to block the gap between the two plates. Rectangular acrylic plates of uniform thickness 1.46 mm were used as propulsors. The plates were attached to the end of the shafts. The width of the plates (span s) was 8 cm, and the heights of the plates (chords c) were 4 cm, 8 cm, and 12 cm for three different aspect ratios (AR = 2, 1 and 0.66). In this study, the aspect ratio was defined as s/c.

The plates rotated along the rotating axis parallel to the y-axis from an initial angle θ_i to a final angle θ_f with a sinusoidal angular velocity program for a given stroke angle ϕ $(= \theta_i - \theta_f)$ (figure 4.2(a)). Only one power stroke was considered in this study. Two stroke angles, $\phi = 45°$ and $90°$, were chosen for flow visualization. The maximum and mean angular velocities were the same for both $\phi = 45°$ and $90°$ cases. The difference between the two stroke angle cases was the rotating time T; 0.6 sec for $\phi = 45°$ cases and 1.2 sec for

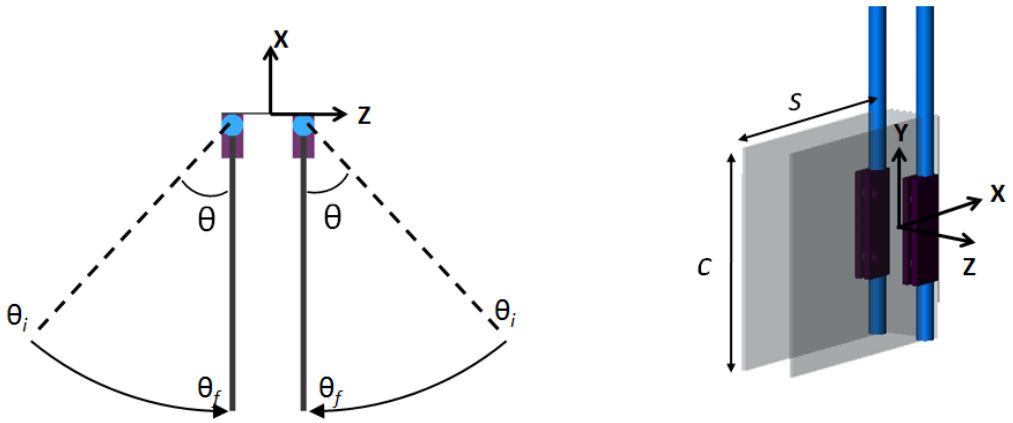

(a) (b)

Figure 4.2: (a) Notations for angles. θ is the angle of the plate with respect to the $z = 0$ plane. θ_i is the initial angle before rotation, and θ_f is the final angle when rotation stops. A stroke angle ϕ is $\theta_i - \theta_f$ with arrows indicating the rotating direction of plates. (b) Coordinate system and definitions of chord c and span s. The clapping double-plates model was used in these subfigures.

Aspect ratio AR	2, 1, and 0.66
Plate material	Acrylic (thickness 1.46 mm)
Reynolds number Re	8400
Angular velocity program	Sinusoid
Stroke angle ϕ	$45° \sim 180°$ for force measurement $45°$ and $90°$ for visualization
Stroke time T	0.6 sec for $\phi = 45°$ 1.2 sec for $\phi = 90°$

Table 4.1: Summary of the model conditions considered in this study.

$\phi = 90°$ cases. During rotation of the plates ($0 \leq t \leq T$),

$$\theta(t) = \frac{\phi}{2}(1 + \cos(\frac{\pi t}{T})) + \theta_f, \tag{4.1}$$

and, after $t = T$, the plate remained static at $\theta = \theta_f$. The Reynolds number based on the mean speed of the tip U and the span s was 8400. The origin of the coordinate system used in this study is between two shafts and in the middle height of the plates. The x-axis is parallel to the tank wall, the y-axis is parallel to the aluminum shafts, and the z-axis is toward the camera (figure 4.2(b)). The model conditions are summarized in table 4.1.

A DDPIV system was employed to map three-dimensional flow fields. A DDPIV system composed of three CCD cameras was placed in front of the tank. The distance between the camera and the tank was adjusted to place the camera probe volume in the middle of the tank. The tank was seeded with silver-coated glass spheres of mean diameter 100 μm (Conduct-o-fil, Potters Industries Inc.). An Nd:YAG laser (200 mJ/pulse, Gemini PIV, New Wave Research Inc.) was placed to the left side of the camera, and plano-concave lenses were used to make a laser cone that covered the camera probe volume. The control computer sent trigger pulses to synchronize operation of the DDPIV camera and the laser, and control the motor motion. The time gap between two laser pulses was 25 msec to take a pair of images in a double exposure mode.

The images taken from the DDPIV camera were processed with the software based on Pereira & Gharib (2002) and Pereira *et al.* (2006). First, three-dimensional coordinates of the particles inside the tank were found by matching particle images of three cameras. From this information, velocity vectors of particles were calculated by a relaxation method of three-dimensional particle tracking (Pereira *et al.*, 2006). The camera probe volume was not large enough to include the vortex structure moving downstream in the wake. Thus, two sets of the experiment were performed by translating 120 mm from the initial position of the model in the x-direction. The velocity vectors of two sets with different model positions were combined. The total fluid domain mapped from two sets was $280 \times 160 \times 160$ mm^3. To increase the density of randomly-spaced velocity vectors in a fluid domain, the experiment was repeated 25 times under the same conditions with an interval of 90 sec. For each time frame, the velocity vectors from 25 cases were collected and fitted into grids of $3 \times 3 \times 3$ mm^3 to obtain a velocity field. After removing outlier vectors and applying a smoothing operator to the velocity field, the vorticity was obtained by a central difference scheme. For smooth rendering of iso-surfaces of vorticity magnitude, vorticity data were smoothed.

For impulse measurement, a load cell (miniature beam type, Interface Inc.) was attached to the motor. The stroke angle was varied from $\phi = 45°$ to $\phi = 180°$ with a 15° step. The rotational kinematics of the plate followed Eq. 4.1, and T was proportional to ϕ; 2.4 sec for $\phi = 180°$ and 0.6 sec for $\phi = 45°$. The signal was amplified and low-pass filtered with 5 Hz cutoff frequency through a signal conditioner (SGA, Interface Inc.). A thrust coefficient

C_T and a non-dimensional total impulse I_∞ was obtained as follows:

$$C_T(t) = \frac{F_x(t)}{\frac{1}{2}\rho U^2 \hat{r}_2^2 S} \quad \text{and} \quad I_\infty = \frac{\int_0^\infty C_T(\tau)\mathrm{d}\tau}{T}, \tag{4.2}$$

where F_x is the force acting on the model in the x-direction, U is the mean tip velocity of the plate during rotation, $\hat{r}_2^2$ is the non-dimensional second moment of plate area with respect to the rotating axis, and S is the area of the plate. S of double-plate clapping cases is twice as big as that of single-plate cases. I_∞ is different from $\overline{C_T}$, the mean of C_T during rotating time, in that I_∞ is integrated over infinite time. Even though the difference between magnitudes of I_∞ and $\overline{C_T}$ is small in our cases, I_∞ is the more proper dimensionless parameter to represent the total impulse acting on the model or the total hydrodynamic impulse imposed on fluid as reaction. Practically, due to the hysteresis problem of the load cell after the model stopped rotating, the force was integrated from $\tau = 0$ to $\tau = T + 0.4$ sec in order to obtain the total impulse I_∞.

Time, coordinate, velocity and vorticity were also non-dimensionalized;

$$t = t_d U/s, \quad \boldsymbol{x} = \boldsymbol{x}_d/s, \quad \boldsymbol{u} = \boldsymbol{u}_d/U, \quad \boldsymbol{\omega} = \boldsymbol{\omega}_d s/U. \tag{4.3}$$

Note that U and s are the same for all cases. In this study, $t = 0$ was set for the time when the plate stopped. It means the plate rotated during the negative t. This setting is used because the time spent for plate rotation depends on the stroke angle ϕ. Thus, it is better to set the stop time as $t = 0$ for easy comparison of vortex formation trends between different stroke angle cases ($\phi = 45^\circ$ and 90°) after the same time passes from the stopping time.

The non-dimensional circulation Γ and position of the vortex center d_x at some sections were calculated from the vorticity data. They were defined as

$$\Gamma = \int |\boldsymbol{\omega} \cdot \boldsymbol{n}| \mathrm{d}A, \quad d_x = \frac{\int |\boldsymbol{\omega} \cdot \boldsymbol{n}||x| \mathrm{d}A}{\Gamma}. \tag{4.4}$$

For $|\boldsymbol{\omega} \cdot \boldsymbol{n}|$ and section A, specific vorticity component and fluid domain were considered. On the xz-sections normal to the y-axis, the positive ω_y on the whole positive z-domain was used. On the xy-sections normal to the z-axis, the positive ω_z on the whole negative y-domain was used. In the above equations, the threshold value for ω_y and ω_z was 0.35; ω_y

and ω_z less than 0.35 were discarded.

4.3 Results and Discussion

Some terms that are frequently used in the following sections need to be clarified first. While the plate rotates, *a (starting) tip vortex* and *side-edge vortices* develop at the vertical tip edge, and the upper and lower horizontal side edges of the plate, respectively. A *bound vortex* is the collection of vorticity close to the surface of the plate as the counterpart of the starting tip vortex. The bound vortex and the starting tip vortex have ω_y components of opposite signs. The bound vortex includes the vorticity inside the rotating plate, which is twice as much as the angular velocity of the plate. The boundary layer of the plate is a major part of the bound vortex. A *vortex loop* means the closed loop of the vortex structure in the wake, translating in the negative x-direction, *downstream*. The vortex loop mainly consists of lateral parts, whose main vorticity component is ω_y, and longitudinal parts, whose main vorticity component is ω_z.

Through §4.3, in figures representing the vortex structure, iso-surfaces of vorticity magnitude were used. In these figures, the color contour on the iso-surface of $|\boldsymbol{\omega}|$ indicates the distribution of ω_y on the iso-surface in order to show clearly the rotating direction of tip and bound vortices. The only exception is figure 4.11.

4.3.1 Comparison of single-plate and double-plate clapping cases

4.3.1.1 Wake dynamics of single-plate cases

The vortex dynamics in the wake of single-plate cases is shown in figure 4.3 for the AR = 1 and $\phi = 45°$ ($\theta_i = 45°$, $\theta_f = 0°$) case and figure 4.4 for the AR = 1 and $\phi = 90°$ ($\theta_i = 90°$, $\theta_f = 0°$) case. For single-plate cases, a plate in the negative z was removed and only the plate in the positive z was considered. As the plate stops its rotation, the stopping tip vortex (blue region in figures) is shed from the plate and forms a vortex loop with the starting tip vortex (red region in figures). The stopping tip vortex is rolled up from the bound vortex on the surface and has the negative ω_y opposite to that of the starting tip vortex. Thus, through the interaction of counter-rotating parts of the vortex loop, the vortex loop translates away from the plate. Side-edge vortices and a portion of the bound vortex are also shed in the vertical direction from the plate. However, since the strength (circulation)

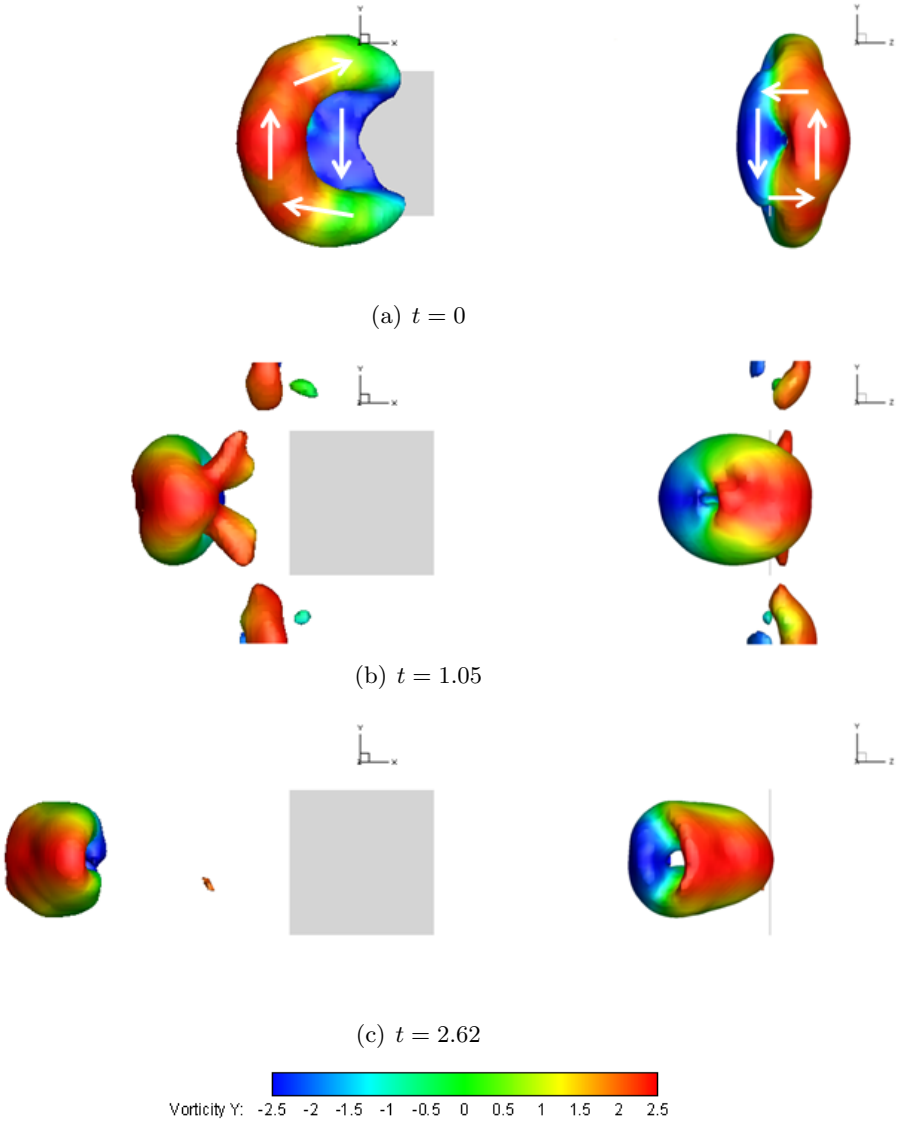

(a) $t = 0$

(b) $t = 1.05$

(c) $t = 2.62$

Figure 4.3: Vortex dynamics in the wake for the AR = 1 and $\phi = 45°$ case of single plate. The view of the left column is from $+z$, and the view of the right column is from $-x$. Iso-surfaces of $|\boldsymbol{\omega}| = 2.5$ are used. A contour of ω_y is colored on the iso-surface. The white arrows show the rotating direction of the vortex with the right-hand rule.

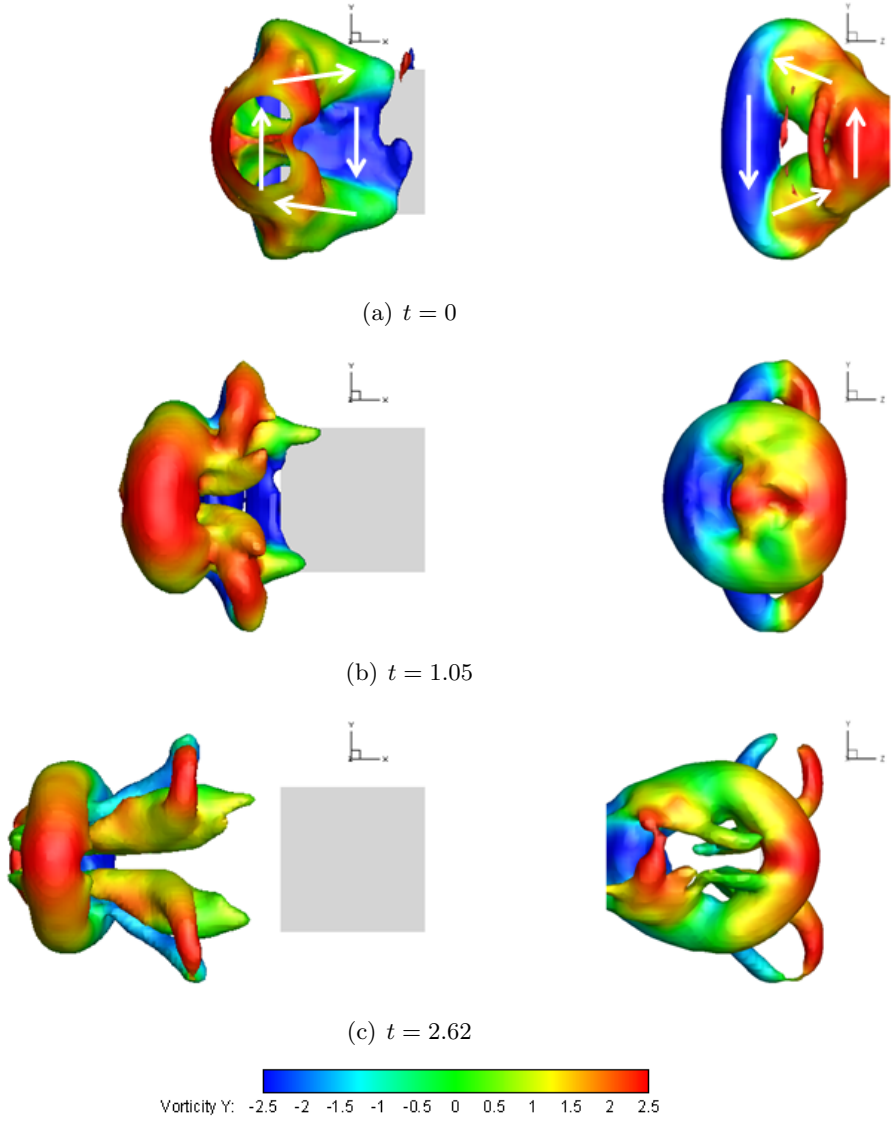

(a) $t = 0$

(b) $t = 1.05$

(c) $t = 2.62$

Figure 4.4: Vortex dynamics in the wake for the AR = 1 and $\phi = 90°$ case of single plate. The view of the left column is from $+z$, and the view of the right column is from $-x$. Iso-surfaces of $|\boldsymbol{\omega}| = 2.5$ are used. A contour of ω_y is colored on the iso-surface. The white arrows show the rotating direction of the vortex with the right-hand rule.

of the tip vortex is stronger than that of side-edge vortices, the vortex loop composed of the starting and stopping tip vortices is more dominant in its size and magnitude. The direction of the vortex loop moving in the wake is not parallel to the x-axis and rather tilted in the negative z-direction. The inertia of the starting tip vortex by the rotating plate causes the vortex loop to move off the x-axis even after the plate stops.

There are some important differences in the evolution of vortices between the stroke angle 45° and 90° cases. One notable difference is the deformation extent of the starting tip vortex before the plate stops as shown in figures 4.3(a) and 4.4(a). In the 90° case, while the plate rotates, the central part of the starting tip vortex separates distinctly from the tip edge and does not follow the edge of the plate. The tip vortex curves with its central part away from the plate. Therefore, in the 90° case, the vortex loop has the larger frontal area, projected onto the yz-plane, than the 45° case. In the 45° case, even though the core of the starting tip vortex is circular before the plate stops, it becomes elongated due to self-induction. However, for the 90° case, the effect of self-induction on the vortex core deformation is less obvious since the area of the vortex loop is larger.

4.3.1.2 Wake dynamics of double-plate clapping cases

Figures 4.5 and 4.6 show the dynamics of wake structures for double-plate clapping cases of $\phi = 45°$ ($\theta_i = 45°$, $\theta_f = 0°$) and $\phi = 90°$ ($\theta_i = 90°$, $\theta_f = 0°$). The aspect ratio of the plates is 1. At $t = 0$, the shape of the tip vortex in each plate does not look different from that of the single-plate case. However, the strength of the tip vortex at $t = 0$ is higher in the double-plate cases. Moreover, the total impulse acting on the model (I_∞) has the higher magnitude per plate when the plates work together. I_∞ of the $\phi = 45°$ cases is 3.30 for the single-plate case and 4.06 for the double-plate case. I_∞ of the $\phi = 90°$ cases is 4.42 for the single-plate case and 4.80 for the double-plate case. More results on circulation and impulse are presented in §4.3.3.

In the 45° case, soon after the plates stop, the tip vortices in both plates connect near the upper and lower corners of the plate and form one vortex loop. The strength of the vortex loop at the connected area becomes stronger from the time the connection begins (figure 4.7(a)). Because of the tip vortices, which tend to move toward the $z = 0$ plane, the vortex loop compresses horizontally and, consequently, elongates vertically for a while. The vortex loop looks elliptical with the major axis along the y-axis and the minor axis

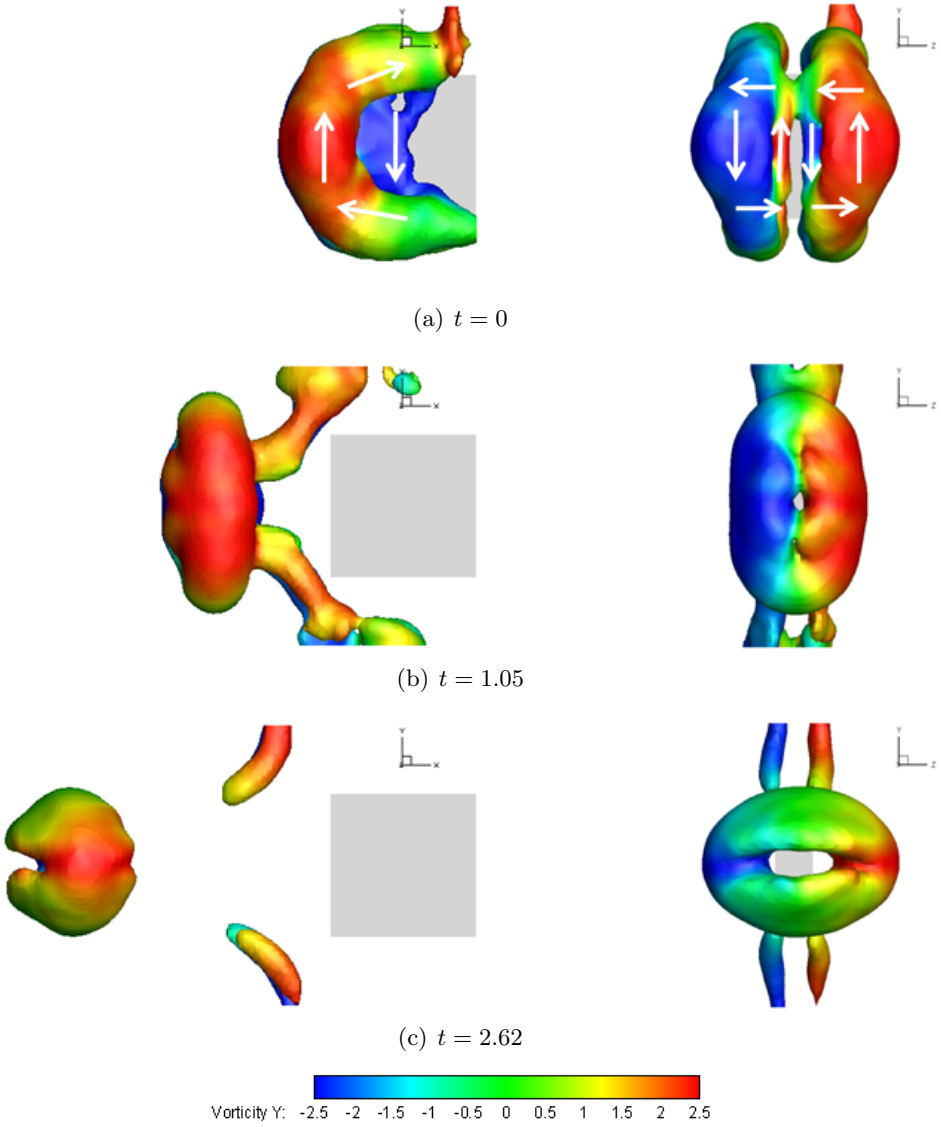

(a) $t = 0$

(b) $t = 1.05$

(c) $t = 2.62$

Figure 4.5: Vortex dynamics in the wake for the AR $= 1$ and $\phi = 45°$ case of double plates. The view of the left column is from $+z$, and the view of the right column is from $-x$. Iso-surfaces of $|\boldsymbol{\omega}| = 2.5$ are used. A contour of ω_y is colored on the iso-surface. The white arrows show the rotating direction of the vortex with the right-hand rule.

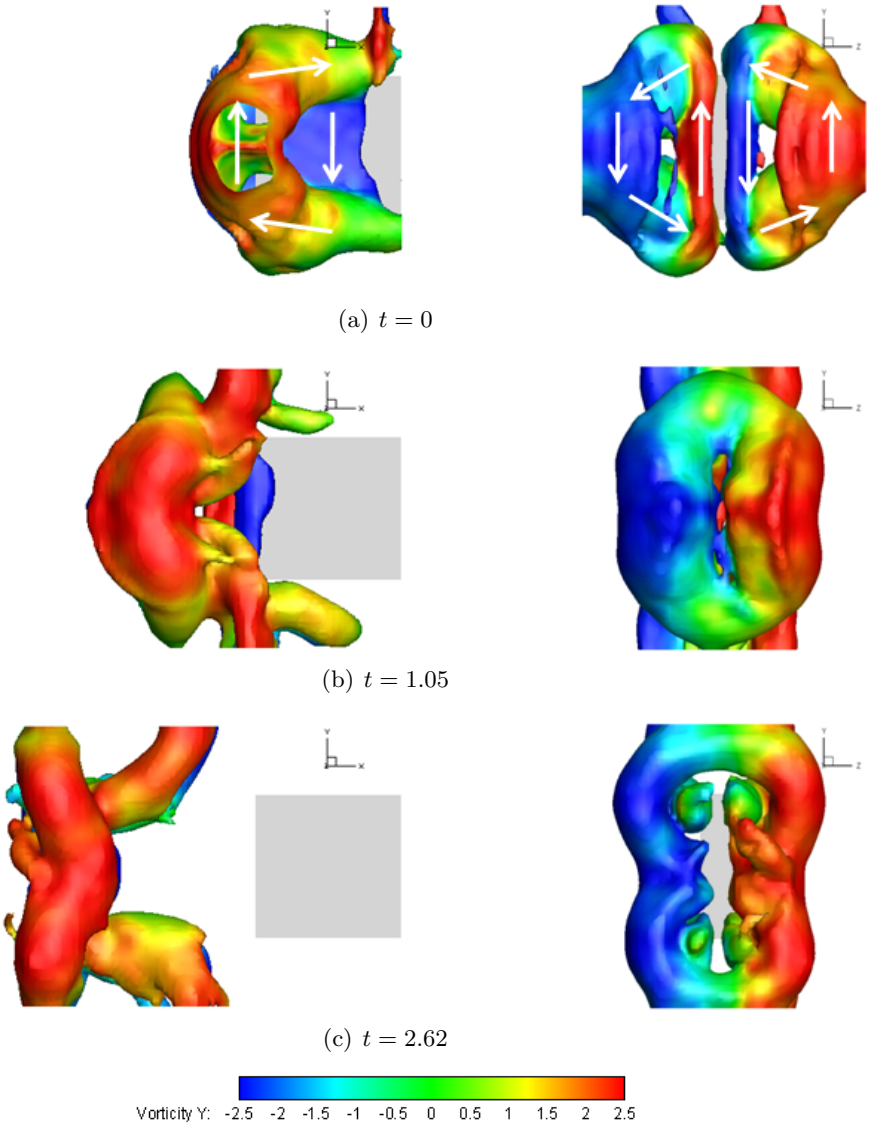

(a) $t = 0$

(b) $t = 1.05$

(c) $t = 2.62$

Figure 4.6: Vortex dynamics in the wake for the AR = 1 and $\phi = 90°$ case of double plates. The view of the left column is from $+z$, and the view of the right column is from $-x$. Iso-surfaces of $|\boldsymbol{\omega}| = 2.5$ are used. A contour of ω_y is colored on the iso-surface. The white arrows show the rotating direction of the vortex with the right-hand rule.

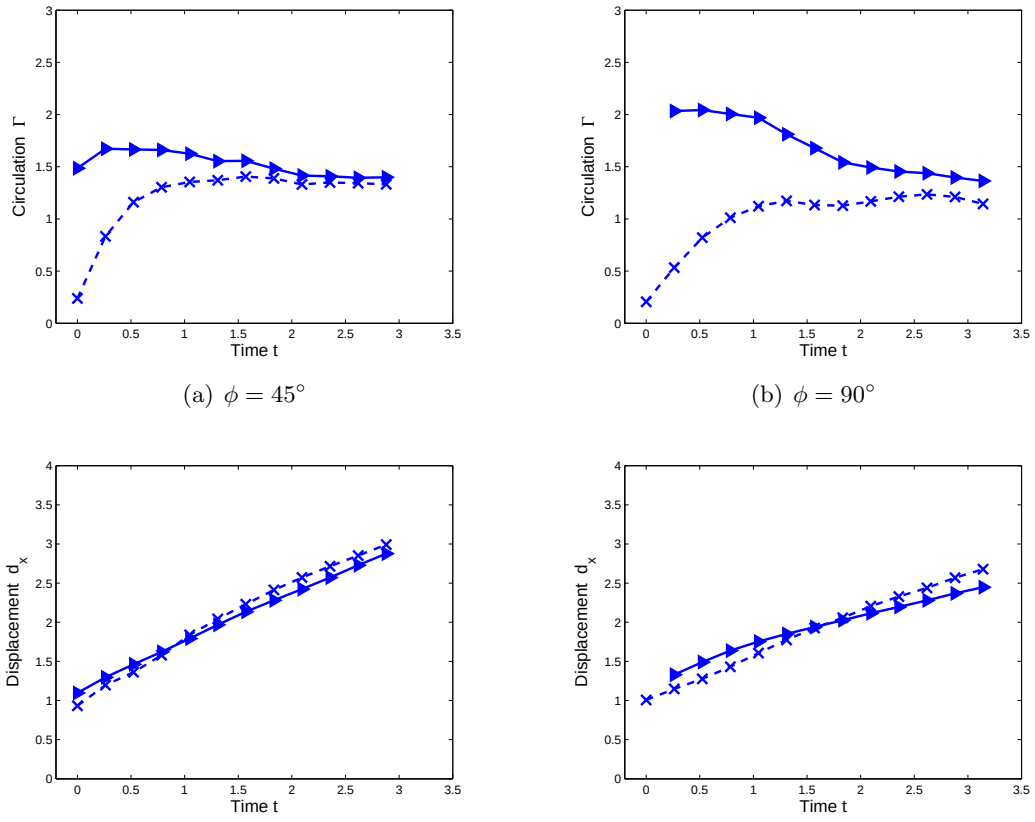

(a) $\phi = 45°$ (b) $\phi = 90°$

(c) $\phi = 45°$ (d) $\phi = 90°$

Figure 4.7: Circulation Γ ((a) and (b)) and x-directional displacement d_x ((c) and (d)) of the vortex structure after the plates stop for the AR = 1 case of double plates. Γ and d_x are taken both on a section of $y = 0$ and $z > 0$ ($\blacktriangleright$) and on a section of $z = 0$ and $y < 0$ ($\times$). Γ and d_x values are discarded when some part of the vortex is out of the measured flow field on the section.

along the z-axis (figure 4.5(b)). Since the upper and lower longitudinal parts of the vortex loop have high curvatures, the propagation speed of the longitudinal parts of the vortex loop begin to exceed that of the lateral parts (figure 4.7(c)). When the vortex loop travels downstream, it changes its major and minor axes. As the vortex loop moves downstream farther beyond $t = 2.62$, it is expected that the vortex loop changes its axes again. From the experiment, it was found that the vortex loop became circular at $t = 5.76$ possibly as a halfway process to change the axes again. Moreover, the core of the vortex loop loses its strength due to diffusion and vorticity cancelation by the part on the opposite side. Thus, its downstream speed decreases gradually.

The morpho-dynamics of the vortex loop in the 90° case is quite different from that of the 45° case. Similarly to the single-plate case, the central region of the tip vortex separates away from the tip edge when the plate rotates (figure 4.6(a)). After the tip vortices start to connect in the upper and lower corners of the plates, the vortex loop compresses laterally and elongates vertically. The lateral parts of the vortex loop near the $y = 0$ plane move toward the $z = 0$ plane more than other lateral parts (figure 4.6(c)). While the lateral parts of the vortex loop straighten up by compression, their propagation speed becomes smaller than that of the longitudinal parts with a higher curvature. Thus, the longitudinal parts of the vortex loop move faster downstream than the lateral parts (figures 4.6(c) and 4.7(d)). Unlike the 45° case, the interchange of major and minor axes in the vortex loop does not occur within the observed time. In the 90° case, the area enclosed by the vortex loop is larger than that of the 45° case, which means the ratio of the vortex loop area to the core size is larger. Thus, despite the higher strength of the vortex loop, the downstream propagation speed of the vortex loop in the 90° case is not as fast as that of the 45° case (figure 4.7).

The evolution of side-edge vortices is not independent of that of tip vortices. The vortices shed from side edges are still connected with the vortex loop when the vortex loop moves downstream. Since the upper and lower side-edge vortices tend to move in the positive and negative y-directions respectively, they have to be curved and stretched by interaction with the vortex loop moving in the negative x-direction. Because of stretching, the side-edge vortices should thin and have higher vorticity. Thus, these side-edge vortices should have been shown in figures 4.5 and 4.6. However, high vorticity of the thinned vortices was not captured in the experiment, which results in the disconnection between the vortex loop and

the side-edge vortices in the above figures. In the 90° case, because of the large inner area of the vortex loop, it is clearly seen that the side-edge vortices near the vortex loop are entrained inside the loop (figure 4.6(c)). Since the side-edge vortices are connected with the vortex loop, the circulation of the vortex loop cannot be constant along the loop as exemplified in figure 4.7.

4.3.2 Vortex reconnection mechanism in clapping

When two anti-parallel vortex tubes of similar strength collide in viscous flow, they merge in a finite contact zone and cancel the vorticity of the vortex tube in the opposite side. Bridges, vortex tubes perpendicular to the original vortex tubes, form near both ends of the contact zone and connect the two anti-parallel vortex tubes. This complicated vortex dynamics is known as the vortex reconnection mechanism (Melander & Hussain, 1990; Kida & Takaoka, 1994). The vortex reconnection mechanism has been studied extensively since the study on instability of counter-rotating vortices shed from the tip of the airplane (Crow, 1970). However, most studies on the interaction of two vortex rings have been conducted either computationally with the predefined vorticity distribution (e.g., Kida & Takaoka, 1987; Melander & Hussain, 1990; Kida *et al.*, 1991), or experimentally with vortex ring generators (e.g., Fohl & Turner, 1975; Oshima & Asaka, 1977). In the above section, it was shown that the vortex reconnection was also found when double plates clapped and it was an important process of developing one vortex loop in the wake.

Figures 4.8 and 4.9 show the time-series of the vortex reconnection process with a finer time step than that of figures 4.5 and 4.6. The plates rotated four times as slow as the §4.3.1 cases. The gap between laser pulses for a pair of images was 50 msec. Even though the Reynolds number is four times smaller than the §4.3.1 cases, the shape and strength of the vortex structure remain similar. Regions A−C of figure 4.10 are the regions where the new vortex tubes with the z-component of vorticity are mainly created on the symmetrical $z = 0$ plane by the reconnection process. In the deceleration and stopping phases of the plates, the bound vortices on both plates begin to shed from the plates. During shedding, the bound vortices contact and cancel the vorticity of each other. The horizontal vortex tubes are created by the reconnection process and serve as the longitudinal parts of the closed vortex loop in region A. This process occurs gradually, not instantly (figures 4.7(a) and 4.7(b)). All of the bound vortex shedding downstream is not involved in the reconnection

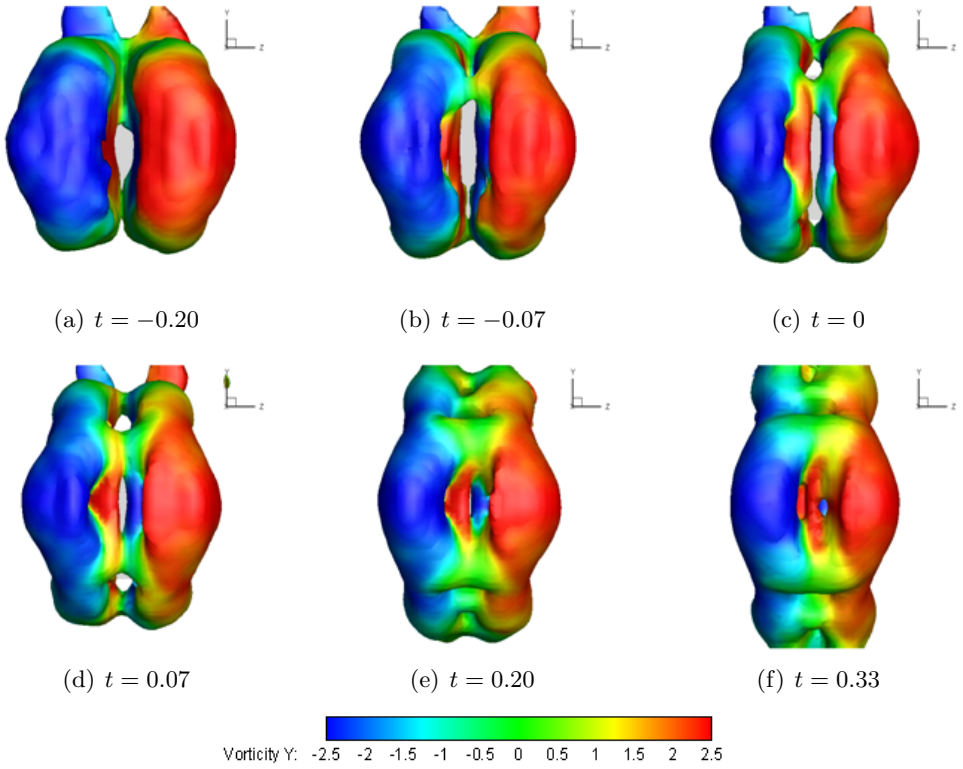

(a) $t = -0.20$ (b) $t = -0.07$ (c) $t = 0$

(d) $t = 0.07$ (e) $t = 0.20$ (f) $t = 0.33$

Figure 4.8: Vortex reconnection process in the AR $= 1$ and $\phi = 45°$ case. The view is from $-x$. Iso-surfaces of $|\boldsymbol{\omega}| = 2.5$ are used.

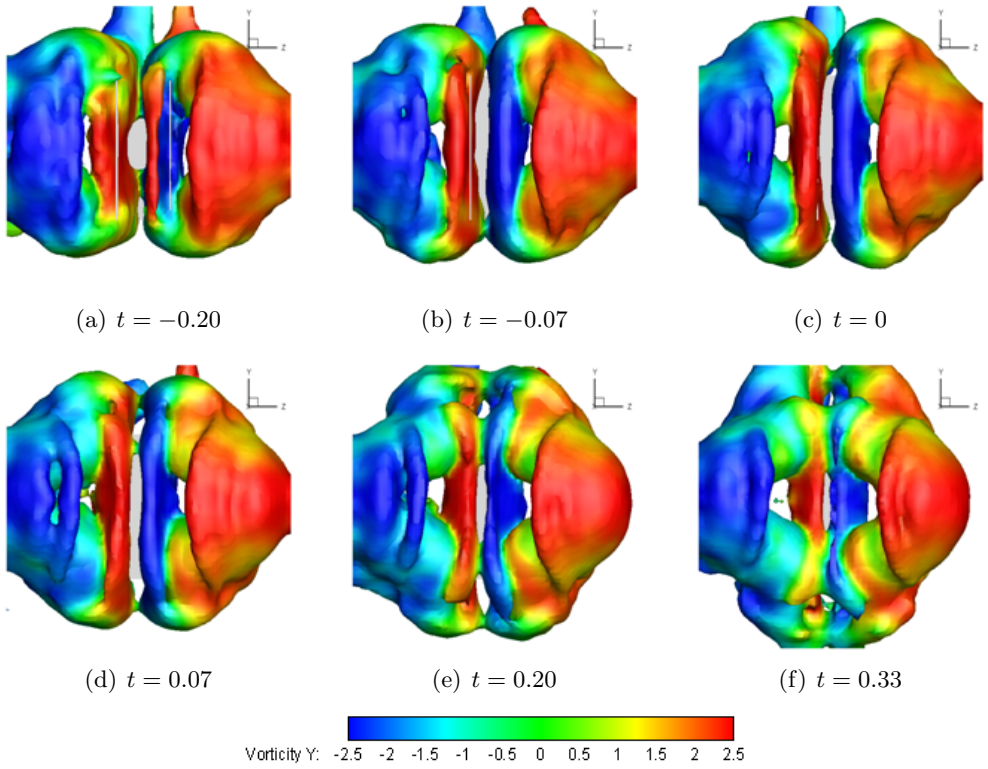

(a) $t = -0.20$ (b) $t = -0.07$ (c) $t = 0$

(d) $t = 0.07$ (e) $t = 0.20$ (f) $t = 0.33$

Figure 4.9: Vortex reconnection process in the AR $= 1$ and $\phi = 90°$ case. The view is from $-x$. Iso-surfaces of $|\boldsymbol{\omega}| = 2.5$ are used.

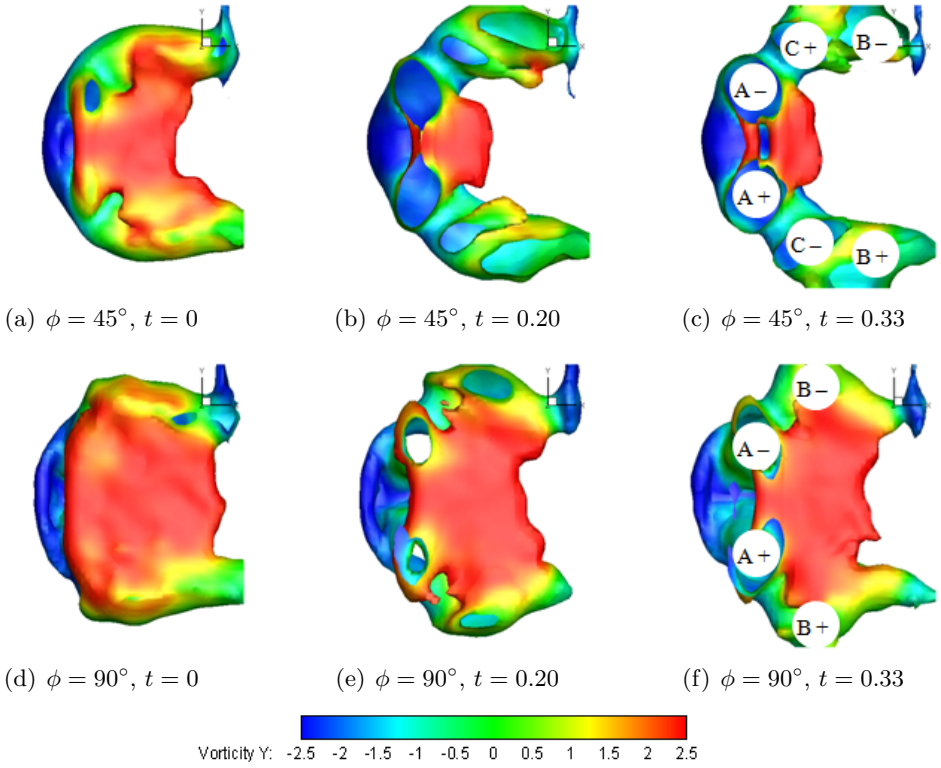

(a) $\phi = 45°$, $t = 0$ (b) $\phi = 45°$, $t = 0.20$ (c) $\phi = 45°$, $t = 0.33$

(d) $\phi = 90°$, $t = 0$ (e) $\phi = 90°$, $t = 0.20$ (f) $\phi = 90°$, $t = 0.33$

Figure 4.10: Bound vortex shedding and reconnection in $\phi = 45°$ and $\phi = 90°$ cases. The view is from $+z$. The flow field in the positive z-domain is removed to show the reconnection regions A, B, and C on the $z = 0$ plane. Plus or minus sign next to the letter means the sign of the ω_z on the $z = 0$ plane, which is created by the reconnection process. Iso-surfaces of $|\boldsymbol{\omega}| = 2.5$ are used. A contour of ω_y is colored on the iso-surface.

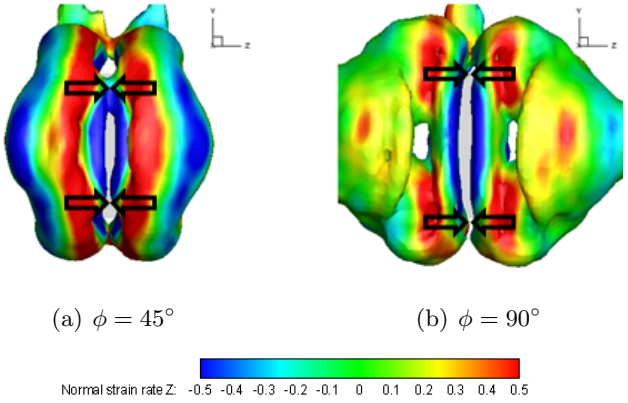

(a) $\phi = 45°$ (b) $\phi = 90°$

Figure 4.11: Normal strain rate in the z-direction ($\mathrm{d}u_z/\mathrm{d}z$) on the vortex at $t = 0$. The view is from $-x$. Iso-surfaces of $|\boldsymbol{\omega}| = 2.5$ are used. A contour of $\mathrm{d}u_z/\mathrm{d}z$ is colored on the iso-surface.

process. Some remains behind the vortex loop moving downstream.

In figure 4.11, the normal strain rate in the z-direction, $\mathrm{d}u_z/\mathrm{d}z$, was plotted on the iso-surface of vorticity magnitude at $t = 0$. The fluid elements of the shedding bound vortices near the $z = 0$ plane are under compression in the z-direction; $\mathrm{d}u_z/\mathrm{d}z$ is negative. However, the fluid elements of the tip vortex near the $z = 0$ plane are stretched in the z-direction. In the corner of the plates where the compression of the bound vortices is weak, the stretched tip vortex induces the formation of vortex tubes connecting two tip vortices.

The new vortex tubes of ω_z by the reconnection process are also found in side-edge vortices near the shafts (region B of figure 4.10). Part of the bound vortex near the shaft cannot shed downstream as fast as the bound vortex near the tip edge, and the reconnection process inside the gap of the plates contributes to the connection of the two side-edge vortices in region B. The vortices in both plates are also connected in region C. Whereas regions A and B are common in all clapping cases studied here, the strength of the vortex tubes in region C is dependent on the stroke angles. It the 90° case, region C was not strong enough to confirm its identification. Probably, the plate deceleration time affects the reconnection process in region C. The time for deceleration of the plate is twice shorter in the 45° case. Therefore, the bound vortex shedding process is more abrupt. While the bound vortex (red contour in figure 4.10) of the 90° case sheds smoothly and slowly downstream, the bound vortex of the 45° case suffers severe deformation near $t = 0$. The abrupt shedding and the resultant severe deformation of the bound vortex may be an important factor to initiate the vortex reconnection in region C.

4.3.3 Aspect-ratio effects

In order to investigate how the aspect ratio of the plate can affect vortex structure and thrust performance, plates with two different chord lengths ($c = 12$ cm for AR = 0.66 and 4 cm for AR = 2) were used in addition to the plate used in the above sections ($c = 8$ cm for AR = 1).

4.3.3.1 Circulation and impulse

For three different ARs, the circulation of the tip vortex at sections normal to the y-axis is presented in figure 4.12. The circulations are taken at $t = -0.26$, which corresponds to

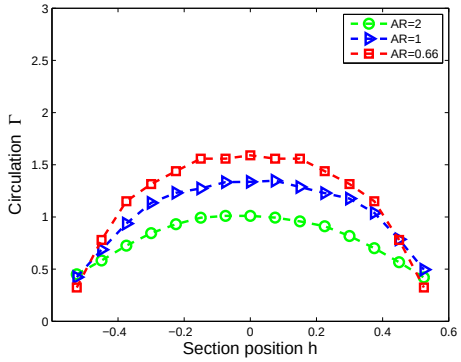

(a) $\phi = 45°$, $t = -0.26$

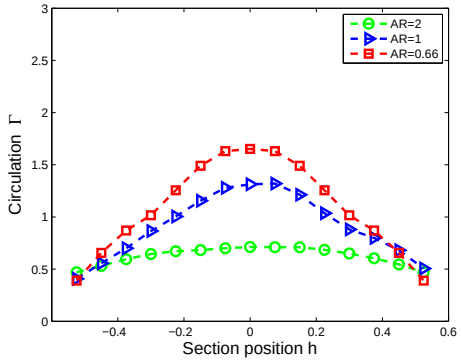

(b) $\phi = 45°$, $t = 0$

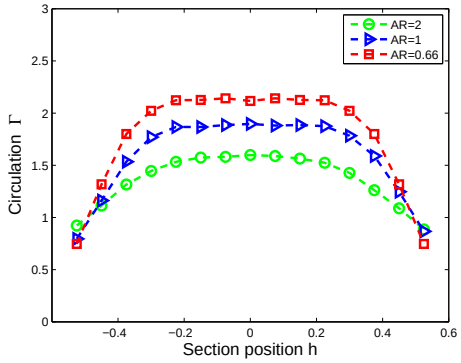

(c) $\phi = 90°$, $t = -0.26$

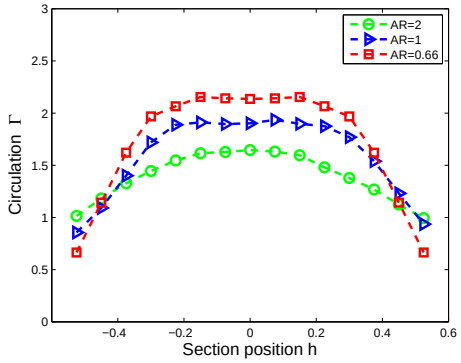

(d) $\phi = 90°$, $t = 0$

Figure 4.12: Circulation Γ of the tip vortex at the sections normal to the y-axis for single-plate cases at $t = -0.26$ and 0. For both stroke angles, three ARs (= 2, 1 and 0.66) are considered. The position for the sections h is defined as the y-coordinate of the section divided by the chord c.

$\theta = 11°$ for the $\phi = 45°$ case and $\theta = 6°$ for the $\phi = 90°$ case, and t = 0, which corresponds to $\theta = 0°$. Only a single plate in the positive z was used by removing the other plate in the negative z. It should be noted that the section h is obtained by dividing the physical y-coordinate by the chord c. The same h for three different AR cases means that the relative position of the section along the tip edge is the same. In the AR = 0.66 case, the mapped flow volume was not enough to include the whole vortex structure. The plate was moved up 40 cm in the y-direction during the DDPIV process. Then, the upper half of the flow field was mirrored from the lower half with respect to the symmetrical plane, $h = 0$. For this reason, in the AR = 0.66 case, only circulations in $h < 0$ are measured, and these values are mirrored for $h > 0$ with the assumption that circulation is symmetric with respect to $h = 0$.

In both 45° and 90° cases, the circulation of the AR = 0.66 case has the highest magnitude at most sections of the tip vortex. As the section h moves closer to the side edge, the circulation becomes smaller since the different vorticity component ω_x is prevalent near the side edge. To explain the trend that the plate with the lower AR generates more circulation, we first examine the effects of side-edge vortices on the strength of the tip vortex. The side-edge vortices induce flow normal to the surface of the plate. The induced flow by side-edge vortices has a negative effect on the circulation of the tip vortex by decreasing the effective rotating velocity of the plate. Here, the effective rotating velocity means the flow velocity encountered by the plate when the reference frame rotating with the plate is used. This is analogous to the effect of a wing tip vortex on the effective angle of attack decrease in the steady flight of an airplane. If the chord of the plate is shortened, the induced flow of the side-edge vortex becomes more dominant and the circulation of the tip vortex get smaller. However, this idea falls short in explaining why the circulation of the AR = 0.66 case is always higher than the other cases during the whole rotating time from the start. When the plate starts to rotate, the side-edge vortex is not developed enough to affect the circulation growth of the tip vortex. Thus, an alternative approach, without relying on the side-edge vortex effect, is required to explain the dependence of circulation on the aspect ratio.

The circulation of the tip vortex indicates the amount of vorticity passing around the tip edge because of the pressure difference between the pressure (front) and suction (back) surfaces of the plate. As a way to show how the aspect ratio affects the pressure distribution

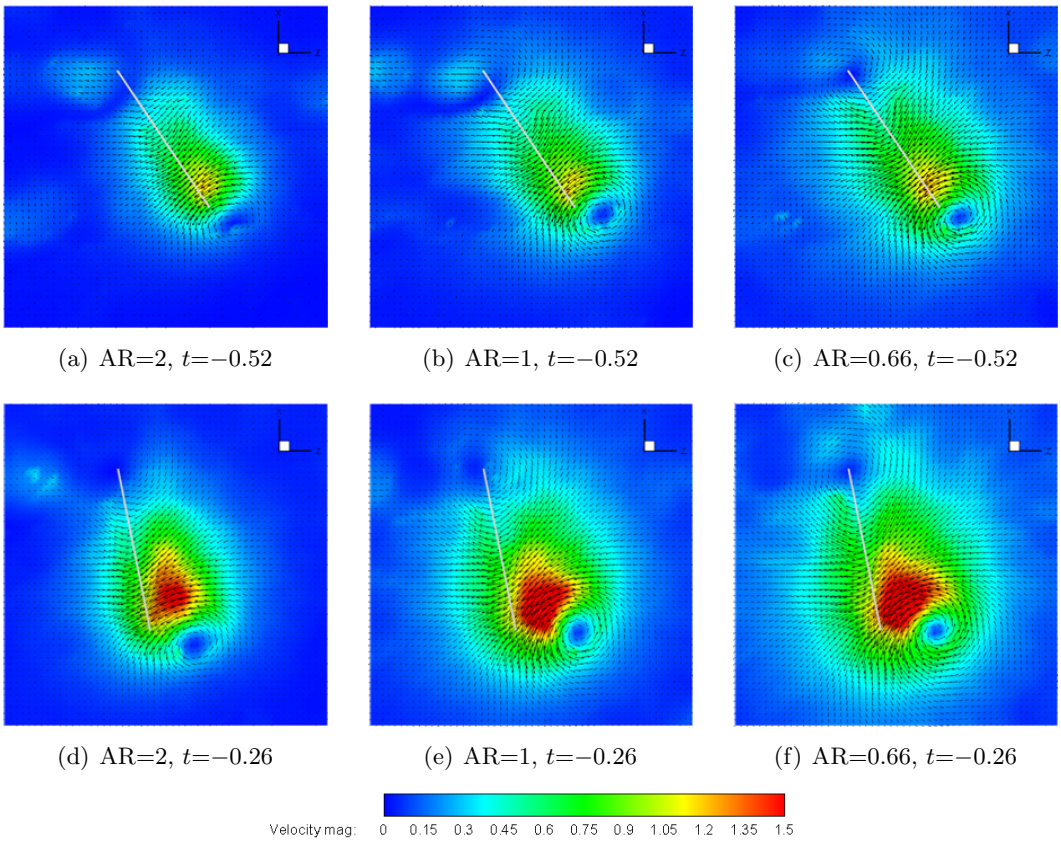

(a) AR=2, t=−0.52 (b) AR=1, t=−0.52 (c) AR=0.66, t=−0.52

(d) AR=2, t=−0.26 (e) AR=1, t=−0.26 (f) AR=0.66, t=−0.26

Figure 4.13: Velocity distribution on $h = 0$ section for the $\phi = 45°$ cases. The angle θ between the rotating plate and the $z = 0$ plane is 33.75° at $t = -0.52$ and 11.25° at $t = -0.26$. Both velocity vector and velocity magnitude contour are plotted. The view is from $+y$, and the plate rotates clockwise in this view.

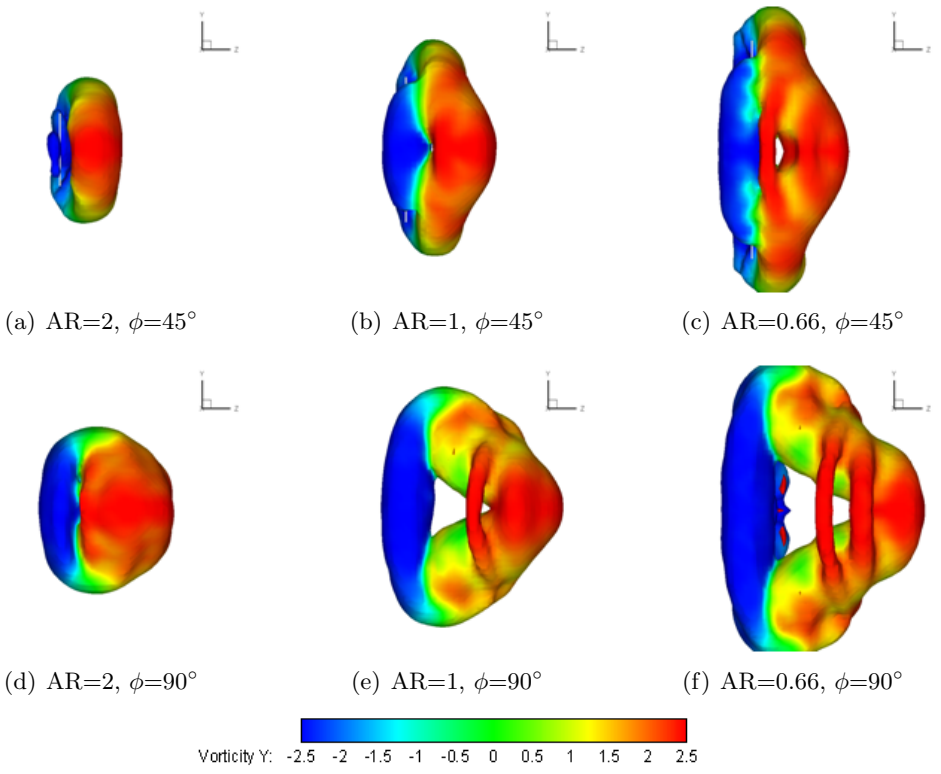

(a) AR=2, ϕ=45° (b) AR=1, ϕ=45° (c) AR=0.66, ϕ=45°

(d) AR=2, ϕ=90° (e) AR=1, ϕ=90° (f) AR=0.66, ϕ=90°

Figure 4.14: Comparison of vortex structures of single-plate cases for three different ARs (= 2, 1 and 0.66) and two different stroke angles (ϕ = 45° and 90°) at $t = 0$. The view is from $-x$. Iso-surfaces of $|\boldsymbol{\omega}| = 2.5$ are used.

around the plate, figure 4.13 demonstrates that velocity distribution around the rotating plate on the $h = 0$ section is also significantly affected by the aspect ratio. In the lower AR case, more fluid is accelerated toward the back surface of the rotating plate and more fluid is pushed out from the front surface of the rotating plate than the higher AR case. This trend is generally applied to other horizontal sections as well as the $h = 0$ section at any rotating time. Therefore, from the simple relation between the pressure gradient and the acceleration of the fluid element, the pressure difference between pressure and suction surfaces of the rotating plate will be larger for the lower AR. In this sense, we argue that, as the aspect ratio decreases (the chord length increases), more vorticity is generated and accumulated around the tip edge because of the increased pressure difference between the pressure and suction surfaces of the plate. In addition to the tip vortex, the strength of the side-edge vortex, the magnitude of circulation for the vorticity component parallel to the side edge, is also inversely related to the aspect ratio.

The shape of the tip vortex also depends on the aspect ratio (figure 4.14). As the aspect ratio decreases, the separation of the tip vortex from the tip edge happens earlier, and the distance between the tip edge and the central part of the tip vortex becomes larger. This early separation process results in the larger inner area of the vortex structure. In the 90° case, the difference in tip vortex shapes among three different ARs is more conspicuous than that of the 45° case at $t = 0$. One possible explanation for the dependence of tip vortex separation on the aspect ratio is that the side-edge vortices affect the tip vortex motion. Two counter-rotating side-edge vortices induce the tip vortex to follow the motion of the tip edge. As the distance between the two side-edge vortices get larger, their effect on the motion of the tip vortex, especially near $h = 0$, will be diminished. On the other hand, near the corner where the tip vortex and the side-edge vortex meet, the vortex has a high curvature. Thus, the self-induced velocity of the vortex near the corner will be high in the direction bi-normal to the tip edge and the side edge, enough to follow the plate motion.

In figure 4.12, the AR = 2 and $\phi = 45°$ cases show the distinct decline of circulation between $t = -0.26$ and $t = 0$. When the plate decelerates, the bound vortex starts to roll up to form the stopping tip vortex. Since the starting tip vortex is quite close to the tip edge in the AR = 2 and $\phi = 45°$ case, some portion of the bound vortex is entrained by the starting tip vortex. Consequently, the strength of the starting tip vortex is annihilated because these two vortices have vorticity of opposite signs. Note that the stopping tip vortex of the AR = 2 and $\phi = 45°$ case is not formed as clearly as the other cases in figure 4.14. If the starting and stopping tip vortices are in a longer distance during deceleration such as the $\phi = 90°$ cases, the circulation of the tip vortex does not suffer the distinct decline.

The circulation of the tip vortex at $t = 0$ is compared between single-plate cases and double-plate cases of $\phi = 45°$ in figure 4.15. For all three ARs (2, 1, and 0.66), double-plate cases produce the higher circulation along the tip edge. The increase of the circulation from the single-plate case to the double-plate case is higher as the aspect ratio is lower; the amount of circulation augmentation is negligible in $\phi = 90° \sim 135°$ of the AR = 2 case. This result means the change in pressure distribution near the plate from the single-plate case to the double-plate case depends on the aspect ratio. For example, in the small stroke angle case, by the rotation of the plate, the flow away from the plate is induced in front of the pressure surface. When the two plates are close, the flow induced by one plate increases the stagnation pressure on the pressure surface of the other plate and, equivalently, the

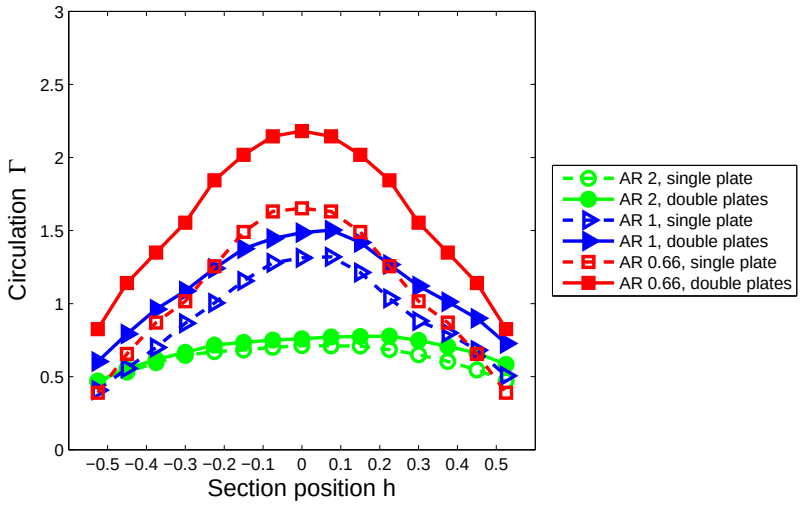

Figure 4.15: Comparison of tip vortex circulation Γ between single-plate and double-plate cases of AR = 2, 1 and 0.66 at $t = 0$. The stroke angle ϕ is 45° ($\theta_f = 0°$).

effective rotating velocity. Thus, the tip vortex of one plate is strengthened by the induced flow of the other plate. Meanwhile, it is possible that the induced flow goes out of the gap between the plates through the upper and lower side edges instead of impacting on the tip vortex strength. If the chord length of the plate is short, a greater portion of fluids between the plates will leak through the upper and lower side edges than the lower AR case with a longer chord length; this results in less gain in the vortex strength.

The effect of the aspect ratio on total impulse in the x-direction I_∞ shows trends similar to that of the circulation (figure 4.16). Over the stroke angle range from 45° to 180°, I_∞ per plate increases as the aspect ratio decreases from 2 to 0.66. In double-plate cases, more impulse is created per plate compared to the single-plate case. The amount of impulse gain from the single-plate case to the double-plate case is larger in the lower AR. The total impulse acting on the model ($\int_0^\infty F_x(t)\mathrm{d}t$) has the same magnitude as the total hydrodynamic impulse acting on the fluid ($\rho \int_{V_\infty} \boldsymbol{x} \times \boldsymbol{\omega} \mathrm{d}V/2$). From this relation between the total hydrodynamic impulse and vorticity distribution, the impulse acting on the model is highly related to the circulation of the vortex. Moreover, the tip vortex separated from the tip edge during plate rotation increases the moment of the y-component of vorticity inside the tip vortex ($|z \times \omega_y|$) and, therefore, contributes to increasing the magnitude of the hydrodynamic impulse.

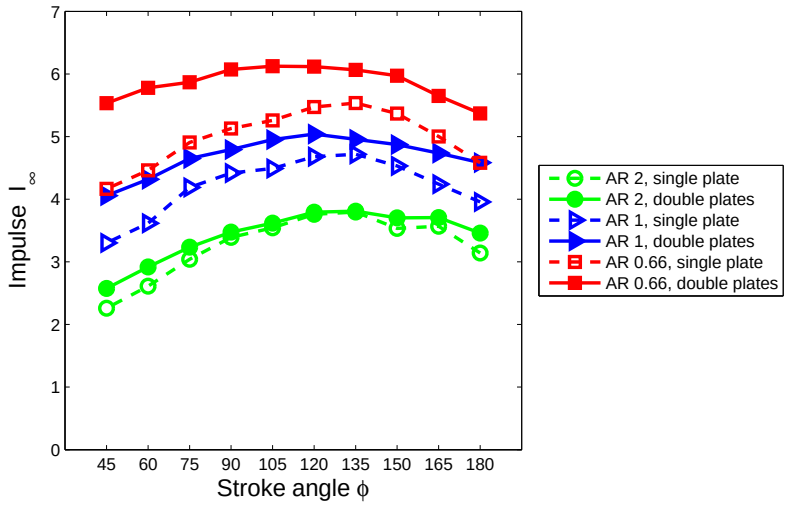

Figure 4.16: Total impulse I_∞ of three different AR cases (2, 1 and 0.66) in various stroke angles ($\phi = 45^\circ \sim 180^\circ$, $\theta_f = 0^\circ$). Both single-plate and double-plate cases are considered for each AR. $I_\infty = \int_0^\infty F_x(\tau)\mathrm{d}\tau / \frac{1}{2}\rho U^2 \hat{r}_2^2 ST$ (see Eq. 4.2). Note that the denominator in the equation is proportional to the chord of the plate in our model.

According to the airfoil theory, the higher AR is better for the larger lift coefficient during steady forward flight because of the downwash effect of the tip vortex. However, in our model, the non-dimensional impulse (and thrust coefficient) is larger for the lower AR (figure 4.16). If the x-direction is assumed to be the lift direction, the motion of our model is similar to the power stroke of the hovering mode with an inclined stroke plane or the very slow forward flight mode of flying animals. In these modes, the propulsor of the lower AR generates the larger lift coefficient during a power stroke according to results presented here. In the lower AR, the tip vortex is the large portion of the whole vortex structure. The dominance of the tip vortex in the whole vortex structure is advantageous in propulsive force generation for the propulsion modes to which our model applies. The advance ratio is one of the parameters characterizing the unsteadiness of the flapping motion and is defined as the forward speed of the body divided by the mean flapping speed of the wing (Ellington, 1984b). Then, we can infer that the effect of a small AR wing on lift generation may be reversed from positive to negative when the advance ratio of the flight increases from zero.

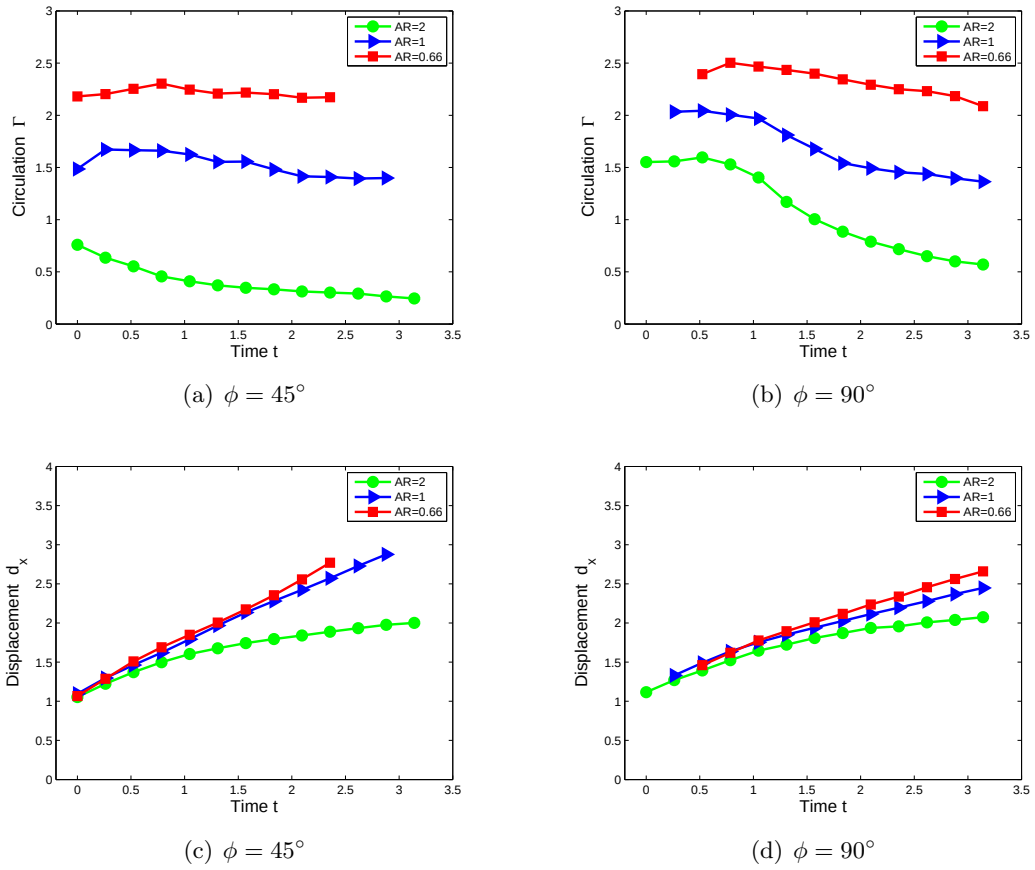

(a) $\phi = 45°$ (b) $\phi = 90°$

(c) $\phi = 45°$ (d) $\phi = 90°$

Figure 4.17: Circulation Γ ((a) and (b)) and x-directional displacement d_x ((c) and (d)) of the vortex structure after the plates stop. Γ and d_x are taken on a section of $y = 0$ and $z > 0$ for double-plate cases. Γ and d_x values are discarded when a part of the vortex is out of the measured flow field on the section.

4.3.3.2 Wake dynamics

The dynamics of the vortex loop moving downstream also depends on the aspect ratio of the plate. In this section, the evolution of the vortex loop is investigated for the double-plate cases of three different aspect ratios (2, 1, and 0.66). In the $\phi = 45°$ cases, the propagation speed of the center of the vortex structure on the $y = 0$ plane is inversely related to the aspect ratio (figure 4.17(c)). This trend is not surprising because the circulation of the tip vortex depends on the aspect ratio. The large circulation of the tip vortex has a positive effect on the propagation speed of the vortex loop. Notably, the propagation speed of the vortex loop is much lower in the AR = 2 case than the other cases. The delayed wake propagation of the vortex loop for the AR = 2 case is due to entrainment of some portion

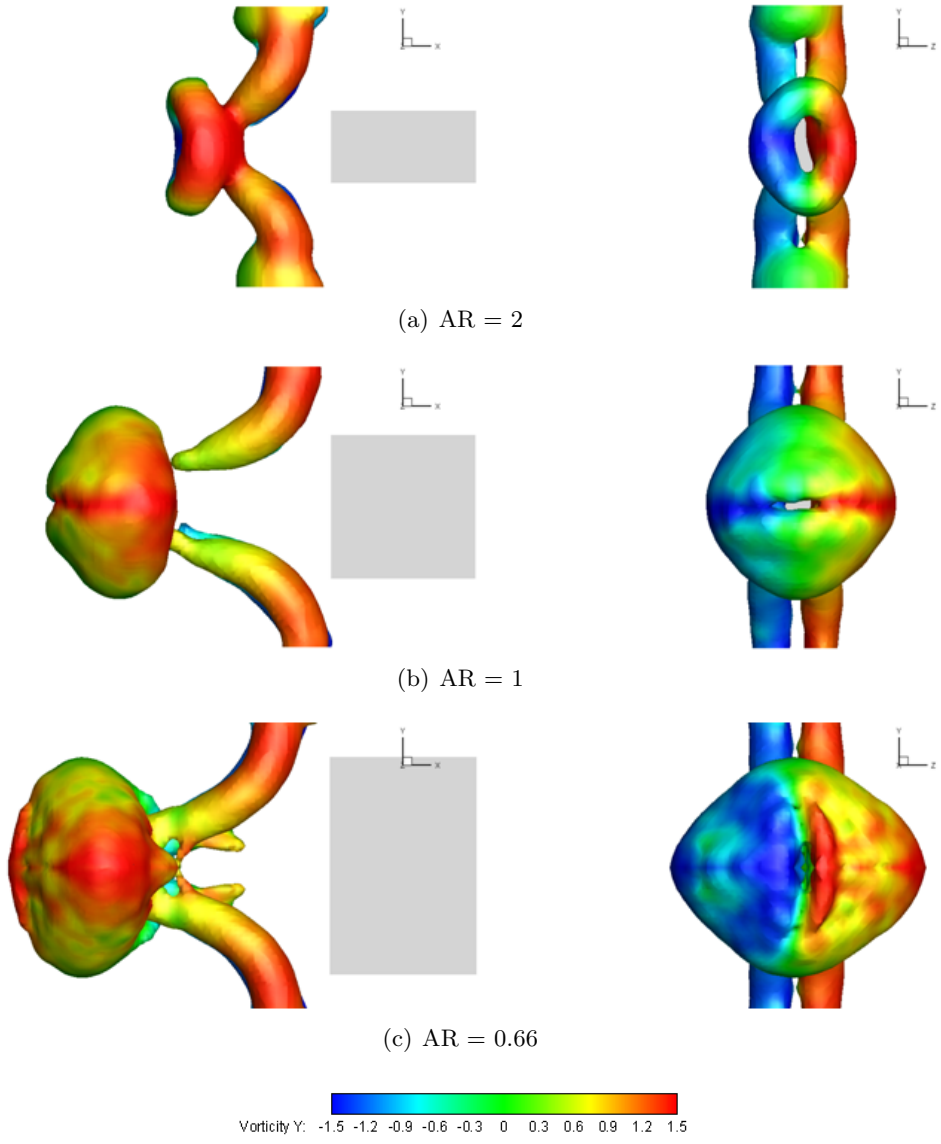

(a) AR = 2

(b) AR = 1

(c) AR = 0.66

Figure 4.18: Effect of aspect ratio on wake structure at $t = 2.09$ for double-plate cases ($\phi = 45°$). The view of the left column is from $+z$, and the view of the right column is from $-x$. Iso-surfaces of $|\boldsymbol{\omega}| = 1.5$ are used.

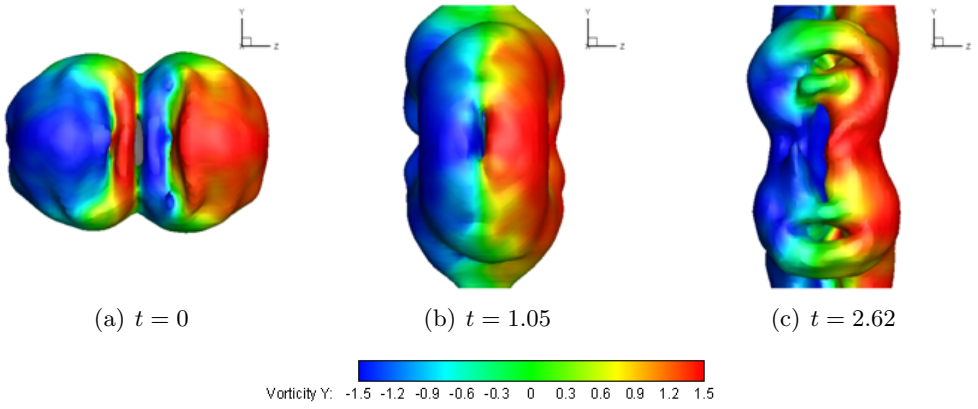

(a) $t = 0$ (b) $t = 1.05$ (c) $t = 2.62$

Figure 4.19: Second vortex reconnection process for the AR = 2 and $\phi = 90°$ case of double plates. The view is from $-x$. Iso-surfaces of $|\boldsymbol{\omega}| = 1.5$ are used.

of the shedding bound vortex into the starting tip vortex in the same side as mentioned in §4.3.3.1. Through entrainment of the bound vortex, the strength of the tip vortex that composes the lateral part of the vortex loop is diminished significantly after $t = 0$ (figure 4.17(a)). For this reason, the vortex loop is much weaker in the AR = 2 case than the other cases (figure 4.18). In the AR = 2 case, all of the bound vortex is not entrained into the tip vortex on the same side. Some part of the bound vortex on both sides is involved in the reconnection process to make a vortex loop.

In the 90° case, the difference between the AR = 2 case and the other AR cases is not as significant as the 45° case in terms of the propagation speed and circulation of the vortex loop (figures 4.17(b) and 4.17(d)). In the AR = 2 case of $\phi = 90°$, the tip vortex is farther away from the tip edge during rotation than the 45° case and, consequently, free from the entrainment of the bound vortex on the same side. Interestingly, in addition to the first reconnection, the lateral parts of the vortex loop reconnect and create small longitudinal vortex tubes inside the vortex loop when it moves downstream (figure 4.19(c)). This second reconnection is not found in the other AR cases of $\phi = 90°$. Even though the stroke angle is large, the tip vortex follows the plate motion without significant separation in the AR = 2 and $\phi = 90°$ case (see figure 4.14). When the plate stops, two tip vortices on both sides impact each other on the $z = 0$ plane, and the vortex loop elongates vertically. Probably the strong impact of tip vortices, followed by severe elongation, causes the secondary reconnection process of the vortex loop. In the AR = 2 case of figure 4.17(b), the sudden drop in circulation after $t = 1$ demonstrates that there is a strong collision of two tip vortices

and a consequent annihilation of vortex strength. Even though there is also the sudden decline of the vortex loop circulation in the AR = 1 case, the second reconnection is not distinguishable in figure 4.6. The fast change of the vortex shape, the change of major and minor axes, may prohibit the second reconnection in the AR = 1 case. On the other hand, in all $\phi = 45°$ cases of AR = 2, 1, and 0.66, the secondary reconnection of the vortex loop in the wake does not happen even though the lateral parts of the vortex loop contact each other on the $z = 0$ plane. Figure 4.17(a) points out that the the circulation of the vortex loop does not drop significantly in the wake, which means the impact of the collision is not strong enough to weaken the strength of the vortex loop. The stroke angle is not large enough to cause the strong impact by inertial motion of two tip vortices toward the $z = 0$ plane. From this observation, the intensity of tip vortex collision is important to determine whether the second reconnection happens in the wake.

4.3.4 Stopping-angle dependence of bound vortex shedding

In all double-plate cases shown above, one vortex loop forms from vortex structures in both plates. When the plates stop, the final angle between the two plates is zero in those cases. To study how the final angle between two plates influences the formation of the vortex loop, three cases with different final angles ($\theta_f = -6°$, 10°, and 20°) are compared (figure 4.20). The stroke angle ϕ is 45° and the aspect ratio is 1. The $\theta_f = -6°$ case was conducted with the intention of making the tip edges of the double plates nearly meet at $t = 0$. In the $\theta_f = -6°$ case, the shape of the vortex loop is not much different from that of the $\theta_f = 0$ case in §4.3.1.2 except for the occurrence of the second reconnection. The second reconnection happens in the wake. However, they are merged into the vortex loop quickly as the vortex loop changes its shape dynamically.

In the $\theta_f = 10°$ case, the bound vortices shed from both plates move toward the $z = 0$ plane. Because of the time taken for the bound vortex shedding and its approach to the $z = 0$ plane, the growth of the vortex loop is delayed, compared to the $\theta_f = 0°$ cases. After $t = 0$, two starting tip vortices also move toward the $z = 0$ plane. Since the tip vortices are farther from each other at $t = 0$ due to the 20° angle between the two plates, it also takes more time for the vortex loop to compress laterally than in the $\theta_f = 0°$ case. Within the observed time, the vortex loop undergoes only lateral compression and vertical elongation without the subsequent deformation such as the change of major and minor axes. In the

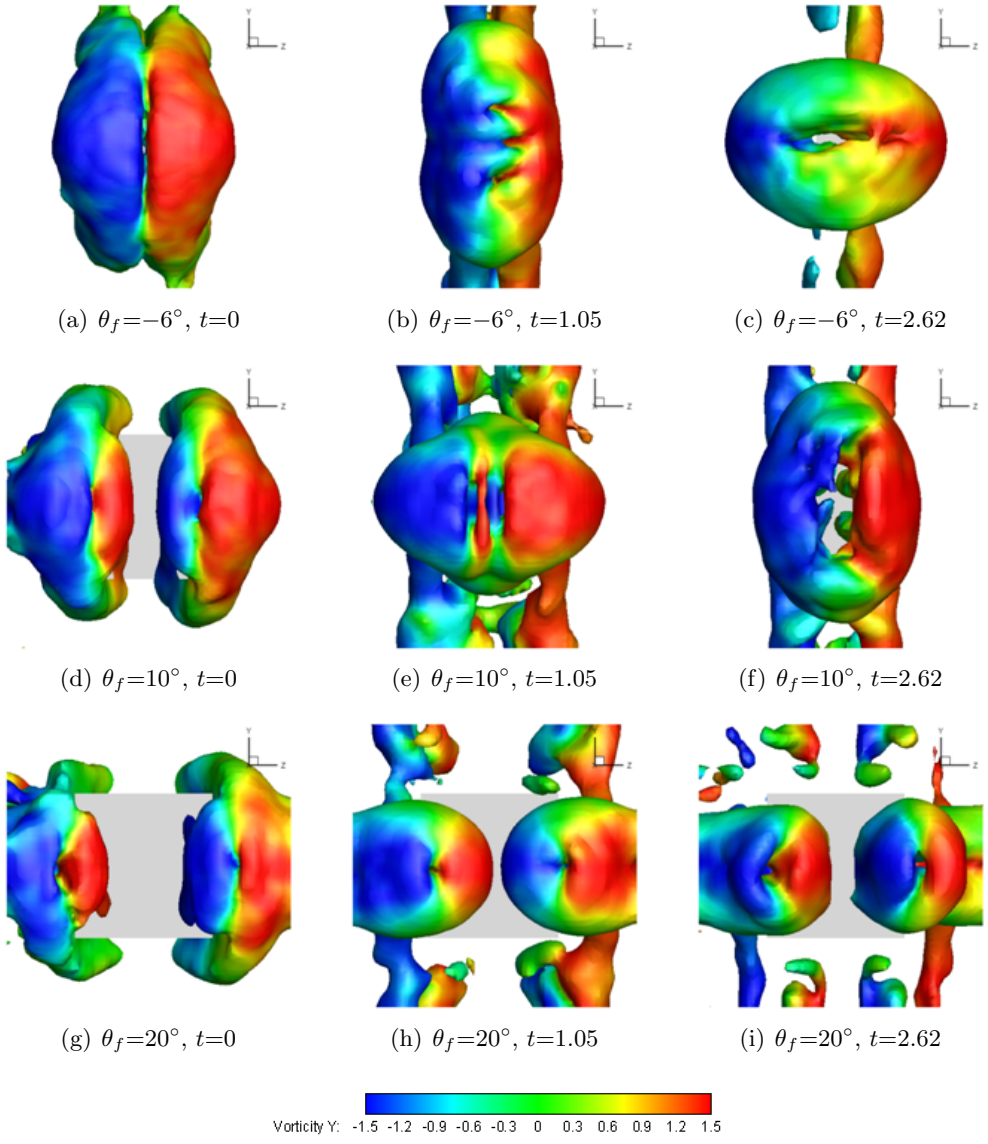

(a) θ_f=−6°, t=0 (b) θ_f=−6°, t=1.05 (c) θ_f=−6°, t=2.62

(d) θ_f=10°, t=0 (e) θ_f=10°, t=1.05 (f) θ_f=10°, t=2.62

(g) θ_f=20°, t=0 (h) θ_f=20°, t=1.05 (i) θ_f=20°, t=2.62

Figure 4.20: Vortex dynamics in the wake for the AR = 1 and $\phi = 45°$ cases of double plates with three different final angles θ_f (−6°, 10°, and 20°). The view is from $-x$. Iso-surfaces of $|\boldsymbol{\omega}| = 1.5$ are used.

$\theta_f = 20°$ case, the reconnection is negligible. When the bound vortices shed from both sides approach each other, only a small portion of the bound vortices is involved in the reconnection process; if the lower vorticity magnitude is used in figure 4.20, tiny vortex tubes connecting the vortex structures on both sides can be seen. As a result, two distinct vortex loops are developed in the wake.

4.3.5 Vortex formation time

Here, we define the vortex formation time $\hat{T}$ for our model, and apply it to explain the dependence of thrust performance on optimal vortex formation process. First, single-plate cases are considered. Based on the argument in Dabiri (2009), we define vortex formation time $\hat{T}$ for our model as

$$\hat{T} = \frac{2\Gamma_d}{DU} = \frac{2\Gamma s}{D}, \tag{4.5}$$

where $\Gamma_d (= \Gamma U s)$ is the dimensional total circulation of the tip vortex on the $y = 0$ plane, U is the mean tip velocity, and D is the characteristic length. We calculate the formation time for the vortex at $t = 0$ (i.e., when the plate stops creating vorticity) (figure 4.14). At $t = 0$, the inner area A of the vortex loop projected on the yz-plane is approximately $cl/2$ where c is the chord length of the plate and l is the z-directional distance between the centers of the tip vortex and counter-rotating bound vortex. Since we are interested in force (or impulse) generation in the x-direction, the area projected on the yz-plane is used. Then, the characteristic length D can be calculated as follows.

$$D = \frac{4A}{P} \approx \frac{2cl}{c + 2\sqrt{l^2 + \frac{c^2}{4}}}, \tag{4.6}$$

where P is the perimeter of the vortex loop. We assume that the shape of the vortex projected on the yz-plane is triangle. From Eq. 4.5 and Eq. 4.6,

$$\hat{T} = \Gamma \frac{s}{l} \left(1 + 2\sqrt{\left(\frac{l}{c}\right)^2 + 0.25} \right). \tag{4.7}$$

Table 4.2 summarizes the formation times of several cases, which were calculated from the experimental results. The formation $\hat{T}$ of the $\phi = 90°$ and AR $= 0.66$ case is closer than other cases to the optimal formation time $\hat{T} \approx 4$ for the vortex ring generator model (Gharib

Stroke angle ϕ	45°			90°		
Aspect ratio AR	2	1	0.66	2	1	0.66
Span s(mm)	80	80	80	80	80	80
Chord c(mm)	40	80	120	40	80	120
Vortex Z-distance l (mm)	20	22	33	34	57	68
Circulation Γ	1.10	1.32	1.65	1.64	1.90	2.14
Formation time $\hat{T}$	9.8	10.3	8.5	11.5	7.3	6.3

Table 4.2: Vortex formation time of the single-plate cases. For the $\phi = 45°$ and AR = 2 case, the circulation at $t = -0.26$ was used since the circulation drops abruptly near when the plate stops (figure 4.12) because of the entrainment of the bound vortex.

et al., 1998) and the two-dimensional flapping plate model (Milano & Gharib, 2005). The trend of the formation time in table 4.2 is correlated with the trend of the non-dimensional total impulse shown in figure 4.16; the lower aspect-ratio plate generates more impulse, and its corresponding formation time tends to be closer to the optimal formation time ($\hat{T} \approx 4$). In terms of stroke angle, the plate with $\phi = 90°$ generates more impulse than the plate with $\phi = 45°$, and the formation time of $\phi = 90°$ is closer to the optimal formation time than that of $\phi = 45°$ except the AR = 2 case.

For the double-plates cases, l of the vortex structure is hardly affected by the addition of the plate, compared to the single-plate cases. l is the z-directional distance between the centers of the tip vortex and bound vortex in the positive z-domain. However, the circulation of the tip vortex increases slightly from that of the single-plate cases as mentioned in §4.3.3.1. Even though the plate rotates with the same kinematics in the single-plate and double-plates cases, the circulation augments by adding the plate in the other side. In order to create the circulation equivalent to that of the single-plate case, the displacement of the plate can decrease by virtue of circulation augment. Therefore, in the definition of the formation time for the double plates, we multiply the formation time defined in Eq. 4.7 by the ratio of tip vortex circulation Γ_s for the single plate to Γ_d for the double plates.

$$\hat{T} = \Gamma_s \frac{s}{l} \left(1 + 2\sqrt{\left(\frac{l}{c}\right)^2 + 0.25} \right) \frac{\Gamma_s}{\Gamma_d}. \tag{4.8}$$

The formation times of the double-plates cases are shown in table 4.3. The formation time $\hat{T}$ of the AR = 0.66 and $\phi = 90°$ case is 5.6. This case has the formation time

Stroke angle ϕ	45°			90°		
Aspect ratio AR	2	1	0.66	2	1	0.66
Span s(mm)	80	80	80	80	80	80
Chord c(mm)	40	80	120	40	80	120
Vortex Z-distance l (mm)	19	22	32	39	57	68
Circulation Γ_d	1.10	1.49	2.18	1.66	2.04	2.40
Circulation Γ_s	1.10	1.32	1.65	1.64	1.90	2.14
Formation time $\hat{T}$	9.3	9.1	6.6	10.6	6.8	5.6

Table 4.3: Vortex formation time of the double-plates cases. For the AR = 1 and 0.66 cases of $\phi = 90°$, some part of the tip vortex is out of the fluid volume. Thus, l of the single-plate case was used. The circulation Γ_s of the single-plate cases is from table 4.2.

closest to the optimal vortex formation time $\hat{T} \approx 4$ in all cases considered here including the single-plate cases. Correspondingly, the non-dimensional impulses of this case is the highest (figure 4.16). Here, we explored the vortex formation time of the clapping model. Based on the analysis shown in this section, we may be able to check whether the clapping motion of animal propulsors in nature (e.g., butterfly wings) is optimized in terms of vortex formation.

4.4 Concluding remarks

Vortex dynamics and thrust performance of clapping plates were investigated experimentally. The reconnection process of bound vortices and the consequent vortex loop formation are the most characteristic aspect of double-plate clapping cases, compared to single-plate cases. Because of the small gap between clapping plates, the bound vortex cannot shed into the wake while maintaining its strength, but interacts with the bound vortex of the opposite sign on the other side. The interaction of two bound vortices results in the gradual growth of longitudinal parts of the vortex loop.

Depending on kinematical and geometrical conditions of the plate such as stroke angle and aspect ratio, the vortex loop has various phases of deformation in the wake. The lateral compression and vertical elongation of the vortex loop is commonly seen in the cases studied here, especially in small stroke angle cases. In some cases, this deformation is followed by a change in major and minor axes, or the second reconnection process of the vertically elongated vortex loop. In addition to the source for the vortex reconnection, the bound

vortex can have other roles in vortex loop formation. If the bound vortex is entrained into the tip vortex on the same side as soon as the plate decelerates, the strength of the vortex loop decreases significantly. If the final angle between two clapping plates is large, the bound vortices are free from the merge process and can move downstream as a strong part of a two-vortex-loop system.

The total impulse acting on the model is determined soon after the plate stops, regardless of the continuous deformation of the vortex in the wake. Thus, vorticity distribution at which the plate stops was studied in order to find the effect of the aspect ratio and the number of plates on the total impulse. As the aspect ratio of the plate decreases, the impulse inversely increases over a broad range of stroke angles in both single-plate and double-plate cases. Double-plate cases generally produce the larger impulse per plate than single-plate cases. The thrust advantage of double plates over a single plate becomes smaller for the higher aspect-ratio case. These results give some insights in understanding when the low aspect-ratio wing of some insects such as a butterfly can be advantageous aerodynamically. In slow forward flight modes or drag-based propulsion modes such as take-off and landing, the low aspect-ratio wing may be more efficient in that it can generate a higher thrust coefficient during a power stroke. Additionally, in the clapping mode of the wings during pronation, low aspect-ratio wings may be more efficient than high aspect-ratio wings in terms of thrust augmentation by the interaction of a wing pair. Admittedly, it is necessary to explore more complicated kinematics and wing shapes in order to generalize this idea. Moreover, in this study, the vortex formation time for the single-plate and double-plates cases was investigated in order to check if the vortex structure of our model is optimized for efficient thrust generation.

Even though several cases are performed in this study by varying aspect ratios and stroke angles, it should be emphasized that these cases do not comprehend all possible scenarios of vortex formation in clapping models. Rather, this study was intended to find out what are important dynamical mechanisms in the evolution of the vortex structure generated by clapping models. Especially, we focused on the dynamics of the tip vortex, the bound vortex and the vortex loop, as well as its relation with thrust generation. One of our future plans is to investigate the effect of the wing's aspect ratio on vortex structure and propulsive performance under various advance ratios by using a model to mimic flying animals.

Chapter 5

Translating and rotating motions with 45° angle of attack

5.1 Background

The development of a stable leading-edge vortex over the wings of hovering insects has been recognized as one of unsteady lift enhancement mechanisms (e.g., Maxworthy, 1981; Ellington *et al.*, 1996; Birch & Dickinson, 2001). It has been reported that the presence of a spiral spanwise flow in the leading-edge vortex core of hawkmoths (Re $\sim$ 4000) delays the vortex shedding by draining vorticity of the leading-edge vortex into the tip vortex (Ellington *et al.*, 1996). However, Birch & Dickinson (2001) claimed that, in the lower Reynolds number flying regimes of hovering fruit flies (Re $\sim$ 100), the spanwise flow inside the leading-edge vortex core may not be an important vortex stabilization mechanism. They reported an experiment in which they blocked the spanwise flow and observed only a small decrease in lift magnitude. According to Birch *et al.* (2004), the magnitude of the spanwise flow in the leading-edge vortex core at Re = 120 is not as large as that of Re = 1400. Birch *et al.* (2004) suggested that the transport of vorticity inside the leading-edge vortex took different forms in Re = 120 and 1400. In a computational study, Shyy & Liu (2007) demonstrated that instantaneous streamlines near the leading edge were also varied drastically within the Reynolds number 10 $\sim$ 6000. Lentink (2008) showed that, in spite of the differences in spanwise flow distribution, the leading-edge vortex is stable during the rotating motion of a wing model for the Reynolds number 100 $\sim$ 14000. He concluded that the mechanism for leading-edge vortex stability does not depend on the Reynolds number, but is governed mainly by rotational acceleration.

Due to significant three-dimensional effects, the study of the unsteady flow structure generated by the low aspect-ratio insect wings still remains a challenging problem. For a better understanding of the fluid dynamical mechanisms involved in insect flight, it is necessary to study the formation and morpho-dynamics of the whole vortex structure as well as those of the leading-edge vortex. In this study, we try to address this issue by providing a more global view of vortex formation in hovering insects by employing wing-like mechanical models and a three-dimensional flow mapping technique, defocusing digital particle image velocimetry (DDPIV) (Willert & Gharib, 1992; Pereira & Gharib, 2002).

Instead of simulating specific insect flight patterns, we used simple translating and rotating kinematic patterns, and a simple rectangular plate model with constant chord length along the span. The angle of attack was 45° for all cases. This angle of attack was chosen because this study was motivated from the wing motion of the hovering insects that usually use a high angle of attack. Translation and rotation cases of Re = 1100 were compared to find different characteristics in vortex structures and spanwise flows between these cases. Also, for rotating plates, the effect of viscosity on the vorticity field and spanwise flow were investigated by comparing the Reynolds number 60 and 8800 cases.

5.2 Experimental setup

5.2.1 Model and kinematic conditions

A glass tank of 870 × 430 × 360 mm^3 was used for the experiment (figure 5.1). The tank was filled with water for high Reynolds number cases and filled with mineral oil (Chevron Superla white oil, $\nu = 140$ mm^2/sec, $\rho = 0.84$ g/cm^3) for low Reynolds number cases. A lead-screw driven traverse (Velmex Inc.) and a micro-stepping stepper motor (NEMA 14 and IM483, Schneider Electric Motion) were implemented to translate and rotate a plate model, respectively. The traverse was aligned parallel to the tank wall. For the wing model, a rectangular acrylic plate with area 60 × 137.5 mm^2 and uniform thickness 1.46 mm was used. Even though there was small deflection of the plate tip during rotation, the deflection was negligible and the plate was assumed rigid. The acrylic plate was connected to the vertical aluminum shaft, which was rotated by the stepper motor. The vertical distance between the center of the plate and the free surface was 160 mm. The distance, l, from the plate tip to the shaft center was 150 mm, and the angle of attack of the plate was 45°.

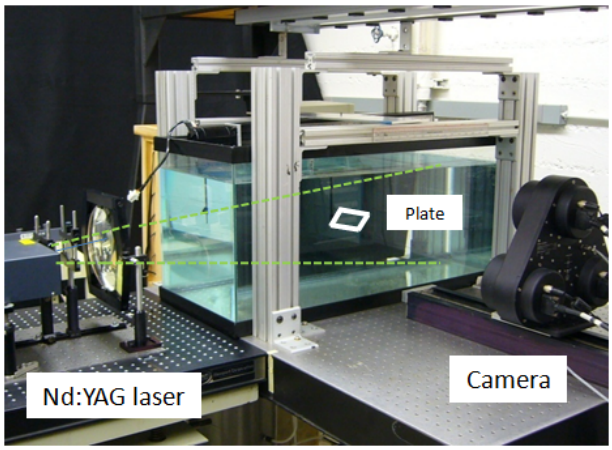

(a)

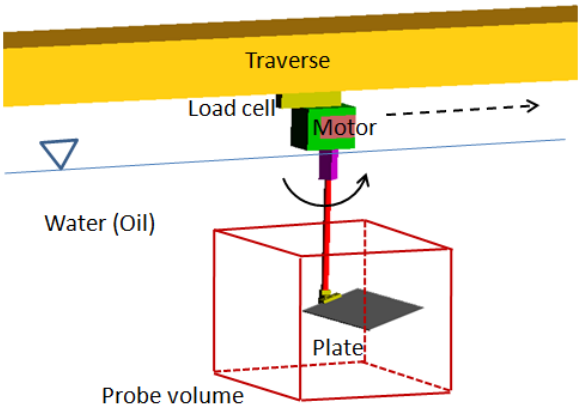

(b)

Figure 5.1: (a) Experimental setup. The plate is indicated by a white rectangle inside the tank. Dashed green lines show the laser cone expanding from a laser in the left side of the tank. (b) Details of a mechanical model. The direction of dashed and continuous lines is the direction of translation and rotation modes, respectively. The cubic shows the approximate size and position of a camera probe volume.

	Kinematic pattern	Re	Fluid	Velocity program	T(sec)	U(mm/sec)
Part 1	Rotation & Translation	1100	Water	Trapezoidal program	16	18.4
Part 2	Rotation	1100	Water	Trapezoidal&	2	147.2
		60	Oil	Sinusoidal programs		

Table 5.1: Summary of experiment cases. T is the total time from start to stop of the plate. U is the mean tip velocity, not maximum tip velocity.

The experiment was composed of two parts. The first part was to compare the vortex formation of a translating plate with that of a rotating plate. For the rotating simulation, the plate rotated with a constant angular velocity with short acceleration at the start and short deceleration at the stop (trapezoidal velocity program, see figure 5.2(a)). For the translation case, the plate translated with the same velocity program as the tip velocity of the rotation case, in order to make the strength of the tip vortex similar in both translation and rotation cases.

In the second part, the effect of viscosity on a vortex formation process was investigated by using fluids with different viscosity, water and oil. In this part, both trapezoidal and sinusoidal velocity programs were considered (figure 5.2(a)). In this study, two basic velocity programs were used to find the effect of velocity profiles on the vortex formation process. For the trapezoidal velocity program, the plate rotated with constant angular velocity except during short acceleration and deceleration. By doing so, the effect of acceleration can be ignored in studying vortex formation after impulsive starting. Next, the sinusoidal velocity program was used to take into consideration the effect of acceleration during rotation; the rotating plate is in an acceleration phase for the first half and in a deceleration phase for the second half. These two velocity programs would be fundamental in studying more complicated wing motions.

Table 5.1 summarizes the information of experimental cases. The Reynolds number in table 5.1 is based on the mean tip velocity (U) and chord ($c = 60$ mm) of the plate. The stroke angle for all rotation cases was 112.5°.

5.2.2 DDPIV process

To map three-dimensional flow fields, a DDPIV system was used. DDPIV is a novel technique to measure 3D position and velocity components of particles within a camera probe

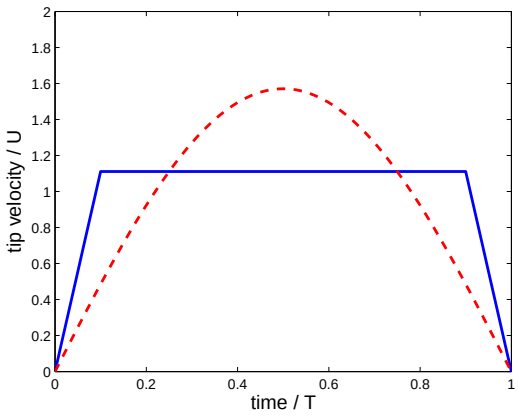

(a)

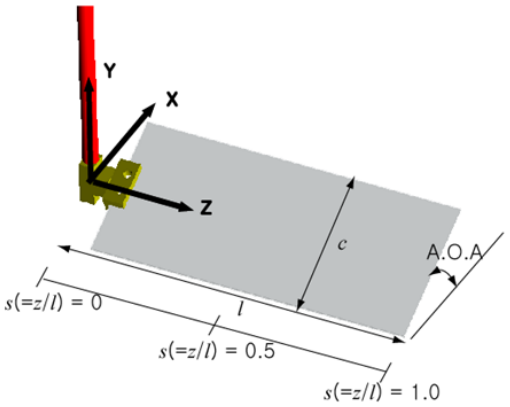

(b)

Figure 5.2: (a) Trapezoidal velocity program (continuous line) and sinusoidal velocity program (dashed line). T is the total time from start to stop, and U is the mean velocity of the tip. (b) Coordinate system used for vector components. The definition of s, which is used frequently to express the position of xy-planar sections normal to the z-axis, is also shown.

volume. In the image captured by a camera with three apertures, one particle image is shown if a particle is on the focal plane of the camera. However, if a particle is out of the focal plane, three particle images appear. From the distance between three particle images, it is possible to construct 3D coordinates of the particles (Willert & Gharib, 1992; Pereira & Gharib, 2002). The DDPIV concept was extended to the system with three cameras in a triangular configuration.

Figure 5.1(a) shows the camera position with respect to the tank. Rigorous calibration was done for both water and oil experiments to deal with multi-media (air-tank glass-water or oil), aberration of lenses, imperfect alignment of setups, etc. The distance between the camera and the tank was adjusted to place the camera probe volume in the middle of the tank. The camera probe volume is about $160 \times 160 \times 160$ mm^3.The details of the volume mapped by a DDPIV system were described in Grothe & Dabiri (2008). The tank was seeded with silver-coated glass spheres of mean diameter 100 μm (Conduct-o-fil, Potters Industries Inc.). An Nd:YAG laser (200 mJ/pulse, Gemini PIV, New Wave Research Inc.) was placed to the left side of the camera, and plano-concave lenses were used to make a laser cone that covered the camera probe volume. The time gap between two laser pulses to take a pair of images was 50 msec for the part 1 experiment and 20 msec for the part 2 experiment. The control computer sent trigger pulses to synchronize operation of the DDPIV camera and the laser, and controlled the motor motion.

The images taken from the camera were processed with the DDPIV software based on Pereira & Gharib (2002); Pereira *et al.* (2006). First, three-dimensional coordinates of the particles inside the tank were found by matching particles in three images captured by the DDPIV camera. Then, from the position information of the particles, the velocity vectors of the particles were calculated from a relaxation method of 3D particle tracking (Pereira *et al.*, 2006). The camera probe volume was not large enough to include the whole vortex structure. Thus, two sets (for the rotation case) or three sets (for the translation case) of the experiment were performed by translating the initial position of the model parallel to the tank wall. Thus, the total fluid volume mapped by multi-sets of the experiment was $280 \times 160 \times 160$ mm^3 for the rotating cases and $360 \times 160 \times 160$ mm^3 for the translating case. The number of cubic grids with size $3 \times 3 \times 3$ mm^3 in the mapped domain was quite large compared to the number of randomly-spaced velocity vectors obtained from one case (≈ 5000). To obtain the number of velocity vectors as many as the number of grids,

the experiment was repeated 25 times under the same conditions with an interval of 90 sec. Then, for each time step, the velocity vectors from each of the 25 cases were collected. The interval between cases was enough to calm the flow generated by the previous case. The velocity vectors collected from 25 cases were interpolated into cubic grids to produce a velocity field. In order to check the dependence of the velocity field output on the number of repeated cases, the velocity vectors collected from 35 cases were compared to those obtained from 25 cases. The difference of velocity components at nodes were within 5%. If the number of cases is much more than 25, the accuracy is expected to improve. However, due to a processing time issue, we chose to limit to 25 cases. After removing outlier velocity vectors and applying a smoothing operator to velocity fields, the vorticity field was obtained by a central difference scheme from the velocity data. The time step between frames was 0.8 sec for the part 1 experiment and 0.1 sec for the part 2 experiment.

The performance of particle position reconstruction in the DDPIV system with three cameras has been characterized (Pereira *et al.*, 2000; Kajitani & Dabiri, 2005; Grothe & Dabiri, 2008; Graff & Gharib, 2008). For a particle in the air, the uncertainty of particle coordinates on the plane parallel to a camera front (in-plane uncertainty) is proportional to the distance of the particle from the camera, while the uncertainty in the direction perpendicular to the camera front (out-of-plane uncertainty) is proportional to its square. For this reason, if the particle is far from the camera, out-of-plane uncertainty of particle coordinates is generally larger than in-plane uncertainty. For the DDPIV system used in this study, the error of the particle position was measured experimentally with the method of Pereira *et al.* (2000). Inside the camera probe volume, the out-of-plane mean error of the particle position was 40 μm for water and 49 μm for oil, and the in-plane mean error was 6 μm for both fluids. As well as particle position reconstruction, the accuracy of velocity calculation using a relaxation method of 3D particle tracking was analyzed (Pereira *et al.*, 2006). In the vortical flow model chosen by Pereira *et al.* (2006), the RMS error of calculated velocity vectors is below 5% as a percentage of the maximum velocity, if the error of particle locations normalized by the maximum displacement of the fluid is within 2.5%.

For lift force measurement, a load cell (miniature beam type, Interface Inc.) was attached to the top of the motor (figure 5.1(b)). For the calibration of the load cell, the calibration setup, similar to the mechanical model for the experiment, was used in order to consider off-axis loading from the plate; the motor, the shaft, and the plate were included in

the calibration setup. During calibration, point load was applied at $s = 0.75$ position along the plate span. The signal was amplified and low-pass filtered with 5 Hz cutoff frequency through a signal conditioner (SGA, Interface Inc.). The time series of signals was scaled and integrated over time to obtain a non-dimensional y-directional impulse acting on the plate; $I_y(t) = \int_0^t F_y(\tau)\mathrm{d}\tau / \frac{1}{2}\rho U^2 \hat{r}_2^2 ST$. S is the area of the plate, and $\hat{r}_2^2$ is the non-dimensional second moment of plate area.

5.2.3 Data analysis

A non-dimensional time variable, t, was defined as the length traveled by the tip divided by the chord length, c. A non-dimensional length variable, s, was defined as the distance from the shaft center in spanwise direction, z, divided by the distance from the shaft center to the tip of the plate, l. The variable, s, was used to express the position of the xy-sections normal to the span. Other variables such as coordinates, velocity, and vorticity were also non-dimensionalized with a proper choice of the chord length c and the mean tip velocity U; $\boldsymbol{x} = \boldsymbol{x_d}/c$, $\boldsymbol{u} = \boldsymbol{u_d}/U$, $\boldsymbol{\omega} = \boldsymbol{\omega_d} c/U$, $\Gamma = \Gamma_d/Uc$, and $\boldsymbol{\omega}$-flux $= \boldsymbol{\omega}$-flux$_d/U^2 c$, where a subscript d means a dimensional variable.

A coordinate system moves with the plate. In this moving coordinate system, the origin of the coordinate system is positioned at the point connecting the shaft and the plate (figure 5.2(b)). The y-axis is along the vertical shaft and the z-axis is parallel to the span of the plate. The vectors of the DDPIV data expressed with a laboratory frame were transformed into vector components in the direction of the x, y, and z axes. Matlab (The Mathworks Inc.) was used to obtain circulation ($\int_A \omega_z \mathrm{d}A$) and vorticity flux ($\int_A u_z \omega_z \mathrm{d}A$) at several xy-sections normal to the span of the plate. Only positive ω_z of the leading-edge vortex was included in these two terms. The threshold criteria for ω_z and u_z in circulation and vorticity flux calculation are $\omega_z > 0.1$ and $|u_z| > 0.02$.

Tecplot360 (Tecplot Inc.) was used for 3D visualization. For smooth rendering of three-dimensional iso-surfaces of vorticity, vorticity vectors were smoothed in Matlab. The new vorticity at a node was computed by $\boldsymbol{\omega}_{new} = (\boldsymbol{\omega}_{old} + \bar{\boldsymbol{\omega}}_{nb})/2$ where $\bar{\boldsymbol{\omega}}_{nb}$ is the mean of six neighbor vorticity values. This smoothing process was iterated three times.

5.3 Results and Discussion

5.3.1 Comparison between translating and rotating plates

Figure 5.3 shows the evolution of the three-dimensional vortex structure generated by the translating plate at Re = 1100. Even though several methods have been suggested to identify the vortex in an unsteady flow (e.g., Jeong & Hussain, 1995; Haller, 2005), the iso-surface of vorticity magnitude was used here to represent the vortex structures and shear layers. In this study, vorticity distribution is more important than the vortex identification itself. Thus, the iso-surface of vorticity magnitude may be more proper in describing vorticity distribution. Furthermore, the shear layer in the wake, which is important for our discussion, is difficult to identify with the methods of Jeong & Hussain (1995) and Haller (2005). For the translation case, the leading-edge vortex shows a bulge in the central region of the plate. The numerical simulation of Taira & Colonius (2009) shows similar behavior. The tip vortex on the side of the plate moves inward near the plate and becomes curved. The time history of circulation (Γ_z) of the leading-edge vortex at some xy-sections normal to the span is shown in figure 5.4(a). Γ_z becomes smaller for the xy-section as it is closer to the tip region. The effective angle of attack is reduced by a downwash effect of the tip vortex, which results in less creation of ω_z near the tip. Moreover, the positive ω_z of the leading-edge vortex near the tip tilts itself to align with the main vorticity component of the tip vortex, ω_x.

During translation, a spanwise flow develops inside the leading-edge vortex over the plate (figure 5.5(a)). This spanwise flow develops first near the center region of the plate and extends toward the tip. The presence of this spanwise flow is due to the fast deformation of the leading-edge vortex in the central region. As the leading-edge vortex deforms into a bulge, the positive ω_z component inside the leading-edge vortex is tilted into ω_x or ω_y components. This tilted vorticity induces the observed spanwise flow (figure 5.5(b)). The reverse spanwise flow from the tip to the center (blue contours in figure 5.5(a)) is also found in the downstream region of the plate. The deformed leading-edge vortex as well as the inwardly curved tip vortex can contribute to the reverse spanwise flow behind the plate near the center region. Because of the presence of the spanwise flow, the flux of ω_z inside the leading-edge vortex across the xy-section is significant even in the region close to the center (figure 5.4(b)). The vorticity flux at the xy-section near the center has a peak during

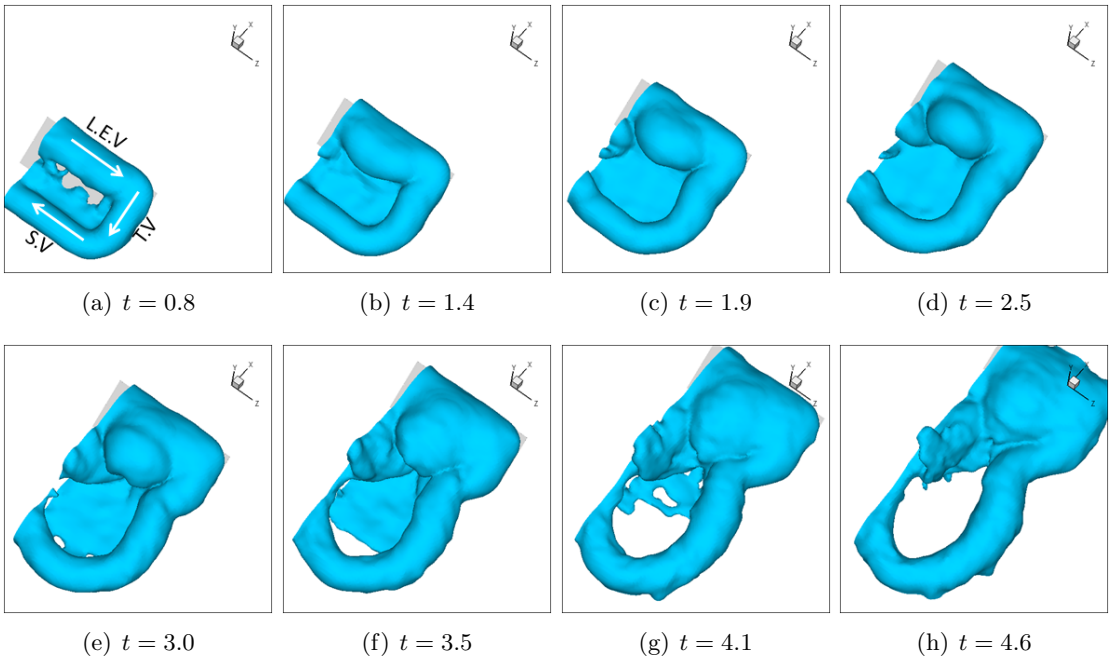

(a) $t = 0.8$ (b) $t = 1.4$ (c) $t = 1.9$ (d) $t = 2.5$

(e) $t = 3.0$ (f) $t = 3.5$ (g) $t = 4.1$ (h) $t = 4.6$

Figure 5.3: Vortex structure by a translating plate of Re = 1100 at eight frames ($t = 0.8 \sim 4.6$). The plate translates in the positive x-direction. Iso-surfaces of vorticity magnitude ($|\boldsymbol{\omega}| = 1$) are used. Leading-edge vortex (L.E.V), tip vortex (T.V) and starting vortex (S.V) are indicated at $t = 0.8$. The white arrows show the rotating direction of the vortex with the right-hand rule.

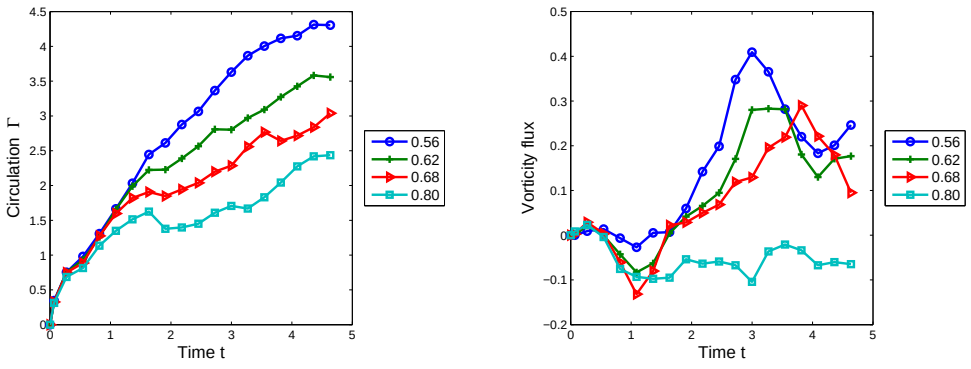

(a) (b)

Figure 5.4: Translation case: (a) circulation and (b) vorticity flux at four xy-sections normal to the z-axis ($s = 0.56 \sim 0.8$).

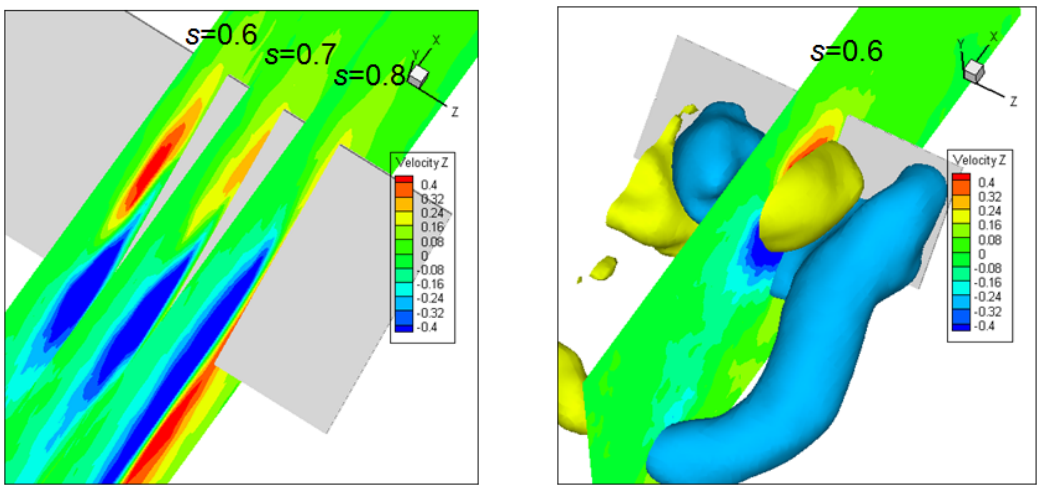

(a) (b)

Figure 5.5: Translation case: (a) contours of u_z on three xy-sections ($s = 0.6$, 0.7 and 0.8) at $t = 2.5$. (b) iso-surfaces of $\omega_x = 1.0$ (yellow) and $\omega_x = -1.0$ (blue) at $t = 2.5$. A contour of u_z on $s = 0.6$ is also plotted.

$t = 3 \sim 4$ and tends to decline afterwards.

In the rotating plate case (Re = 1100), the vortex structure is stronger near the tip than near the base (figure 5.6). More vorticity is created near the tip because the velocity of the plate is higher near the tip. Unlike the tip vortex of the translation case, the tip vortex of the rotating plate does not move inward. The lack of inward motion may be due to the presence of a strong spanwise flow in the positive z-direction (figure 5.7). One of the main differences in the flow field between these two cases in terms of flow structure is the vorticity distribution of a wake region (figure 5.8). For the translating plate case, the distribution of strong ω_x is confined to the counter-rotating tip vortices on both sides. On the other hand, in the rotating plate case, positive ω_x is widely distributed in the shear layer of the wake. This shear layer is shed from the trailing edge of the plate.

One notable source of positive ω_x in the shear layer of the wake is the rotation of the plate itself. As the plate rotates, the positive ω_x component of vorticity is created on the bottom surface of the plate. This positive ω_x sheds from the trailing edge and makes up the wake vorticity field. In addition, the spanwise flow from the base to the tip can induce the positive ω_x generation on the top surface of the plate because of the no-slip condition. However, we speculate that most of the positive ω_x generated by the spanwise flow on the top surface will not shed into the wake because it would be entrapped by the leading edge

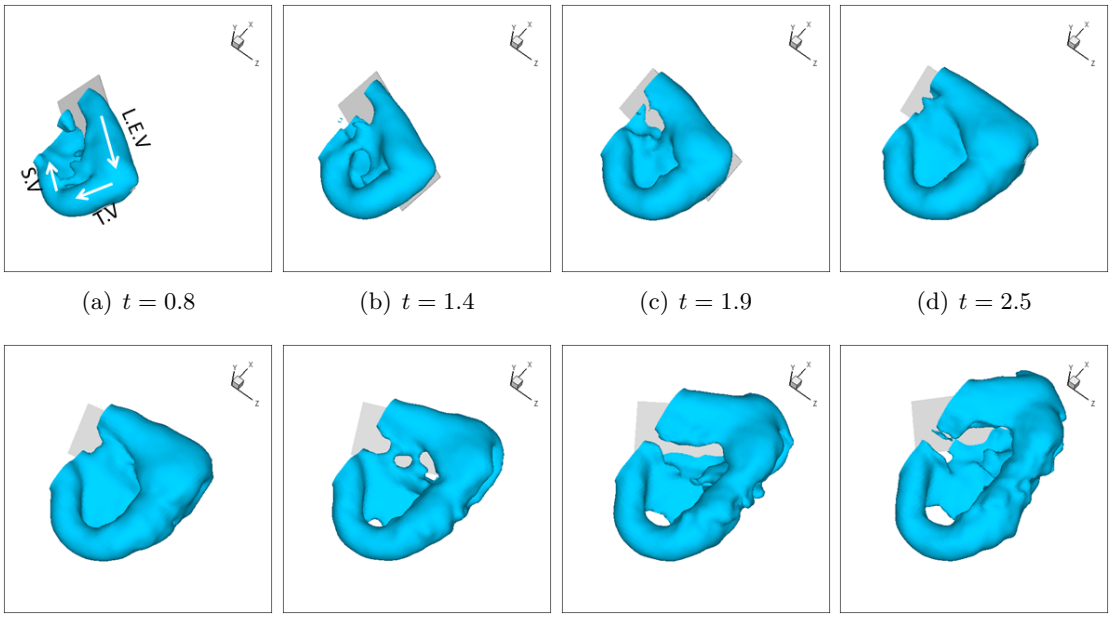

(a) $t = 0.8$ (b) $t = 1.4$ (c) $t = 1.9$ (d) $t = 2.5$

(e) $t = 3.0$ (f) $t = 3.5$ (g) $t = 4.1$ (h) $t = 4.6$

Figure 5.6: Vortex structure by a rotating plate of Re = 1100 at eight frames ($t = 0.8 \sim 4.6$). The plate rotates with respect to the positive y-axis. Iso-surfaces of vorticity magnitude ($|\boldsymbol{\omega}| = 1$) are used. Leading-edge vortex (L.E.V), tip vortex (T.V) and starting vortex (S.V) are indicated at $t = 0.8$. The white arrows show the rotating direction of the vortex with the right-hand rule.

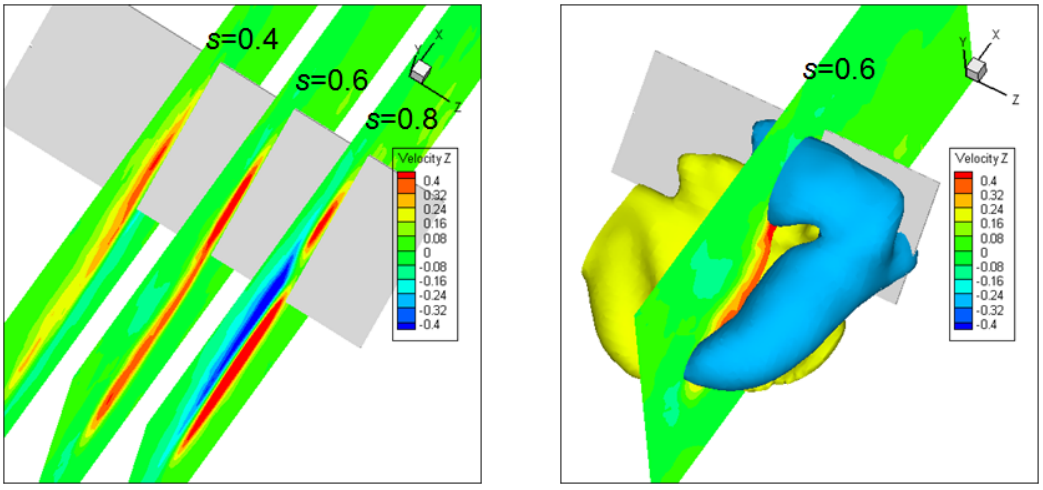

(a) (b)

Figure 5.7: Rotation case: (a) contours of u_z on three xy-sections ($s = 0.4$, 0.6, and 0.8) at $t = 2.5$. (b) iso-surfaces of $\omega_x = 1.0$ (yellow) and $\omega_x = -1.0$ (blue) at $t = 2.5$. A contour of u_z on $s = 0.6$ is also plotted.

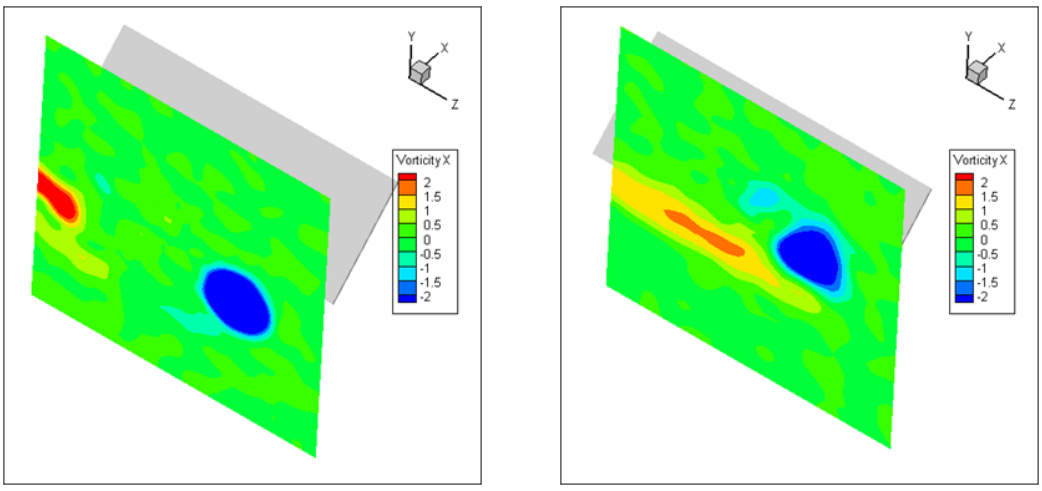

(a) (b)

Figure 5.8: Contours of ω_x for (a) the translation case on the yz-section at $x = -1.0$ and (b) the rotation case on the yz-section at $x = -0.5$. Both cases are at $t = 2.5$.

vortex. The existence of positive ω_x in the wake of the rotating plate is also explained by an invariance property of vorticity; the volume integral of vorticity over the whole flow field is always constant for a flow field at rest at infinity (Wu *et al.*, 2006). According to this property, if the vorticity is created in the flow field, the vorticity of the opposite sign and equal strength should be created to balance it. The vorticity created at the bottom surface of the rotating plate has positive ω_x as opposed to negative ω_x at the tip vortex.

In the wake region behind the plate, the positive ω_x of the shear layer shed from the trailing edge contributes to a spanwise flow. Moreover, when the plate rotates, the starting vortex is no longer parallel to the span of the plate. Therefore, the starting vortex induces the spanwise flow. In the wake, the spanwise flow is also found in an area between the tip vortex and the shear layer shed from the trailing edge. The interaction of these two flow structures with opposite ω_x components induces the stronger spanwise flow between them (figure 5.7).

There is also a negative ω_x region along the span of the plate in addition to the tip region (figure 5.7(b)). This negative ω_x is from the tilting of positive ω_z inside the leading-edge vortex. In the translation case, we mentioned the tilting process in order to explain the entrainment of positive ω_z into the tip vortex and the bulging of the leading-edge vortex. For the rotation case, vorticity tilting inside the leading-edge vortex is essentially caused by the

variation of the leading-edge vortex strength along the span. To clarify this point, consider that the size of the leading-edge vortex at the xy-section gets larger and its core moves away from the leading edge. For this reason, the leading-edge vortex in the outer region (nearer to the tip) of the rotating plate is tilted backward (i.e., its core is shifted farther away from the leading edge) with respect to that of the leading-edge vortex in the inner region, which has a core closer to the leading edge of the plate due to slower growth. This tilting mechanism changes some of positive ω_z in the leading-edge vortex to negative ω_x. Since the flow induced by this negative ω_x region over the plate is close to the plate, the plate blocks the downward component of the flow and changes the flow to the direction parallel to the span near the plate surface; i.e., an image vortex inside the plate changes the flow field induced by a real vortex. As a result, the spanwise flow over the plate is strengthened by the presence of the plate. Consequently, vorticity transport by this spanwise flow contributes to stabilizing the leading-edge vortex. From the vorticity distribution over the plate and in the wake, it is confirmed that a spanwise flow is not only confined inside the leading-edge vortex core, but is also widely distributed in the downstream region of the plate. The circulation and vorticity flux on several xy-sections of the rotation case are explained in the following section.

5.3.2 Effect of viscosity and velocity program on vortex formation

We examined the effect of viscosity while keeping all other parameters same. For a given plate rotation, vorticity distribution by diffusion makes the vortex structure of Re = 60 quite different from that of Re = 8800. In figure 5.9, the iso-surface of the vorticity magnitude for the Re = 60 case does not show a starting vortex as distinctly as that of Re = 8800. Moreover, tip and leading-edge vortices are more widely distributed for the Re = 60 case. Also note that the vortex structure (non-dimensional vorticity distribution) of Re = 1100 in the previous section (figure 5.6) is quite similar to that of Re = 8800. For the low Reynolds number case (Re = 60), the negative ω_x component of vorticity tilted inside the leading-edge vortex is distributed throughout a larger area over the plate (figure 5.10). Due to this broadly distributed ω_x, a spanwise flow is strong over the rear area of the plate.

For a given vorticity field, the force acting on a body in an infinite flow field at rest at

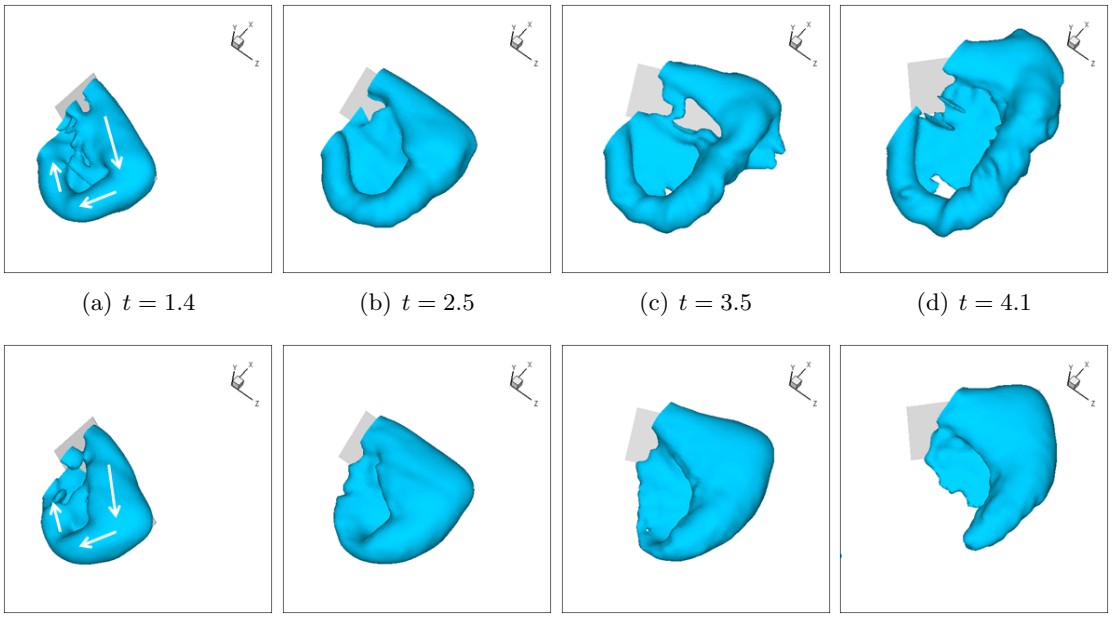

(a) $t = 1.4$ (b) $t = 2.5$ (c) $t = 3.5$ (d) $t = 4.1$

(e) $t = 1.4$ (f) $t = 2.5$ (g) $t = 3.5$ (h) $t = 4.1$

Figure 5.9: Upper line: Vortex structure by a rotating plate of Re = 8800 at four frames ($t = 1.4 \sim 4.6$). Lower line: Vortex structure by a rotating plate of Re = 60 at four frames ($t = 1.4 \sim 4.6$). Iso-surfaces of vorticity magnitude ($|\boldsymbol{\omega}| = 1$) are used. The plates are rotated with the trapezoidal velocity program. The white arrows show the rotating direction of the vortex with the right-hand rule.

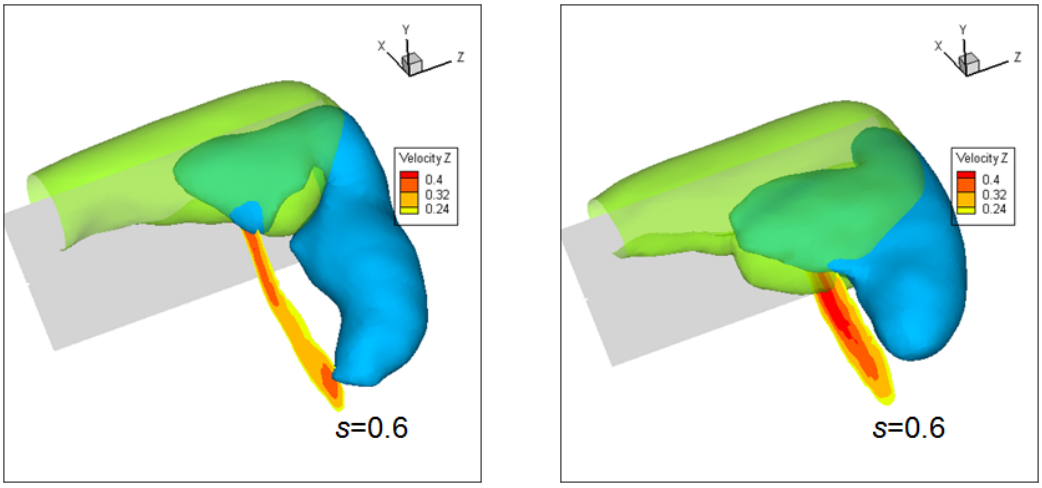

(a) (b)

Figure 5.10: Iso-surfaces of $\omega_z = 0.8$ (transparent green) and $\omega_x = -0.8$ (blue) in (a) Re = 8800 and (b) Re = 60 cases at $t = 2.5$. A contour of u_z is plotted on the xy-plane at $s = 0.6$. On the contour, u_z less than 0.2 is blanked.

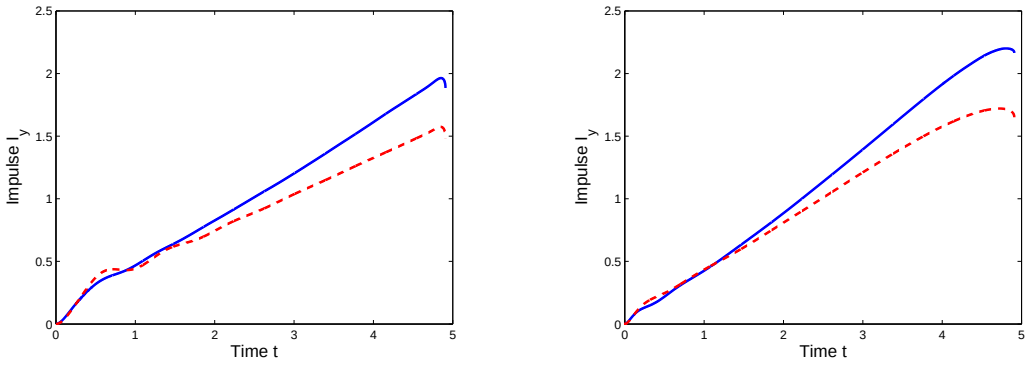

(a) (b)

Figure 5.11: Y-component of impulse (I_y) from load cell measurement for (a) trapezoidal velocity program and (b) sinusoidal velocity program cases. Continuous lines are for the Re = 8800 case, and dashed lines are for the Re = 60 case.

infinity can be obtained by using the following vorticity moment theory (Wu, 1981).

$$\boldsymbol{F} = -\frac{\rho}{2}\frac{\mathrm{d}}{\mathrm{d}t}\int_{V_\infty} \boldsymbol{x} \times \boldsymbol{\omega} \mathrm{d}V + \rho \frac{\mathrm{d}}{\mathrm{d}t}\int_{V_b} \boldsymbol{u} \mathrm{d}V, \tag{5.1}$$

where V_∞ is an infinite fluid domain including the body, V_b is body volume, and ρ is fluid density. The variables in Eq. 5.1 are dimensional and expressed in a global coordinate system instead of the moving coordinate system used in this study. The force acting on a body can be obtained from the temporal change of vorticity distribution inside the flow field (first term) and the temporal change of the body velocity (second term). In an unbounded flow, the integrand of the first term on the right-hand side is invariant for any vorticity field, regardless of viscous diffusion, unless non-conservative body forces are imposed (Wu *et al.*, 2006). However, if the body inside the flow field moves, the motion of the body creates vorticity, and changes vorticity distribution of the flow field over time (and, thus, the first term in Eq. 5.1).

According to Birch *et al.* (2004), Lentink (2008), and our result of force measurement using a load cell (figure 5.11), as the Reynolds number becomes smaller, less lift force is generated under the same kinematic conditions. From these results, it is clear that viscosity affects the first term of the above equation by changing vorticity distribution of the flow field. First, it is reasonable to think that viscosity influences the vorticity creation on the surface of the body. Less vorticity is generally created in a lower Reynolds number flow

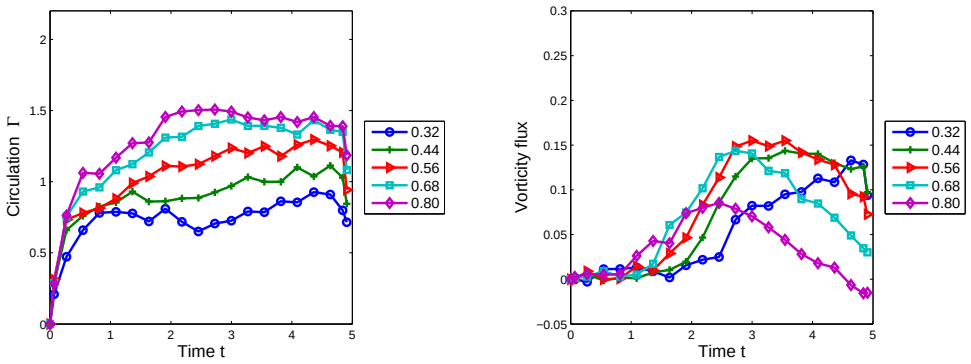

(a) (b)

Figure 5.12: Rotation case of the Re = 60 and trapezoidal velocity program: (a) circulation and (b) vorticity flux at five xy-sections ($s = 0.32 \sim 0.80$).

even though it is not easy to quantify, especially in 3D cases. More importantly, if the Reynolds number becomes smaller, the vorticity of the leading-edge vortex diffuses more away from the plate. The velocity field near the moving plate can be expressed as the sum of a vorticity-induced velocity field and a velocity field of the potential flow generated by the plate motion (Batchelor, 1967). The effect of the potential flow on the velocity field decreases as the distance from the plate is larger. Thus, the fluid elements with vorticity diffused away from the plate do not obtain plate-induced potential velocity large enough to follow the rotating plate, whereas the fluid elements close to the plate keep following the rotating plate. For this reason, if the origin of the coordinate system used in Eq. 5.1 is on the shaft center, the vorticity moment (integrand of the first term in Eq. 5.1) becomes smaller compared to a high Reynolds number case. Figure 5.10 demonstrates how the lagging forward motion of vorticity due to viscous diffusion changes the distribution of vorticity inside the leading-edge and tip vortices. In the Re = 60 case, positive ω_z and negative ω_x are distributed more widely inside the area swept by the rotating plate.

Circulation and flux of ω_z in the leading-edge vortex across several xy-sections normal to the span of the plate are plotted in figure 5.12 for the Re = 60 and trapezoidal velocity program case. As Poelma *et al.* (2006) and Babinsky & Jones (2009) noted, the circulation increases significantly by sudden acceleration and stays without notable increase after acceleration. Vorticity generated by the leading edge is tilted or convected toward a tip by a spanwise flow, which inhibits circulation from growing. The flux increases generally

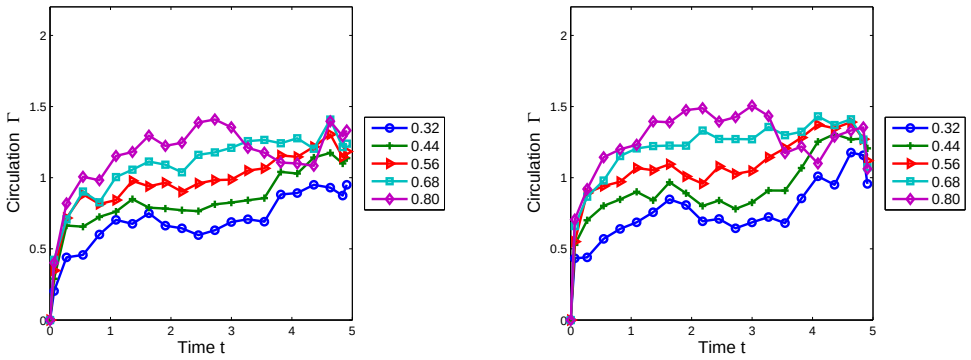

Figure 5.13: Rotation cases of the trapezoidal velocity program, (a) Re = 8800 and (b) Re = 1100. Circulation at five xy-sections ($s = 0.32 \sim 0.80$) is plotted.

as a xy-section moves from the base to the tip between $s = 0.32 \sim 0.56$. The positive z-directional gradient of flux indicates that positive ω_z convects toward the tip. However, in the other region ($s = 0.56 \sim 0.80$), the z-directional gradient of flux is rather negative in the second half of the rotation. Nevertheless, circulation in this region does not grow significantly because the tilting of ω_z into other vorticity components is dominant. According to Eq. 5.1, the transport of vorticity created at the leading edge toward the tip has a positive effect on lift force generation because it increases a vorticity moment.

For the Re = 8800 case, the circulation curves are very similar to those of the Re = 1100 case of 5.3.1 (figure 5.13). As is the Re = 60 case, circulation grows suddenly during impulsive starting of the plate, and then its growth is retarded after acceleration; the trend of circulation curves for the Re = 8800 is not significantly different from the Re = 60 case except for the $s = 0.80$ curve. The section $s = 0.80$ of the Re = 8800 case is close to the tip vortex. Thus, the notable decrease in circulation for the $s = 80$ curve during the second half of the rotation may be due to significant vorticity transport into the tip vortex by tilting. For the high Reynolds number cases (e.g., Re = 8800 and 1100 in our study), the high spanwise velocity region over the plate is close to the surface (Aono *et al.*, 2008). Therefore, when the velocity vectors were fitted into cubic grids and velocity vectors were smoothed during the DDPIV data process, high spanwise velocity on the top surface might not be captured with good accuracy. For this reason, calculation of ω_z flux at xy-sections is not considered in the Re = 8800 and 1100 cases. To solve this problem, a mapped flow

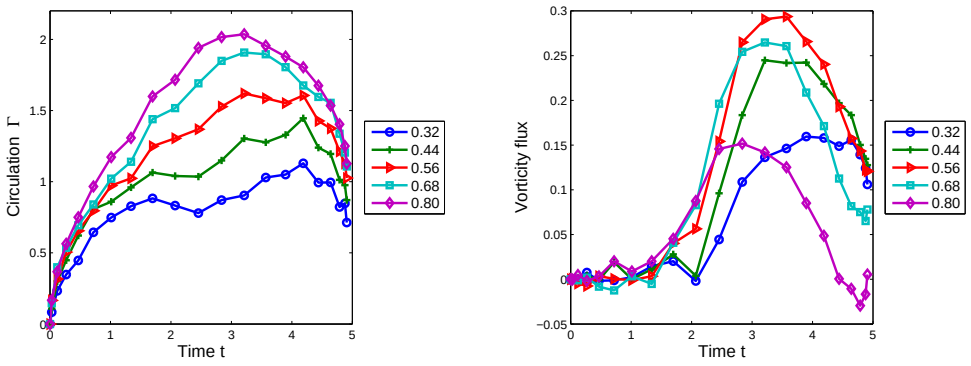

(a) (b)

Figure 5.14: Rotation case of the Re = 60 and sinusoidal velocity program: (a) circulation and (b) vorticity flux at five xy-sections ($s = 0.32 \sim 0.80$).

field should be confined in a near-field around the plate, or finer spatial resolution should be used.

In order to see how the velocity program influences the vorticity distribution of the leading-edge vortex, circulation and flux of sinusoidal and trapezoidal velocity programs are compared for the Re = 60 case (figures 5.12 and 5.14). At the initial stage, the trapezoidal velocity program case develops a vortex structure faster due to impulsive acceleration of the plate. Note that the circulation slope is steeper at the early stages and tends to level out after $t = 1$. Meanwhile, in the first half of the sinusoidal velocity program case, the vortex strength continues to grow, especially for higher s curves, because of the increasing velocity of the plate. In this case, during the first half, the production rate of ω_z exceeds the drainage rate of ω_z by out-of-plane vorticity transport, convection, or tilting. However, during the second half when the plate decelerates, the out-of-plane transport of ω_z exceeds the generation of ω_z, which results in negative slopes for circulation. Correspondingly, the flux of ω_z starts to increase steeply in the middle of rotation (figure 5.14(b)). Even though the trends of circulation curves are considerably different between these two velocity program cases, the circulation values of both cases are quite similar when the plate stops ($t = 4.9$).

5.4 Concluding remarks

The flow fields generated by two kinematics of a plate were studied using the DDPIV technique. This mapping technique offers a great opportunity to investigate three-dimensional flow fields. Here, the formation process of the whole vortex structure by translating and rotating plates was presented. In addition, the effect of vorticity transport by convection, tilting, and diffusion on vortex formation and force generation was investigated.

For a small aspect-ratio plate in the translation mode, owing to the influence of a tip, a leading-edge vortex develops non-uniformly along the span. The deformed leading-edge vortex induces the spanwise flow over the plate and subsequent vorticity transport. This vorticity transport starts near the central region of the plate. However, the spanwise flow is not strong enough to suppress the growth of the leading-edge vortex near the central region of the plate. For the rotation mode, the vorticity of the leading-edge vortex is tilted because the size of the leading-edge vortex increases from the base to the tip. The tilted vorticity induces the spanwise flow over the rotating plate. Contrary to the translation mode, the spanwise flow is also found in the wake. The spanwise flow in the wake is due to the streamwise component of vorticity, which is distributed inside a shear layer and a starting vortex in the wake. Aono *et al.* (2008) used a pressure field near a rotating model to explain the mechanism of a spanwise flow over the plate. As the circulation of a vortex is larger, the pressure inside the vortex is lower. The increasing strength of the leading-edge vortex from the base toward the tip creates a pressure gradient along the span. Thus, a fluid over the plate accelerates toward the tip because of the pressure gradient. It is necessary to study in detail how two different approaches, the pressure gradient and vorticity tilting, are related to the development of the spanwise flow.

As the Reynolds number decreases, viscous diffusion of vorticity becomes a more important factor in affecting flow structure and force generation. In the low Reynolds number case, the forward motion of the leading-edge vortex is retarded. Thus, the vorticity of the leading-edge and tip vortices tends to spread into the inner area enclosed by the whole vortex structure. Because of this change in vorticity distribution, the lift force becomes smaller than that of the high Reynolds number case.

Chapter 6

Dynamics of corner vortices

6.1 Background

Vortex formation by objects starting from rest has been studied extensively in the past. The roll-up process of starting vortex sheets has been used to explain lift generation by starting airfoils (Prandtl & Tietjens, 1934). The starting vortex formation of various two-dimensional models has also been studied (e.g., Pullin, 1978; Pullin & Perry, 1980; Saffman, 1995; Lugt, 1996). While two-dimensional or axisymmetrical starting vortices have been studied intensively, experimental studies of three-dimensional starting vortices are sparse (von Ellenrieder *et al.*, 2003; Buchholz & Smits, 2006). In particular, the vortex formation in the corner region where the flow is highly three-dimensional has been rarely studied experimentally. We studied vortex formation in the corner region of impulsively translating thin plates with a 90° angle of attack by using a three-dimensional flow mapping technique. Three corner-angle cases (60°, 90° and 120°) were investigated in order to understand the effect of the corner angle on the dynamics of the vortices created near corners.

6.2 Experimental setup

In order to map three-dimensional fields near the corner, defocusing digital particle image velocimetry (DDPIV) was used (Willert & Gharib, 1992; Pereira & Gharib, 2002; Pereira *et al.*, 2006). A DDPIV camera was placed in front of a tank ($870 \times 430 \times 360$ mm^3). The tank was filled with water and seeded with 100 μm silver-coated particles. The positions of a model and camera probe volume are shown in figure 6.1. An acrylic plate with thickness 1.46 mm was immersed vertically so that a corner region is included in the DDPIV camera

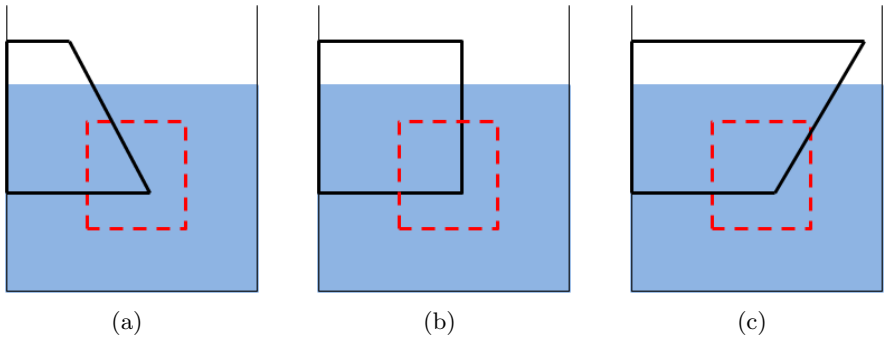

Figure 6.1: Positions of the plate model and the camera probe volume inside the tank for (a) 60° corner-angle, (b) 90° corner-angle, and (c) 120° corner-angle cases. In this figure, the plate moves into the page, and the camera is placed on the right side of the tank. Thick continuous lines indicate the plate model. Thick dashed lines are the volume in which the flow field is mapped.

probe volume. Three plates with different corner angles (60°, 90°, and 120°) were used. In the 90° angle case, the area immersed in water has height 160 mm and width 200 mm. The position of the corner vertex in the mapping volume is the same for three different corner-angle cases. The vertical edge on the other side of the plate was closely aligned with the tank wall to avoid water leakage through the gap. Even though we used plates with finite length, ideally there should be no characteristic length so that the vortex formation processes are dependent only on corner shapes. Plates accelerated for 1 sec at the start, and translated with a constant velocity of 20 mm/sec. The Reynolds number based on the constant velocity and the height of immersed plates is 3200. The images taken with 5 image pairs/sec were processed using the DDPIV software to get velocity and vorticity field data. To get a velocity field, a relaxation method of 3D particle tracking was used (Pereira *et al.*, 2006). Then, vorticity fields were obtained from the velocity field data. Because of the limitation of the camera volume size, only the flow near a corner region was mapped. Two sets of the experiment were performed by translating the initial position of the model 120 mm parallel to the tank wall. The total fluid volume mapped by two sets of the experiment was $280 \times 140 \times 140$ mm^3. The mapped flow volume is long in the plate moving direction.

6.3 Results and Discussion

Figures 6.2−6.4 show the vortex formation process near the corner of the plate with a different corner angle (60°, 90°, and 120°). In these figures, iso-surfaces of vorticity magnitude were used to represent vortex structures. A relatively high vorticity magnitude was chosen to show the vortex core clearly. At the start, the vortex sheet rolls up along the plate edge. Therefore, the shape of the vortex is similar to the shape of the plate edge. However, as the plate moves farther, the vortex core begins to separate non-uniformly from the edge and finally lose its initial shape. After the vortex core separates from the edge, newly-created vortex sheets continue to roll up around the deformed vortex core. Here, the term *vortex separation* is used to indicate that a vortex core does not follow the plate edge and retards its forward motion. Note that its definition is subjective. We use this term mainly for the purpose of comparing vortex positions relative to the plate edge.

As can be seen in (a)−(c) of figures 6.2−6.4, the corner angle affects the morphology of the corner vortex. As the corner angle is small (60°), the vortex close to the corner follows the forward motion of the plate without noticeable separation from the edge. Meanwhile, the vortex far from the corner separates from the corner early. This trend is weakened as the corner angle gets larger. For the 120° case, the corner vortex tends to separate from the corner earlier than that of the lower angle cases. Its x-directional position is quite uniform along the edge. If there is a thin vortex tube in a flow field without a moving object, the vortex tube can change its position by its self-induction. As the curvature of the thin vortex tube gets bigger, the vortex tube has the larger self-induced velocity component in the direction bi-normal to the curved vortex tube (Batchelor, 1967). This theoretical finding may be used in explaining the dependence of the vortex forward motion on the corner angle. As the corner angle gets smaller, the curvature of the corner vortex becomes larger, and the larger displacement of the vortex is anticipated in the direction bi-normal to the plate edge (x-direction in our model).

It is well known that, in the absence of a moving object, the velocity field in the fluid domain can be obtained from the vorticity induction equation. This approach makes it easier to explain self-induction of a vortex or mutual interaction with other vortices. However, in the case of a vortex near a moving body in an infinite field, the potential flow effect caused by a moving body should be taken into consideration as well because the velocity field

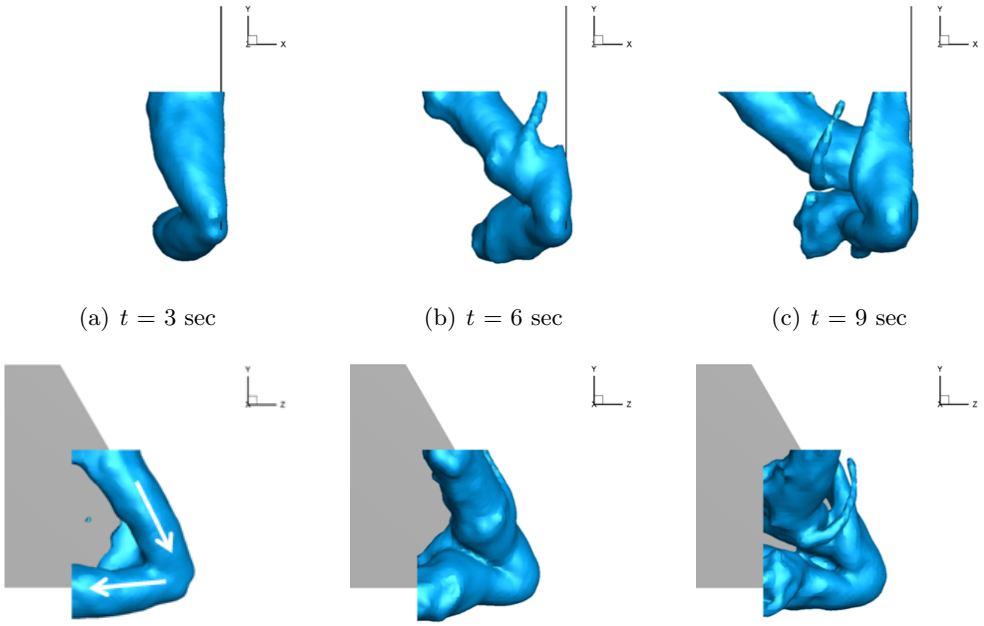

(a) $t = 3$ sec (b) $t = 6$ sec (c) $t = 9$ sec

(d) $t = 3$ sec (e) $t = 6$ sec (f) $t = 9$ sec

Figure 6.2: Vortex formation process at the corner of the 60° corner-angle plate. (a)−(c) are in side view from the $+z$ axis, and (d)−(f) are in back view from the $-x$ axis. Iso-surfaces of vorticity magnitude ($|\boldsymbol{\omega}| = 1.7$/sec) are used. The white arrows show the rotating direction of the vortex with the right-hand rule.

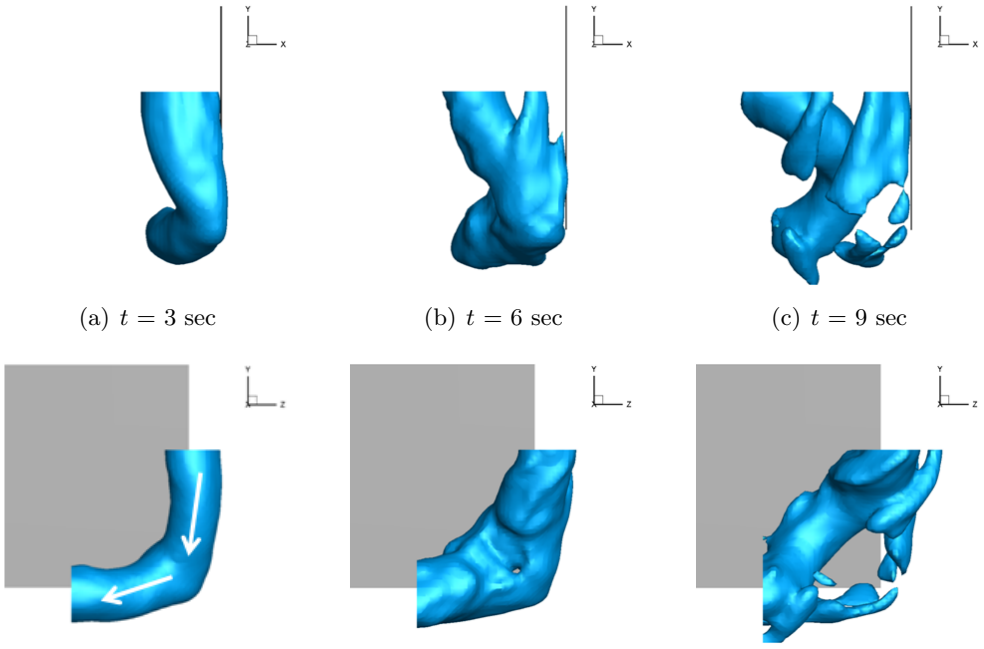

(a) $t = 3$ sec (b) $t = 6$ sec (c) $t = 9$ sec

(d) $t = 3$ sec (e) $t = 6$ sec (f) $t = 9$ sec

Figure 6.3: Vortex formation process at the corner of the 90° corner-angle plate. (a)−(c) are in side view from the $+z$ axis, and (d)−(f) are in back view from the $-x$ axis. Iso-surfaces of vorticity magnitude ($|\boldsymbol{\omega}| = 1.7$/sec) are used. The white arrows show the rotating direction of the vortex with the right-hand rule.

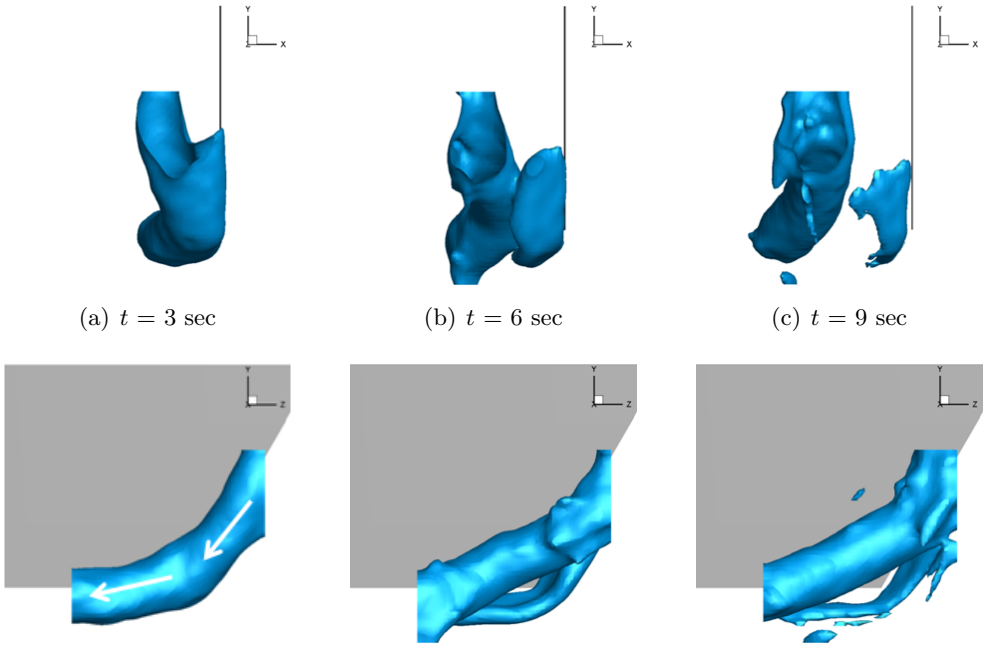

(a) $t = 3$ sec (b) $t = 6$ sec (c) $t = 9$ sec

(d) $t = 3$ sec (e) $t = 6$ sec (f) $t = 9$ sec

Figure 6.4: Vortex formation process at the corner of the 120° corner-angle plate. (a)−(c) are in side view from the $+z$ axis, and (d)−(f) are in back view from the $-x$ axis. Isosurfaces of vorticity magnitude ($|\boldsymbol{\omega}| = 1.7$/sec) are used. The white arrows show the rotating direction of the vortex with the right-hand rule.

must be constructed from both vorticity distribution and potential flow effect by the plate motion (Batchelor, 1967). Thus, self-induction of the vortex is not enough to explain the morpho-dynamics of the vortex generated by the plate. For example, when the plate just starts to translate, the starting vortex follows the plate motion in spite of its small strength. However, the vortex gradually separates from the plate even though its strength becomes larger as the plate continues to translate. To fully understand the vortex motion behind the plate, the effect of the plate motion should be considered. While the plate translates, fluids close to the back of the plate are under strong potential flow effect enough to follow the plate motion. As the distance between a fluid particle and the plate becomes larger, the induction effect by the plate becomes smaller. For this reason, it is difficult for the vortex, which is far from the plate, to catch up with the plate motion.

As well as the forward motion of the corner vortex, the inward motion of the corner vortex is also different among the three corner-angle cases studied here ((d)−(f) of figures 6.2−6.4). As the plate starts to translate, a low pressure region is generated behind the plate and an inward flow (the flow from the outside toward the backside of the plate) is induced behind the plate. Due to the low pressure zone behind the plate, the corner vortex moves inward gradually. Since the corner vortex of the 90° case is closer to the plate in the x-direction, it is influenced by pressure suction more than that of the 120° case, and its inward motion is more distinct. In the 60° corner-angle case, two edges are in a short distance from each other. Vorticity near the corner, which is transported by the inward flow, is eventually entrained by vortices away from the corner in both edges. For this reason, the corner vortex of the 60° case does not develop as well as that of the other two cases.

6.4 Concluding remarks

The three-dimensional flow condition near the corner reveals interesting features of vortex dynamics. Here, it was shown that the dynamics of the growing corner vortex was strongly dependent on the shape of the corner. This study was motivated by various shapes of low aspect-ratio flapping propulsors in nature. In order to understand the morphology of animal propulsors from the viewpoint of locomotive efficiency, it may be necessary to investigate how the edge shapes of propulsors affect vortex formation and consequent thrust performance.

Chapter 7

Summary and Future work

The three-dimensional vortex formation process was studied with plate models simulating some motions of flapping propulsors. The translating motion of the plate was also considered to investigate flexibility effect and corner-vortex dynamics.

By analyzing vortex formation and its relation to force generation, some characteristics of unsteady fluid physics for flapping propulsors were explored. Spanwise flow delays the shedding of a leading-edge vortex in rotating motion mimicking insect hovering, but it induces a tip vortex to separate from the plate in paddling motion. Both effects of spanwise flow are positive in generating propulsive force. The interaction of spanwise flow with a vortex structure is also important in explaining the dependence of vortex formation on plate flexibility, plate shape, and the Reynolds number. Flexible propulsors can smooth out the excessive peak of force acting on them without sacrificing thrust performance, which is also good in reducing the danger of fatigue and fracture and stabilizing the body motion. In the clapping motion of double plates and the simple flapping motion of a single plate, thrust performance is inversely related to aspect ratio. In these motions, low aspect-ratio propulsors are more effective in generating thrust. This result offers information to better understand the benefit of low aspect-ratio wings in force generation under specific locomotion modes. Vortex formation near the corner is strongly influenced by the corner shape. While the corner vortex separates early from the plate edge for the high corner-angle case, it can follow the plate motion for the low corner-angle case.

In this thesis work, the mechanical model was fixed to the tank, and the motion of the model was simple; only one stroke was simulated in quiescent fluid. In conducting future work, it is necessary to consider repeated flapping motion of a propulsor and study how the vortex structure can be changed, compared to that of the first stroke in quiescent

fluid. In repeated motion of power and recovery strokes, the flow structure generated by the previous stroke can affect the flow structure and propulsive performance in the current stroke. For example, Dickinson *et al.* (1999) claimed that, when fruit flies hovered, they took advantage of the wake created by the previous stroke to enhance the lift. In addition to repeated strokes, it is also necessary to consider the body motion instead of using the fixed body model. For this reason, as a continuation of Ch. 4 work, it is important to investigate how advance ratio affects the relation between aspect ratio and force generation for repeatedly flapping models. The advance ratio is defined as the forward body speed divided by the mean speed of the flapping wing. In gliding of flying animals, the advance ratio is infinite, and high aspect-ratio wings are preferred in lift generation. Meanwhile, in hovering with a vertical stroke plane, the advance ratio is zero, and low aspect-ratio wings are preferred in lift generation according to Ch. 4. Thus, it is reasonable to think that there should be an optimal aspect ratio for a given advance ratio. The advance ratio frequently used by a flying animal may be one of the most important factors in optimizing the aspect ratio.

Also, the flight mechanisms of live butterflies are to be explored in order to improve the characteristics studied in the thesis work. In fact, many parts of my thesis work were motivated by butterfly flight. They have many features that I have been interested in. During strokes, their wings deform severely. The wing aspect ratio is small even compared to that of other insects. Under some circumstances, they use a peculiar flapping motion, clap and fling. Quantitative observation of the flight patterns of live butterflies and flow structure analysis through a scaled mechanical model mimicking them will be helpful in establishing the principles of unsteady aerodynamics for butterflies.

Appendix A

Scaling of hydrodynamic force by length in 2D translating plates

To supplement the work in Ch. 4, a two-dimensional computational study was performed. The vortex particle method with fluid-body coupling was used (Eldredge, 2007, 2008). The flow field was assumed to be two-dimensional, and the plate translated in one direction, the negative x-axis. The angle of attack of the plate was 90°, and the shape of the plate was elliptical with the major axis on the y-axis. Three plates with different sizes were used; the lengths of the plates along the major axis h were 1, 2, and 3. However, the length along the minor axis w was constant, $w = 0.1$ (figure A.1(a)).

Here, we investigate how vortex strength and hydrodynamic force are scaled by a vertical length h. Three plates move with the same kinematics. Two fundamental kinematic conditions are imposed. In the first case, the plate impulsively accelerates for $\Delta t = 0.1$ and then translates with a constant velocity $u_x = -1$. In the second case, the plate's velocity is sinusoidal until $t_f = 5$; $u_x = \cos(2\pi t/t_f) - 1$, and the plate does not move anymore after $t_f = 5$ (figure A.1(b)). The Reynolds numbers based on the characteristic velocity $U = 1$ and length h are 100, 200, and 300 for three plates.

First, the constant velocity program case is investigated. Theoretically, it is known that the added-mass force during impulsive starting is proportional to the square of the length scale for the two-dimensional thin plate model with a 90° angle of attack; $F \propto h^2$. Also, the quasi-steady force, the force averaged over a long time, is nearly proportional to the length scale for the two-dimensional thin plate model; $F \propto h$. In our case, the Reynolds number is from 100 to 300, and thus the quasi-steady force coefficients may be a little different from one another. However, the effect of the Reynolds number on the quasi-steady force

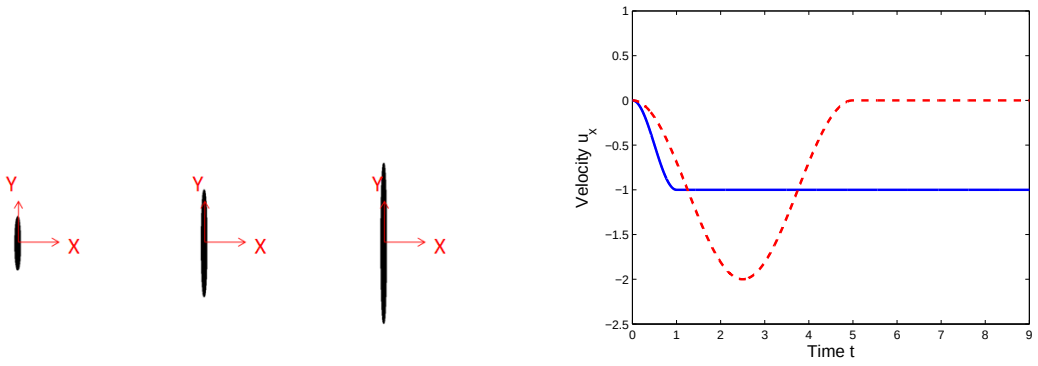

(a) (b)

Figure A.1: (a) Three elliptical plates with different vertical lengths h. (b) Two velocity programs. The continuous line represents the constant velocity program and the dashed line represents the sinusoidal velocity program.

coefficient is not a major part of the discussion. Instead, I will focus on the scaling effect of the plate length on the force history. From two scaling relations, there should be a transient phase where the scaling relation of the force and length is changed from $F \propto h^2$ to $F \propto h$.

For the constant velocity program, force coefficients C_F $(= F_x/\frac{1}{2}\rho U^2 h$, actually drag coefficients), are shown in figure A.2(a). During the acceleration phase, there is a significant difference among force coefficients of the three models as expected. However, this difference becomes smaller as the plates continue to translate, and finally the quasi-steady force condition is attained. During the transient phase, the force that can be exerted by the plate is not proportional to the size (or volume) of the thin plate. For example, by increasing the length twice, the force acting on the model increases more than double during the transient phase. The scaling of the force by the length in the transient phase is important in the mechanical study of flapping propulsion since the displacement of the flapper is limited during each stroke. For details about the optimal stroke of two-dimensional flapping, see Milano & Gharib (2005).

During the acceleration phase, the slope of the circulation, $\dot{\Gamma}$, is quite different for the three cases (figure A.2(b)). Because of the symmetric condition with respect to $y = 0$, only positive ω in the negative y-region is considered in the Γ calculation. The slopes of three cases become similar as time goes on. The vortex of the longer plate has more circulation at the same plate displacement. This trend was also found in three-dimensional clapping models of Ch. 4.

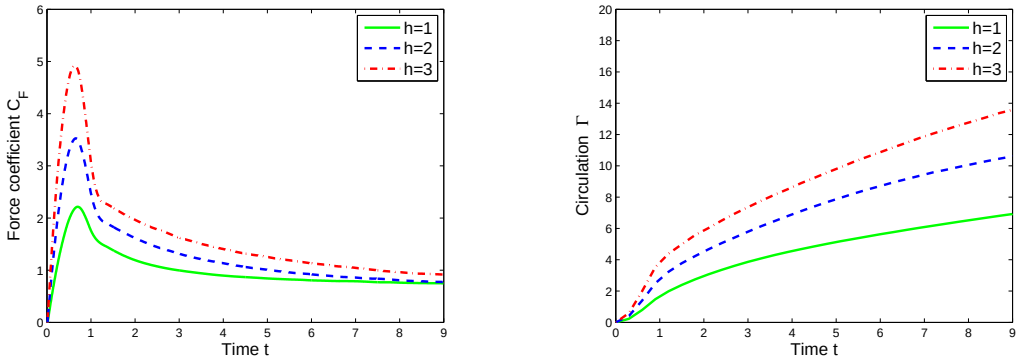

(a) (b)

Figure A.2: Time history of (a) force coefficients and (b) circulations for three plate models in the constant velocity program.

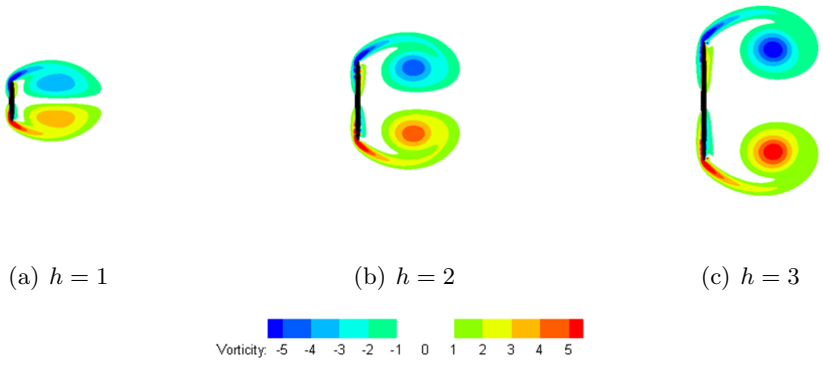

(a) $h = 1$ (b) $h = 2$ (c) $h = 3$

Figure A.3: Vorticity distribution for the constant velocity program at $t = 4.8$.

In the case of the sinusoidal velocity program, the force coefficient C_F ($= F_x/\frac{1}{2}\rho U^2 h$) is larger for the longer plate during the acceleration phase ($t = 0 \sim 2.5$), similar to the case of the constant velocity program. During the deceleration phase and after the stop, C_F becomes negative. In the lowest peak of the force, the absolute magnitude of C_F is larger for the longer plate (figure A.4(a)). Nevertheless, total impulse or averaged force is still higher for the longer plate. It is notable that the force graph is not anti-symmetric with respect to $t = 2.5$ for acceleration and deceleration. Moreover, the times of plate acceleration and deceleration do not coincide exactly with the times of positive and negative force generation; e.g., the force is positive during the early deceleration phase.

During deceleration, the stopping vortex develops, which has vorticity opposite that of the starting vortex in the same y-direction (figure A.5). The formation of the stopping vortex is related to the negative force production. During the deceleration phase, the circulation of the starting vortex does not continue to grow. Rather, the circulation decreases after $t = 3.5$ in spite of the positive velocity of the plate (figure A.4(b)). The decrease of the starting vortex circulation is due to interaction with the stopping vortex of opposite vorticity. Since the core of the starting vortex in the $h = 1$ case is closer to the plate than the $h = 3$ case, the amount of circulation decrease is also larger in the $h = 1$ case because of the proximity of two counter-rotating starting and stopping vortices on the same side.

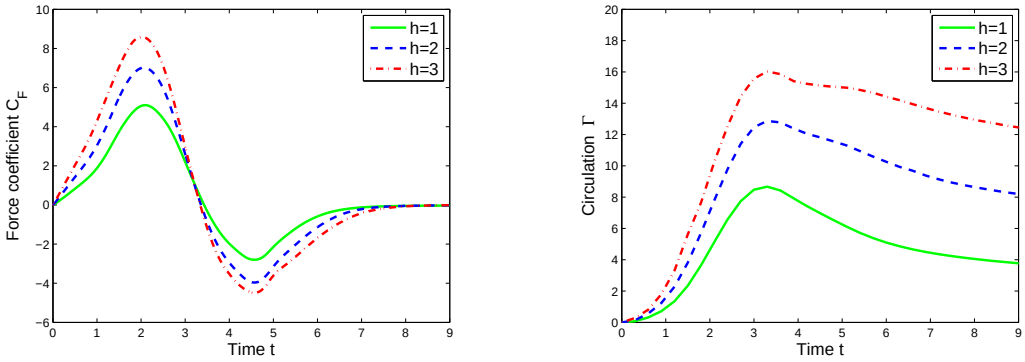

(a) (b)

Figure A.4: Time history of (a) force coefficients and (b) circulations for three plate models in the sinusoidal velocity program.

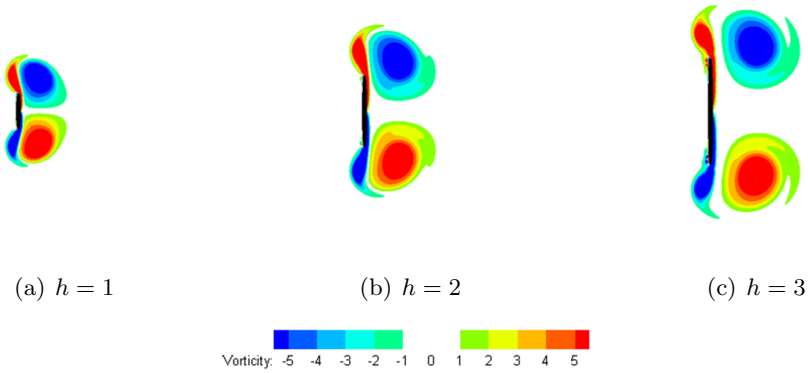

(a) $h = 1$ (b) $h = 2$ (c) $h = 3$

Figure A.5: Vorticity distribution for the sinusoidal velocity program at $t = 4.8$.

Appendix B

Validation of approximated vortex moment theory for force calculation

In order to check how well Eq. 2.6 approximates Eq. 2.4, the force coefficient C_F obtained from Eq. 2.6 was compared to C_F obtained from Eq. 2.4 for the two-dimensional model in Appendix A (the constant velocity program case) and the three-dimensional model in Ch. 2. The angle of attack is 90° in both cases.

B.1 Two-dimensional translating plates

In two-dimensional flow, the numeric in the right-hand side of Eq. 2.4 should be 1 instead of 2, and S_x of Eq. 2.6 is the distance between the centers of counter-rotating vortices. The y-coordinate of the vortex center was defined as $\int |\boldsymbol{\omega} \cdot \boldsymbol{n}| y \mathrm{d}A/\Gamma$ for both vortices in $y > 0$ region and $y < 0$ region. For the thin plate model with a 90° angle of attack, the second term in Eq. 2.4 is negligible during acceleration. The peak of the second term is much smaller than that of the first term in Eq. 2.4.

The distance between the vortex centers is plotted in figure B.1. When the plate starts to translate, most vorticities are on the surface of the plate. Thus, the distance between the vortex centers is smaller than the height of the plate; in the definition of circulation and vortex center, we considered the whole area of either $y > 0$ or $y < 0$, not the separated vortex only. While the vortex sheet is rolled up behind the plate, the distance between the vortex centers becomes close to the height of the plate. As the plate translates further and the vortex becomes larger, the distance increases slightly (see the $h = 1$ case).

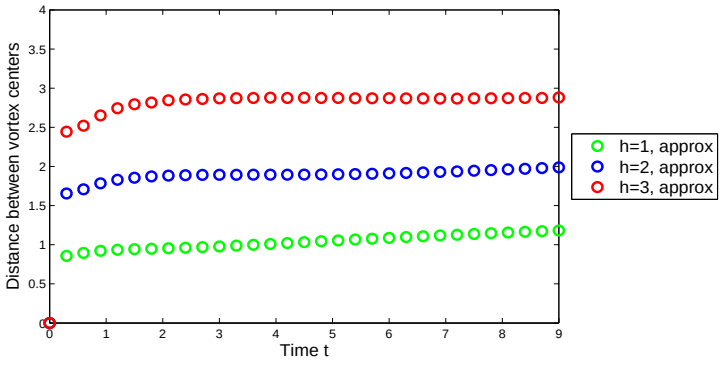

Figure B.1: Distance between vortex centers.

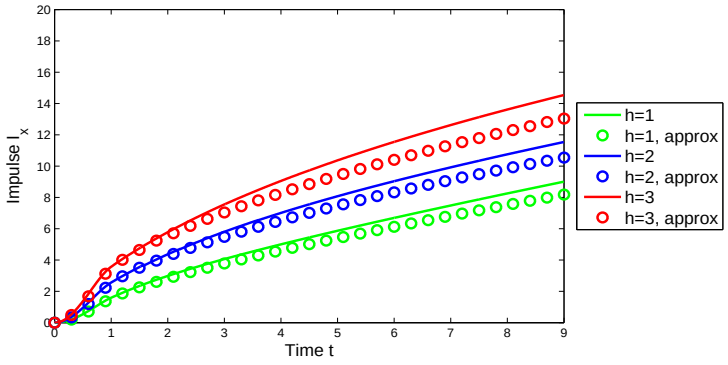

(a)

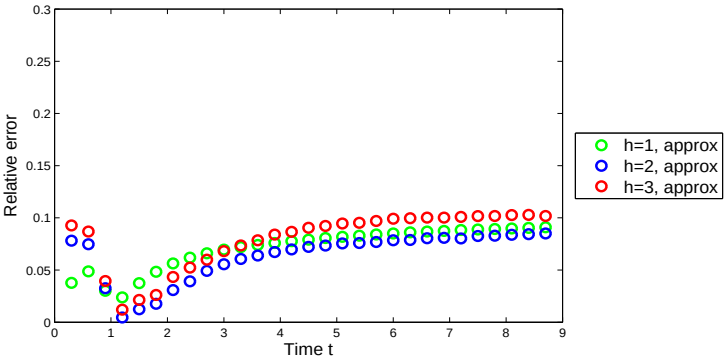

(b)

Figure B.2: (a) Comparison of impulses calculated from the exact equation, Eq. 2.4 (line), and the approximated equation, Eq. 2.6 (circle). (b) Magnitude of the relative error.

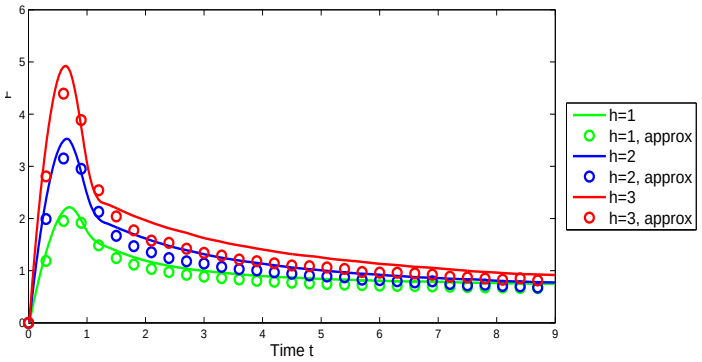

(a)

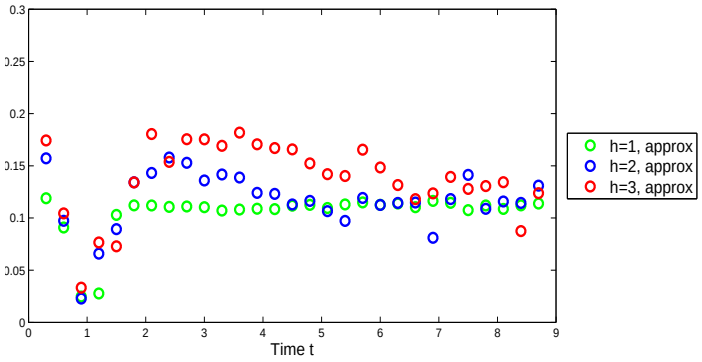

(b)

Figure B.3: (a) Comparison of forces calculated from the exact equation, Eq. 2.4 (line), and the approximated equation, Eq. 2.6 (circle). (b) Magnitude of the relative error.

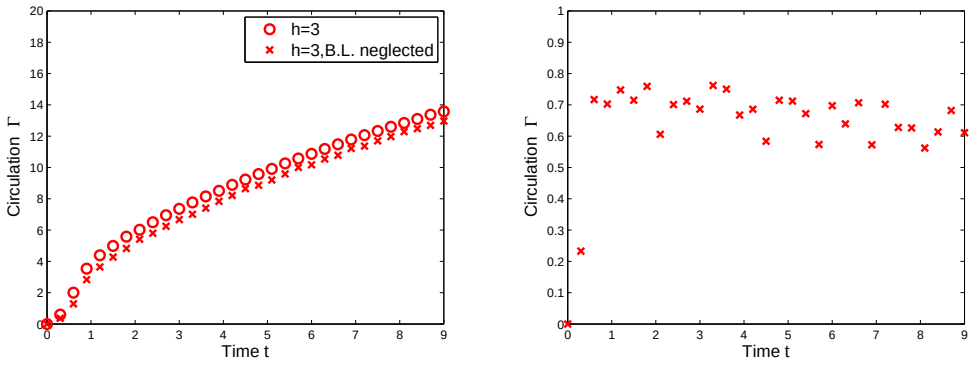

(a) (b)

Figure B.4: (a) Comparison of circulations with and without considering vorticity in the boundary layer for the $h = 3$ case. (b) Circulation of the boundary layer for the $h = 3$ case.

Figure B.2 shows the impulse calculated from the approximated equation, Eq. 2.6 ($\int_0^t C_F(\tau)\mathrm{d}\tau \approx \Gamma S_x/\frac{1}{2}\rho U^2 h$). The magnitude of the maximum relative error is below 0.11. Figure B.3 compares the force coefficient C_F from Eq. 2.6 and the exact force coefficient. The approximated force coefficient was obtained by calculating the slope of the impulse in figure B.2 with central difference scheme. If we used more data points with shorter time step, we could obtained the better approximated force, especially in the initial peak. The magnitude of the maximum relative error is below 0.2.

Next, we check the effect of vorticity in the boundary layer on the circulation and the impulse for the $h = 3$ plate and constant velocity program case (Re = 300). The circulations with and without the vorticity in the boundary layer (the vorticity in front of the plate) were compared in figure B.4. The difference between two circulations, which also means the total vorticity in the boundary layer, is below 0.8. After the initial acceleration phase, the circulation in the boundary layer does not increase, and its contribution to the circulation of either upper or lower-half plane is negligible.

The approximated impulse ($= \Gamma S_x/\frac{1}{2}\rho U^2 h$) was also calculated without considering the vorticity in the boundary layer, and compared to the impulse from the exact equation (Eq. 2.6) (figure B.5(a)). During the initial phase ($t < 1$), there is a large error since a large portion of the circulation is from the boundary layer and it was neglected in the impulse calculation. The force, which was calculated from the slope of the impulse with central difference scheme, was plotted in figure B.5(b). Even if the boundary layer was not

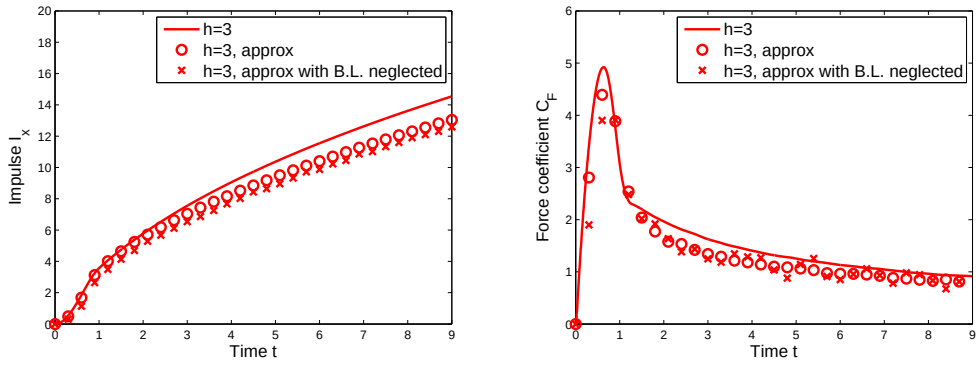

(a) (b)

Figure B.5: Comparison of (a) impulses and (b) forces calculated from the exact equation, Eq. 2.4 (line), the approximated equation, Eq. 2.6 (circle), and the approximated equation with the boundary layer neglected (cross) for the $h = 3$ case.

considered, the temporal trend of the force (e.g., the peak for $t < 1$) could be captured with this approximation. During the initial force peak, the error is larger than that of the case considering the boundary layer. The smaller time step between data points will improve the accuracy of the approximation.

In our translating plate model, the circulation of the boundary layer in either upper or lower-half plane is much smaller than the circulation behind the plate (after $t > 1$). However, for the rotating plate (e.g., paddling plate), the bound vortex on the plate is the counterpart of the the vortex created near the tip as shown in Ch. 3 and figure 1.2. In this case, the strength of the bound vortex cannot be negligible, and the vorticity of the bound vortex is widely distributed on the plate surface. Therefore, it is expected that the simple approximation of the vortex moment theory (Eq. 2.6) may cause the larger error than that of the translating plate case.

B.2 Three-dimensional translating plates

Experimental results of Ch. 2 were used to validate the approximated vortex moment theory. Since the fluid field measured in Ch. 2 is limited to the flow field near the tip, it is difficult to obtain reliable information about the inner area of the vortex, S_x. Thus, in this chapter, we assume that S_x is the frontal area of the plate projected on the yz-plane; S_x is constant. This assumption is reasonable only for the small formation time (e.g., $T < 1$) at

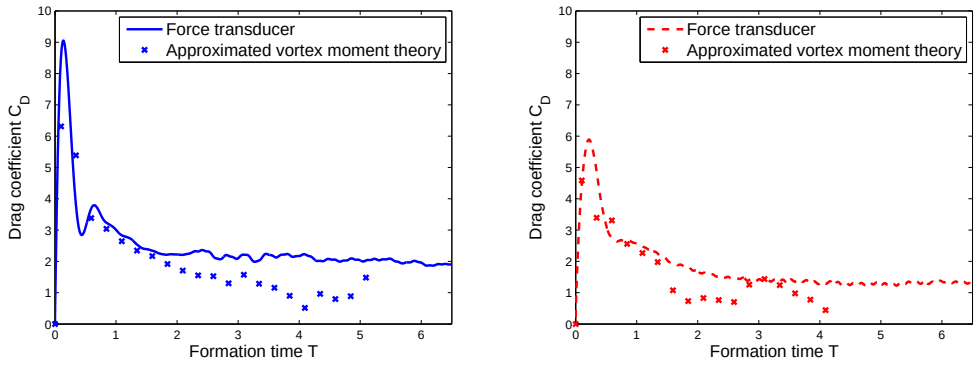

(a) (b)

Figure B.6: Comparison of forces from the approximated vortex moment theory and the force transducer measurement. (a) is from the flat-rigid plate, and (b) is from the curved-rigid plate.

which the vortex sheet is rolled up around the edge of the plate for the rigid plates.

$$D(t) \approx \rho \dot{\Gamma} S_x. \tag{B.1}$$

For the flat-rigid and curved-rigid plates, circulation growth rate $\dot{\Gamma}$ was calculated from the Γ_y curve of $d = 0.62$ in figure 2.15. Γ_y at $d = 0.62$ is not affected by the dynamical change of vortex structure near the tip as much as Γ_y of the other sections ($d = 0.26 \sim 0.56$). Thus, it is regarded as the circulation of the vortex structure S_x in this study. The slope of the circulation was obtained by central difference scheme.

Figure B.6 compares the force coefficients calculated from Eq. B.1 and measured from the force transducer. For $T < 1.5$, the force coefficient trend of the approximated theory follows the trend of the force transducer; after initial peak, the force decreases rapidly. However, for $T > 1.5$, the approximated theory shows the lower force coefficient. For the large T, the vortex deforms and loses its initial shape as demonstrated in figures 2.5 and 2.9. Therefore, $\dot{S}_x$ should not be neglected for the large T. The neglect of $\dot{S}_x$ may be the main reason for the large deficit between two force coefficients. In addition, the circulation curve should be fitted smoothly in order to remove the negative effect of some fluctuation on the force calculation.

Appendix C

Unsteady lift force in butterfly take-off

Many researchers have tried to use the blade element theory with quasi-steady flow assumption in order to calculate the lift force acting on the hovering insect. However, the analysis based on quasi-steady flow assumption has failed to explain the lift force generated by hovering insects (Ellington, 1984a). This approach uses the sectional quasi-steady lift coefficient for the section of the wing. Then, the quasi-steady lift force is obtained by integrating the sectional quasi-steady lift along the wing span. The calculated lift force was found to be smaller than the weight of the hovering insect. In order to solve this paradox, researchers suggested the unsteady lift enhancement mechanisms such as delayed stall of the leading-edge vortex, wake capture, and rotational circulation during stroke reversals (Ellington *et al.*, 1996; Dickinson *et al.*, 1999).

Here, we deal with a similar problem. Can a butterfly take off by the aerodynamic force acting on its wings? For simplicity, we assume that the stroke plane is vertical and the angle of attack is 90° during the power stroke for take-off. Therefore, the vertical component of the drag force acting on the wing will be responsible for lifting the body (figure C.1). We use the kinematic and geometric data of Sunada *et al.* (1993) for a butterfly, *Pieris melete*, with some additional simplifications. From figure 4 of Sunada *et al.* (1993), the kinematics of the wing was approximated. The Reynolds number based on the mean wing tip velocity during the power stroke and the span of one wing is about 4300. The stroke angle ϕ is 150°. The time for the power stroke (T_{p}) is approximately 40% of one beating cycle ($T_{\mathrm{p+r}}$, power and recovery strokes). The wing accelerates its rotation linearly for $0.1T_{\mathrm{p}}$, and decelerates

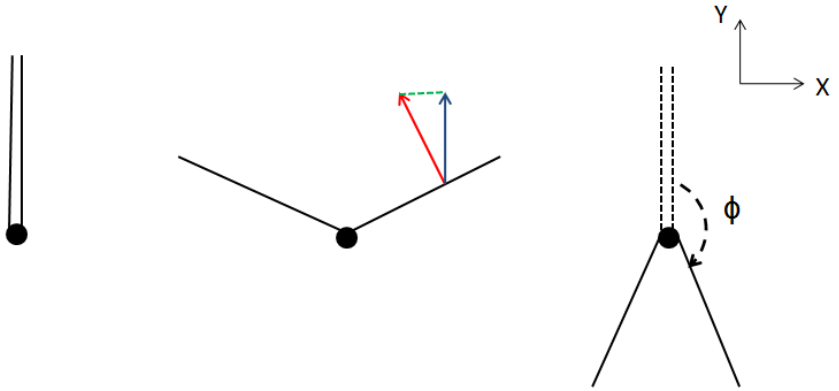

Figure C.1: Wing positions of the butterfly during the power stroke for take-off. The black lines are wings, the red arrows are the drag force acting on the wing, and the blue arrows are the vertical component of the drag force. The stroke angle ϕ is the angle between the first and last positions of the wing during the power stroke.

linearly afterwards. The angular velocity of the wing $\Omega(t)$ is given as,

$$\begin{aligned} \Omega(t) &= \frac{\phi}{2T_{\rm p}}\frac{t}{T_{\rm p}} \qquad (0 \le t \le 0.1T_{\rm p}) \\ &= \frac{\phi}{2T_{\rm p}}(1 - \frac{(t-0.1T_{\rm p})}{0.9T_{\rm p}}) \quad (0.1T_{\rm p} \le t \le T_{\rm p}). \end{aligned} \tag{C.1}$$

The minimum mean force coefficient of the power stroke $\overline{C_{y_{\rm req}}}$ for a wing in one side, which is required for take-off, can be calculated from the following equation.

$$2\overline{F}T_{\rm p} = 2\frac{1}{2}\overline{C_{y_{\rm req}}}\rho\overline{\Omega}^2 M_y T_{\rm p} = WT_{\rm p+r}, \tag{C.2}$$

where $\overline{F}$ is the mean lift force generated during the power stroke for one wing, W is the weight of the butterfly, $\overline{\Omega}$ is the mean angular velocity, M_y is the second moment of area of one wing around the flapping axis, and $T_{\rm p} = 0.4T_{\rm p+r}$. From the kinematic and geometric information in Sunada *et al.* (1993), $\overline{C_{y_{\rm req}}}$ was 2.5. In fact, the time-averaged lift force is not sufficient to track the upward or downward motion of the body, and the instantaneous force should be used to find the dynamics of the body (Dabiri, 2005). Nevertheless, we neglect the dependence of the body motion on the instantaneous force, and simply consider the relation between the weight and the *mean* force acting on the body in order to find the

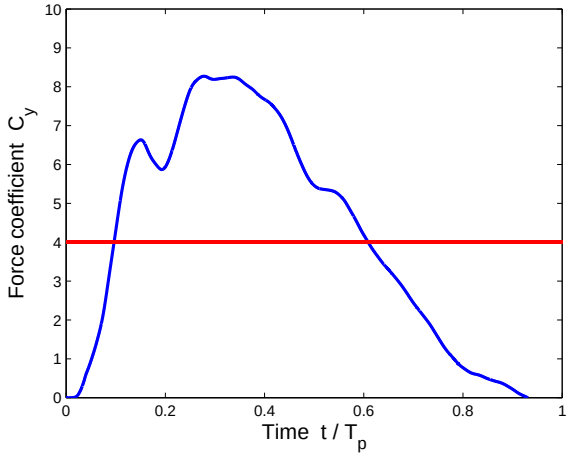

Figure C.2: Force coefficient C_y of one wing during the power stroke, which was measured from the mechanical model. The red line is the mean force coefficient.

minimum force coefficient for take-off. We also neglect the drag acting on the body and the role of legs in producing the lift force for take-off.

In Ch. 4, we measured the non-dimensional total impulse for clapping motion of the model quite similar to the take-off motion of the butterfly wings. The definition of the aspect ratio used in Sunada *et al.* (1993) is different from that of Ch. 4; while the total span of two wings is considered in Sunada *et al.* (1993), the span of one wing is considered in Ch. 4 for the definition of the aspect ratio. With the plate model used in Ch. 4 (rectangular plates of AR = 1) and the kinematic conditions in Eq. C.1, we measured the force coefficient C_y (figure C.2). For the scaled kinematic conditions, the time for the power stroke was 2 sec. The Reynolds number based on the mean tip velocity and the span of one wing was 8400. The mean force coefficient $\overline{C_y}$ in figure C.2 is about 4.0. The mean force coefficient in the y-direction ($\overline{C_y} \approx 4.0$) is larger than the minimum mean force coefficient ($\overline{C_{y_{\mathrm{req}}}} \approx 2.5$) required for take-off, which means that the butterfly can accelerate upward. It also indicates that the butterfly can take off without using the force generated by leg extension.

For the plate that starts to translate with a 90° angle of attack with a constant velocity, the force acting on the plate during the short displacement (i.e., when the displacement of the plate is comparable to the length scale of the plate) is generally larger than the quasi-steady force (see Ch. 2, Appendix A, Dickinson & Götz (1993), and Ringuette *et al.* (2007)). In Sunada *et al.* (1993), the stroke angle of the wing is 150°. The ratio of the wing

tip displacement to the mean chord length is roughly 3.4. This length ratio indicates that the effect of unsteady force is important during the power stroke of the butterfly in take-off.

Bibliography

Alexander, R. M. 2003 *Principles of Animal Locomotion*. Princeton: Princeton University Press.

Algeldinger, T. L. & Fish, F. E. 1995 Hydroplaning by ducklings - overcoming limitations to swimming at the water-surface. *J. Exp. Biol.* **198**, 1567–1574.

Aono, H., Liang, F. & Liu, H. 2008 Near- and far-field aerodynamics in insect hovering flight: an integrated computational study. *J. Exp. Biol.* **211**, 239–257.

Babinsky, H. & Jones, A. R. 2009 Unsteady lift generation on sliding and rotating flat plate wings. In *39th AIAA Fluid Dynamics Conference*. San Antonio, Texas.

Batchelor, G. K. 1967 *An introduction to fluid dynamics*. Cambridge: Cambridge University Press.

Birch, J. M. & Dickinson, M. H. 2001 Spanwise flow and the attachment of the leading-edge vortex on insect wings. *Nature* **412**, 729–733.

Birch, J. M., Dickson, W. B. & Dickinson, M. H. 2004 Force production and flow structure of the leading edge vortex on flapping wings at high and low Reynolds numbers. *J. Exp. Biol.* **207**, 1063–1072.

Blake, R. W. 1979 The mechanics of labriform locomotion. 1. Labriform locomotion in the angelfish (*Pterophyllum Eimekei*) - analysis of the power stroke. *J. Exp. Biol.* **82**, 255–271.

Blake, R. W. 1980 The mechanics of labriform locomotion. 2. An analysis of the recovery stroke and the overall fin-beat cycle propulsive efficiency in the angelfish. *J. Exp. Biol.* **85**, 337–342.

Brodsky, A. K. 1991 Vortex formation in the tethered flight of the peacock butterfly *Inachis Io* L. (Lepidoptera, Nymphalidae) and some aspects of insect flight evolution. *J. Exp. Biol.* **161**, 77–95.

Buchholz, J. H. J. & Smits, A. J. 2006 On the evolution of the wake structure produced by a low-aspect-ratio pitching panel. *J. Fluid Mech.* **546**, 433–443.

Combes, S. A. & Daniel, T. L. 2003*a* Flexural stiffness in insect wings i. Scaling and the influence of wing venation. *J. Exp. Biol.* **206**, 2979–2987.

Combes, S. A. & Daniel, T. L. 2003*b* Flexural stiffness in insect wings ii. Spatial distribution and dynamic wing bending. *J. Exp. Biol.* **206**, 2989–2997.

Combes, S. A. & Daniel, T. L. 2003*c* Into thin air: contributions of aerodynamic and inertial-elastic forces to wing bending in the hawkmoth *Manduca sexta*. *J. Exp. Biol.* **206**, 2999–3006.

Cooter, R. J. & Baker, P. S. 1977 Weis-Fogh clap and fling mechanism in *Locusta*. *Nature* **269**, 53–54.

Crow, S. C. 1970 Stability theory for a pair of trailing vortices. *AIAA J.* **8**, 2172–2179.

Dabiri, J. O. 2005 On the estimation of swimming and flying forces from wake measurements. *J. Exp. Biol.* **208**, 3519–3532.

Dabiri, J. O. 2009 Optimal vortex formation as a unifying principle in biological propulsion. *Annu. Rev. Fluid Mech.* **41**, 17–33.

Dabiri, J. O. & Gharib, M. 2005a Starting flow through nozzles with temporally variable exit diameter. *J. Fluid Mech.* **538**, 111–136.

Dabiri, J. O. & Gharib, M. 2005b The role of optimal vortex formation in biological fluid transport. *Proc. R. Soc. London, Ser. B* **272**, 1557–1560.

Dickinson, M. H. & Götz, K. G. 1993 Unsteady aerodynamic performance of model wings at low Reynolds numbers. *J. Exp. Biol.* **174**, 45–64.

Dickinson, M. H., Lehmann, F. O. & Sane, S. P. 1999 Wing rotation and the aerodynamic basis of insect flight. *Science* **284**, 1954–1960.

Drucker, E. G. & Lauder, G. V. 1999 Locomotor forces on a swimming fish: Three-dimensional vortex wake dynamics quantified using digital particle image velocimetry. *J. Exp. Biol.* **202**, 2393–2412.

Eldredge, J. D. 2007 Numerical simulation of the fluid dynamics of 2D rigid body motion with the vortex particle method. *J. Comput. Phys.* **221**, 626–648.

Eldredge, J. D. 2008 Dynamically coupled fluid-body interactions in vorticity-based numerical simulations. *J. Comput. Phys.* **227**, 9170–9194.

von Ellenrieder, K. D., Parker, K. & Soria, J. 2003 Flow structures behind a heaving and pitching finite-span wing. *J. Fluid Mech.* **490**, 129–138.

Ellington, C. P. 1984a The aerodynamics of hovering insect flight .1. The quasi-steady analysis. *Philos. Trans. R. Soc. London, Ser. B* **305**, 1–15.

Ellington, C. P. 1984b The aerodynamics of hovering insect figh. 3. Kinematics. *Philos. Trans. R. Soc. London, Ser. B* **305**, 41–78.

Ellington, C. P. 1984c The aerodynamics of hovering insect flight. 4. Aerodynamic mechanisms. *Philos. Trans. R. Soc. London, Ser. B* **305**, 79–113.

Ellington, C. P., Van den Berg, C., Willmott, A. P. & Thomas, A. L. R. 1996 Leading-edge vortices in insect flight. *Nature* **384**, 626–630.

Epps, B. P. & Techet, A. 2007 Impulse generated during unsteady maneuvering of swimming fish. *Exps. Fluids* **43**, 691–700.

Fish, F. E. 1984 Mechanics, power output and efficiency of the swimming muskrat (*Ondatra Zibethicus*). *J. Exp. Biol.* **110**, 183–201.

Fohl, T. & Turner, J. S. 1975 Colliding vortex rings. *Phys. Fluids* **18**, 433–436.

Gal, J. M. & Blake, R. W. 1988 Biomechanics of frog swimming. 2. Mechanics of the limb-beat cycle in *Hymenochirus Boettgeri*. *J. Expl Biol.* **138**, 413–429.

Gharib, M., Rambod, E. & Shariff, K. 1998 A universal time scale for vortex ring formation. *J. Fluid Mech.* **360**, 121–140.

Graff, E. C. 2007 On the development of defocusing digital particle image velocimetry with full characterization. Ph.d. thesis, California Institute of Technology.

Graff, E. C. & Gharib, M. 2008 Performance prediction of point-based three-dimensional volumetric measurement systems. *Meas. Sci. Technol.* **19**, 075403.

Grothe, R. L. & Dabiri, D. 2008 An improved three-dimensional characterization of defocusing digital particle image velocimetry (DDPIV) based on a new imaging volume definition. *Meas. Sci. Technol.* **19**, 065402.

Haller, G. 2005 An objective definition of a vortex. *J. Fluid Mech.* **525**, 1–26.

Jeong, J. & Hussain, F. 1995 On the identification of a vortex. *J. Fluid Mech.* **285**, 69–94.

Johansson, L. C. & Lauder, G. V. 2004 Hydrodynamics of surface swimming in leopard frogs (*Rana Pipiens). J. Expl Biol.* **207**, 3945–3958.

Kajitani, L. & Dabiri, D. 2005 A full three-dimensional characterization of defocusing digital particle image velocimetry. *Meas. Sci. Technol.* **16**, 790–804.

Kida, S. & Takaoka, M. 1987 Bridging in vortex reconnection. *Phys. Fluids* **30**, 2911–2914.

Kida, S. & Takaoka, M. 1994 Vortex reconnection. *Annu. Rev. Fluid Mech.* **26**, 169–189.

Kida, S., Takaoka, M. & Hussain, F. 1991 Collision of two vortex rings. *J. Fluid Mech.* **230**, 583–646.

Koumoutsakos, P. & Shiels, D. 1996 Simulations of the viscous flow normal to an impulsively started and uniformly accelerated flat plate. *J. Fluid Mech.* **328**, 177–227.

Krueger, P. S. & Gharib, M. 2003 The significance of vortex ring formation to the impulse and thrust of a starting jet. *Phys. Fluids* **15**, 1271–1281.

Lai, W., Pan, G., Menon, R., Troolin, D., Graff, E. C., Gharib, M. & Pereira, F. 2008 Volumetric three-component velocimetry: a new tool for 3D flow measurement. In *14th Int. Symp. on Applications of Laser Techniques to Fluid Mechanics*. Lisbon, Portugal.

Lentink, D. 2008 Exploring the biofluiddynamics of swimming and flight. Ph.d. thesis, Wageningen University.

Leonard, A. & Roshko, A. 2001 Aspects of flow-induced vibration. *J. Fluids Struct.* **15**, 415–425.

Lugt, H. J. 1996 *Introduction to Vortex Theory*. Potomac: Vortex Flow Press.

Maxworthy, T. 1979 Experiments on the Weis-Fogh mechanism of lift generation by insects in hovering flight. 1. Dynamics of the fling. *J. Fluid Mech.* **93**, 47–63.

Maxworthy, T. 1981 The fluid dynamics of insect flight. *Annu. Rev. Fluid Mech.* **13**, 329–350.

Melander, M. V. & Hussain, F. 1990 Topological aspects of vortex reconnection. In *Proc. IUTAM Symp.*, pp. 485–499. Cambridge: Cambridge Univ. Press.

Milano, M. & Gharib, M. 2005 Uncovering the physics of flapping flat plates with artificial evolution. *J. Fluid Mech.* **534**, 403–409.

Miller, L. A. & Peskin, C. S. 2005 A computational fluid dynamics of 'clap and fling' in the smallest insects. *J. Exp. Biol.* **208**, 195–212.

Mountcastle, A. M. & Daniel, T. L. 2009 Aerodynamic and functional consequences of wing compliance. *Exps. Fluids* **46**, 873–882.

Oshima, Y. & Asaka, S. 1977 Interaction of two vortex rings along parallel axes in air. *J. Phys. Soc. Jpn.* **42**, 708–713.

Pereira, F. & Gharib, M. 2002 Defocusing digital particle image velocimetry and the three-dimensional characterization of two-phase flows. *Meas. Sci. Technol.* **13**, 683–694.

Pereira, F., Gharib, M., Dabiri, D. & Modarress, D. 2000 Defocusing digital particle image velocimetry: a 3-component 3-dimensional DPIV measurement technique. Application to bubbly flows. *Exps. Fluids* **29**, S78–S84.

Pereira, F., Stuer, H., Graff, E. C. & Gharib, M. 2006 Two-frame 3D particle tracking. *Meas. Sci. Technol.* **17**, 1680–1692.

Poelma, C., Dickson, W. B. & Dickinson, M. H. 2006 Time-resolved reconstruction of the full velocity field around a dynamically-scaled flapping wing. *Exps. Fluids* **41**, 213–225.

Prandtl, L. & Tietjens, O. G. 1934 *Applied Hydro- and Aeromechanics*. New York and London: McGraw-Hill.

Pullin, D. I. 1978 Large-scale structure of unsteady self-similar rolled-up vortex sheets. *J. Fluid Mech.* **88**, 401–430.

Pullin, D. I. & Perry, A. E. 1980 Some flow visualization experiments on the starting vortex. *J. Fluid Mech.* **97**, 239–255.

Pullin, D. I. & Wang, Z. J. 2004 Unsteady forces on an accelerating plate and application to hovering insect flight. *J. Fluid Mech.* **509**, 1–21.

Ringuette, M. J., Milano, M. & Gharib, M. 2007 Role of the tip vortex in the force generation of low-aspect-ratio normal flat plates. *J. Fluid Mech.* **581**, 453–468.

Saffman, P. G. 1995 *Vortex Dynamics*. Cambridge: Cambridge University Press.

Shyy, W. & Liu, H. 2007 Flapping wings and aerodynamic lift: The role of leading-edge vortices. *AIAA J.* **45**, 2817–2819.

Spedding, G. R. & Maxworthy, T. 1986 The generation of circulation and lift in a rigid two-dimensional fling. *J. Fluid Mech.* **165**, 247–272.

Spedding, G. R., Rosen, M. & Hedenstrom, A. 2003 A family of vortex wakes generated by a thrush nightingale in free flight in a wind tunnel over its entire natural range of flight speeds. *J. Exp. Biol.* **206**, 2313–2344.

Srygley, R. B. & Thomas, A. L. R. 2002 Unconventional lift-generating mechanisms in free-flying butterflies. *Nature* **420**, 660–664.

Stamhuis, E. J. & Nauwelaerts, S. 2005 Propulsive force calculations in swimming frogs. ii. Application of a vortex ring model to DPIV data. *J. Exp. Biol.* **208**, 1445–51.

Sunada, S., Kawachi, K., Watanabe, I. & Azuma, A. 1993 Performance of a butterfly in take-off flight. *J. Exp. Biol.* **183**, 249–277.

Taira, K. & Colonius, T. 2009 Three-dimensional flows around low-aspect-ratio flat-plate wings at low Reynolds numbers. *J. Fluid Mech.* **623**, 187–207.

Vogel, S. 2003 *Comparative Biomechanics: Life's Physical World*. Princeton: Princeton University Press.

Walker, J. A. 2004 Dynamics of pectoral fin rowing in a fish with an extreme rowing stroke: the threespine stickleback (*Gasterosteus aculeatus*). *J. Exp. Biol.* **207**, 1925–1939.

Walker, J. A. & Westneat, M. W. 2000 Mechanical performance of aquatic rowing and flying. *Proc. R. Soc. London, Ser. B* **267**, 1875–1881.

Wang, Z. J. 2004 The role of drag in insect hovering. *J. Exp. Biol.* **207**, 4147–4155.

Weis-Fogh, T. 1973 Quick estimates of flight fitness in hovering animals, including novel mechanisms for lift production. *J. Exp. Biol.* **59**, 169–230.

Willert, C. E. & Gharib, M. 1991 Digital particle image velocimetry. *Exp. In Fluids* **10**, 181–193.

Willert, C. E. & Gharib, M. 1992 Three-dimensional particle imaging with a single camera. *Exps. Fluids* **12**, 353–358.

Wu, J. C. 1981 Theory for aerodynamic force and moment in viscous flows. *AIAA Journal* **19**, 432–441.

Wu, J. Z., Ma, H. Y. & Zhou, M. D. 2006 *Vorticity and Vortex Dynamics*. Berlin Heidelberg: Springer.

Young, J., Walker, S. M., Bomphrey, R. J., Taylor, G. K. & Thomas, A. L. R. 2009 Details of insect wing design and deformation enhance aerodynamic function and flight efficiency. *Science* **325**, 1549–1552.